



**HAL**  
open science

# Development of the thin film solid solutions of perovskite based transparent conductors

Oualyd El Khaloufi

► **To cite this version:**

Oualyd El Khaloufi. Development of the thin film solid solutions of perovskite based transparent conductors. Physics [physics]. Normandie Université, 2023. English. NNT : 2023NORMC237 . tel-04362520

**HAL Id: tel-04362520**

**<https://theses.hal.science/tel-04362520>**

Submitted on 22 Dec 2023

**HAL** is a multi-disciplinary open access archive for the deposit and dissemination of scientific research documents, whether they are published or not. The documents may come from teaching and research institutions in France or abroad, or from public or private research centers.

L'archive ouverte pluridisciplinaire **HAL**, est destinée au dépôt et à la diffusion de documents scientifiques de niveau recherche, publiés ou non, émanant des établissements d'enseignement et de recherche français ou étrangers, des laboratoires publics ou privés.



Normandie Université



UNIVERSITÉ  
CAEN  
NORMANDIE

## THÈSE

Pour obtenir le diplôme de doctorat

Spécialité PHYSIQUE

Préparée au sein de l'Université de Caen Normandie

**Development of the thin film solid solutions of perovskite based transparent conductors**

**Présentée et soutenue par  
OUALYD EL KHALOUFI**

**Thèse soutenue le 20/10/2023  
devant le jury composé de**

MME NATHALIE LEMÉE	Professeur des universités, UNIVERSITE AMIENS PICARDIE JULES VERNE	Rapporteur du jury
M. DAVID MUNOZ-ROJAS	Directeur de recherche, Université Grenoble Alpes	Rapporteur du jury
M. ROMAIN BACHELET	Chargé de recherche, INSTITUT DES NANOTECHNOLOGIES DE LYON	Membre du jury
M. SYLVAIN VEDRDAINE	Maître de conférences, Université de Limoges	Membre du jury
M. WILFRID PRELLIER	Directeur de recherche au CNRS, ENSICAEN	Président du jury
MME ULRIKE LÜDERS	Directeur de recherche au CNRS, ENSICAEN	Directeur de thèse

**Thèse dirigée par ULRIKE LÜDERS (Laboratoire de cristallographie et sciences des matériaux (Caen))**





## Acknowledgements

I would like to begin by dedicating this thesis to dearest to my heart, Mom and Dad, whose unwavering love and support have been my strength throughout this journey. To my little sisters, Soukaina, Basma, and Yasmine, your presence in my life has meant the world to me.

I extend my heartfelt gratitude to the esteemed members of the jury who accepted the responsibility of evaluating my work: Romain Bachelet, David Muñoz-Rojas, Nathalie Lemee, and Sylvain Vedraïne. Your expertise and insights has enrich this research.

My sincere thanks go to Wilfrid Prellier, the director of the CRISMAT laboratory, for not only welcoming me into the brilliant team of CRISMAT but also for his unwavering support, both personally and professionally.

I would like to express my deepest appreciation to my dear thesis supervisor, Ulrike Luders. Ulrike... you have been more than just a supervisor; you have been a friend and a mentor. Your infectious positivity, your jokes, your clever and smart approach to science, and your expertise in material science have made these three years of my PhD the highlight of my professional and academic career. You will forever be my inspiration.

A special note of gratitude goes to the one and only Abhishek YADAV, the brother I never had but found later in life. Your friendship, support, and partnership have been invaluable and words can not describe my gratitude for you little brother. You shared every step of this journey with me, day by day, year by year. Without you, I wouldn't be the person I am today. May our friendship and brotherhood last forever. While I wish I could fill an entire page with words of gratitude, I find that expressing the depth of my appreciation a challenge. Being grateful to someone is effortless, but finding the right words to express it can be quite hard. I expect you to understand all this when you will become a doctor. And, as a wise man once said, we didn't choose strength, strength has chosen us.

I would like to offer a special thanks to my little angel, Julie. Whose endless help and support sustained me during challenging times. Loulou, This work is dedicated to you, and I will always be grateful for your unwavering support. Your presence provided me with the strength to persevere through challenging moments, and your patience in bearing with me meant the world to me, VALE VALE.

To Badran, the sweetest Lebanese, I extend my deepest gratitude for your unwavering support. Your place provided the inspiration and motivation I needed to complete this thesis. I will be forever grateful to you, and i could never thank you enough for what you did for me.

A heartfelt thanks to my beloved friends and seniors, Martando, and Aimane. Your invaluable assistance, ideas, and scientific expertise greatly contributed to the success of this thesis. I could never thank you enough...

My heartfelt and enduring thanks go to Cintli and Mike, who though they are far away, remain forever in my mind and in my heart. The boundless love and care you both showered upon me continue to inspire and lift me every day. This work is dedicated to you, dear friends, as a testament to the impact you've had on my life.

A big thanks to Vincent, Damien, and Mathieu for their invaluable help and supervision throughout this journey.

To albarito and mufeed, my beloved friends and office neighbors, thanks for the endless moments of laughter and jokes.

A special thanks to Mudit updhayhaya, for his unique talent of doing nothing. Your ability to contribute absolutely nothing to this journey has been remarkable.

I must also recognize Mouhcine, Arpan, Hasanthi and Badr, without whom, this work would have been finished earlier.

To my beloved colleagues and friends: Krisnendu, Jofrey, Nishu, Abdel, Moussa, Erica, Sara, Luska, and everyone else. The countless coffee breaks, the after-work parties, and the positive work vibes you brought into our shared journey were the sources of motivation and support. Together, we created an environment that made the challenges seem easy and the victories all sweeter. I thank each and every one of you, from the bottom of my heart.



---

# Contents

---

<b>1</b>	<b>General introduction</b>	<b>1</b>
<b>2</b>	<b>State of the art</b>	<b>5</b>
2.1	Transparent conducting oxide . . . . .	6
2.1.1	Band structure differences for correlated metals . . . . .	8
2.2	Perovskite Oxides . . . . .	11
2.3	Epitaxial strain . . . . .	14
2.4	Perovskite Vanadates . . . . .	16
2.4.1	Earlier studies at the CRISMAT . . . . .	26
2.5	Perovskite Chromites . . . . .	29
<b>3</b>	<b>Experimental Methods</b>	<b>37</b>
3.1	Thin film synthesis . . . . .	38
3.1.1	Pulsed Laser Deposition (PLD) . . . . .	40
3.1.2	Growth parameters . . . . .	41
3.1.3	Solid solution compositional calibration . . . . .	43
3.1.4	Surface cleaning of Vanadate films . . . . .	47
3.2	Structural characterization . . . . .	50
3.2.1	X-Ray Diffraction . . . . .	50
3.2.2	X-ray reflectivity . . . . .	53

3.3	Spectroscopic measurements . . . . .	56
3.3.1	X-ray photoelectron spectroscopy (XPS) . . . . .	56
3.3.2	X-ray absorption spectroscopy (XAS) . . . . .	60
3.4	Electrical measurements . . . . .	66
3.4.1	Electrical resistivity . . . . .	67
3.4.2	Hall effect . . . . .	68
3.5	Optical measurements . . . . .	69
3.5.1	Perkin Elmer Spectrophotometer: Measurement of optical transmission and reflection. . . . .	69
<b>4</b>	<b>(La,Sr)VO<sub>3</sub> solid solution thin films</b>	<b>73</b>
4.1	Growth of solid solution thin films . . . . .	74
4.1.1	Growth optimization . . . . .	74
4.1.2	Chemical characterisation . . . . .	79
4.2	(La,Sr)VO <sub>3</sub> as a transparent conducting oxide . . . . .	87
4.2.1	Electrical resistivity . . . . .	87
4.2.2	Hall effect . . . . .	91
4.2.3	Optical measurements . . . . .	92
4.2.4	The effect of La doping on electronic correlations . . . . .	94
4.3	Strain engineering . . . . .	97
4.3.1	Structural and chemical characterization . . . . .	97
4.3.2	Analysis of the functional TCO properties . . . . .	103
4.4	Interaction of the (La,Sr)VO <sub>3</sub> surface with different atmosphere . . . . .	106
<b>5</b>	<b>(La, Sr)CrO<sub>3</sub> solid solution thin films</b>	<b>113</b>
5.1	Growth of the solid solution thin films . . . . .	115
5.1.1	Structural characterizations . . . . .	116
5.1.2	Chemical characterization . . . . .	120
5.2	TCO properties of LSCO solid solution thin films . . . . .	123
5.3	Strain engineering of LSCO . . . . .	128
5.3.1	Structural Analysis . . . . .	128
5.3.2	Electrical properties . . . . .	130

---

5.3.3 Integration with solar cell materials . . . . .	132
<b>6 General conclusion and perspectives</b>	<b>139</b>
<b>List of publications and conferences</b>	<b>145</b>



---

## List of Figures

---

2.1	Conductivity $\sigma$ vs screened plasma frequency $\omega$ of different semiconductor TCOs, metals and correlated metals. Taken from reference [1]	8
2.2	Band structure of (a) ITO and (b) SVO. Taken from reference [2]	9
2.3	The perovskite structure: (a) constituting octahedra in the cubic phase with the orientations using Miller indexes, (b) rotation of octahedra for tolerance factors $t \neq 1$ , (c) orthorhombic distortion of the cubic perovskite structure, (c) cubic perovskite structure. Taken from reference [3]	11
2.4	The lattice constant of different perovskite oxides. Taken from reference [4].	14
2.5	Illustration of the adaptation of the film perovskite unit cell to compressive and tensile strain. Taken from reference [5].	15
2.6	Illustration of the optical conductivity (a) and the band structure (b) of a strongly correlated metal ( $U < t$ ) and a Mott insulator ( $U > t$ ). Adapted from reference [6]	17

2.7	(a) Optical transmittance of SVO films on LSAT, about 50 nm thick, deposited either at $P(\text{Ar}) = 0$ mbar (red) or at $P(\text{Ar}) = 0.1$ mbar (blue) (b) Temperature dependence of the normalized resistivity $\rho(T) / \rho(300 \text{ K})$ for SVO films on LSAT and $\text{NdGaO}_3$ substrates. Taken from reference [7] . . . . .	18
2.8	Variation of the dielectric function of LVO with energy. Illustration of the electronic structure indicating the different excitations related to the optical transitions. Taken from reference [8] . . . . .	21
2.9	(a) Phase diagram of $\text{LaVO}_x$ under different deposition conditions, (b) Annular dark-field electron microscopy (ADF) showing the presence of 3D $\text{LaVO}_4$ islands in the $\text{LaVO}_3$ film. Taken from reference [9] . . . . .	22
2.10	(a) Absorption coefficient values of vanadium-rich LVO (green symbols), lanthanum-rich LVO (pink symbols), and stoichiometric LVO (blue symbols), (b) The optical conductivity of bulk LVO compared to LVO deposited by HMBE and LVO deposited by PVD. Taken from reference [10] . . . . .	22
2.11	Temperature dependent resistivity for a single crystal of the solid solution $\text{La}_{1-x}\text{Sr}_x\text{VO}_3$ . Taken from reference [11] . . . . .	23
2.12	(a) Temperature-dependent sheet resistance of the LSVO thin films. (b) Resistivity versus $T^2$ using the Fermi liquid model in the metallic region for the LSVO thin films. Figures taken from reference [12] . . . . .	24
2.13	(a) Transmission spectrum of the LSVO thin films with varying thickness on LSAT substrates. (b) Photographs of 12, 24, and 48 nm LSVO thin films on LSAT substrates. (c) The plot of $(\alpha h\nu)^2$ versus $h\nu$ for the 48 nm LSVO thin film. Figures taken from reference [12]. . . . .	25
2.14	Reciprocal Space Maps of the (103) XRD reflection of a SVO film deposited on STO (a), LAO (b) and LSAT (c). The $Q_x$ alignment of the substrate peak and the film peak indicate the coherently strained growth of the film on the substrate. Figures taken from references [13] and [14]. . . . .	26

2.15	(a) Low magnification cross-sectional bright field TEM image of as grown SVO thin film on STO substrate, (b) High resolution TEM image of the sample and insets show fast Fourier Transform (FFT) patterns of SVO grown on the STO substrate, (c) High resolution STEM-HAADF micrograph showing perfect alignment of [001] SVO film on [001] STO. The dotted line indicates the interface position, (d) is a low magnification STEM-HAADF image showing the similar Z contrast between SVO and STO and (e-h) STEM-EDX mappings of the elements O, Sr, Ti and V respectively. . . . .	27
2.16	Typical RBS spectrum of a thin SVO film on STO (001). . . . .	28
2.17	Electrical and optical properties of LSCO: (a) Temperature dependence of the conductivity, (b) Optical transmission and photographs of the LSCO films deposited on STO(001), (c) RT conductivity and hole concentration versus $x$ . Taken from reference [15]. . . . .	30
2.18	Band structure of (a) metallic and (b) polaronic $\text{La}_{0.75}\text{Sr}_{0.25}\text{CrO}_3$ . Blue states are occupied at $T = 0$ K. Taken from reference [16] . . . .	31
2.19	Temperature-dependent properties. (a) Seebeck coefficient (S), (b) electrical conductivity and (c) thermoelectric power factor ( $\text{PF} = S^2$ ) for each film as a function of the temperature in the range of 300-400 K. Taken from reference [17] . . . . .	33
2.20	In-plane electronic and thermoelectric transport characterizations. (a) Temperature dependence of the resistivity ( $\rho_{xx}$ ) in the 100-400 K range. (b) Corresponding temperature dependence of the conductivity. (c) Activation energies ( $E_a$ ) for small polaron hopping extracted from (b), plotted as a function of in-plane strain. (d) Room temperature Seebeck coefficient (S) and fraction of hopping sites occupied with holes (hSPH) estimated from S and small polaron hopping model, plotted as a function of in-plane strain. Taken from reference [17] . . . . .	34

2.21	Resistivity for the $\text{La}_{1-x}\text{Sr}_x\text{CrO}_3$ film series (open squares) along with fits for $x = 0.12, 0.25,$ and $0.50$ (solid curves). Taken from reference [18] . . . . .	35
3.1	Image of the plume generated by the impact of the laser on the target (left side) and schematics of Pulsed Laser Deposition (right side). . .	41
3.2	XRR of $\text{LaVO}_3$ on STO (a) and $\text{SrVO}_3$ on STO (b) single film samples with different numbers of laser pulses, (c) XRR simulation of one of the $\text{LaVO}_3$ samples with Genx. . . . .	44
3.3	The correlation between the thickness of the samples and the laser pulses for (a) SVO and (b) LVO. The red lines are linear fits of the data. . . . .	45
3.4	(a) XRR measurements of the different calibration superlattices for $\text{SrCrO}_3/\text{LaCrO}_3$ , (b) Graphical solution of the three superlattice equations. . . . .	47
3.5	O 1s and V 2p3 (a), and Sr 3d (b) XPS spectra recorded before (dark green) and after liquid water cleaning procedure of 1 min (red). (c) XRR spectra before and after the water cleaning. Figures taken from reference [19] . . . . .	48
3.6	Schematic representation of the X-ray measurement principle, with the incident beam on the left side with an incident angle $\theta$ . The crystalline lattice is characterized by the interplane distance $d$ . [20] .	51
3.7	Schematic representation of the X-ray measurement configurations. [21]	52
3.8	Thickness determination methodology (a) Typical XRR profile (b) $\sin^2\theta$ as a function of $n^2$ (considering $n = 1,2,3,4$ and $5$ ) and the linear fits. In the shown example, $n = 2$ is chosen as the correct linear dependence. . . . .	54
3.9	Schematic representation of the photoabsorption process of X-rays. [22]	57
3.10	Charge compensation using flood gun during the XPS measurement. [23]	58
3.11	La 4d core level XPS spectra of the solid solution thin films (a) with flood gun, (b) without flood gun. . . . .	59

3.12 O 1s - V 2p3 core level XPS spectra of the solid solution thin films (a) with flood gun, (b) without flood gun. . . . .	60
3.13 Sr 3d core level XPS spectra of the solid solution thin films (a) with flood gun, (b) without flood gun. . . . .	60
3.14 X-ray absorption spectrum with the NEXAFS and EXAFS regions. . . . .	62
3.15 L2 and L3 absorption edges of the different oxidation states of vana- dium (a) adapted from [24] (b) adapted from [25], and (c) adapted from [9]. . . . .	64
3.16 Comparison between the three adapted references (a) V <sup>3+</sup> , (b) V <sup>4+</sup> , and (c) V <sup>5+</sup> . . . . .	65
3.17 (a) Schematic representation of the PPMS, (b) details of the sample puck . . . . .	66
3.18 Hall measurement in Van Der Pauw configuration. [26] . . . . .	68
3.19 Schematic representation of Perkin Elmer 1050 UV-vis-NIR . . . . .	70
3.20 Schematic representation of Perkin Elmer 1050 UV-vis-NIR . . . . .	71
4.1 $\theta - 2\theta$ scan of the (002) reflection of the STO and the SrVO <sub>3</sub> (a) and LaVO <sub>3</sub> (b) thin films at various deposition temperatures . . . . .	74
4.2 $\theta - 2\theta$ scan of the (002) reflection of the STO and the LSVO solid solution set for a deposition temperature of (a) 500 °C and (b) 700 °C. 75	75
4.3 Evolution of the out-of-plane lattice parameter $c$ with lanthanum con- tent $x$ for the two deposition temperatures. The horizontal lines in- dicate the lattice parameters of SrVO <sub>3</sub> , LaVO <sub>3</sub> and SrTiO <sub>3</sub> bulk value. 77	77
4.4 (a) Evolution of the resistivity of the conductive LSVO samples with the temperature (b) Hall effect at 10K of the composition $x = 0.66$ . . . . .	78
4.5 (a) Reciprocal Space Map of the (103) reflection of the STO substrate and the LSVO film with a La content of 83 % . . . . .	78
4.6 (a) XPS survey spectra of LSVO solid solution thin films for specific La <sub><math>x</math></sub> Sr <sub>1-<math>x</math></sub> VO <sub>3</sub> compositions ( $x = 0$ bottom panel, 0.33 middle panel, and 0.5 top panel) (b) Experimental composition extracted from the average of XPS and EDS vs nominal composition. . . . .	80

4.7	La 4d core level XPS spectra (a) of the solid solution films and (b) the integrated area of the core levels. . . . .	81
4.8	Core level XPS spectra of the $x = 0.5$ solid solution thin film before and after a surface water treatment. . . . .	81
4.9	Experimental La/Sr ratio determined from XPS measurements before (orange squares) and after (green circles) the water treatment of the LSVO solid solution samples. The nominal La/Sr ratio is indicated by open triangles. . . . .	82
4.10	XPS Sr 3d core level spectra (black circles) with fit: Sr lattice contribution (orange line), Sr surface contribution (green line) and the full simulation (blue line). . . . .	83
4.11	XPS V 2p3 core level spectra (black circles) with fit: $V^{3+}$ contribution (green line), $V^{4+}$ contribution (yellow line), $V^{5+}$ contribution (green line), and the full simulation (blue line). . . . .	84
4.12	Relative contribution of the different V oxidation states to the XPS V 2p3 core level as a function of the La content . . . . .	85
4.13	XAS spectra of the V L2,3 edge for a SVO single film (a), $x = 0.16$ (b), 0.33 (c), 0.5 (d) and 0.66 (e), and a LVO single film (f). Data is shown in black, the contributions of the $V^{3+}$ , $V^{4+}$ and $V^{5+}$ as green, orange and yellow line, respectively. The full simulation is shown as a blue dashed line. In the bottom of the panels, the quantification of the relative contribution of the three V oxidation states is displayed in shades of blue. . . . .	86
4.14	Relative contents of $V^{3+}$ , $V^{4+}$ and $V^{5+}$ oxidation state vs the La content. . . . .	87
4.15	(a) Resistivity as a function of temperature of the LSVO solid solution thin films, and (b) evolution of resistivity with lanthanum content. . . . .	88
4.16	(a) The fit parameters $\alpha$ (left axis) and $A$ (right axis), and (b) the residual resistivity $\rho_0$ as a function of the La content. . . . .	89
4.17	(a) Hall resistance as function of magnetic field of the LSVO solid solution films (b) Charge density $n$ at 10K and 300K vs $x$ (c) Carrier mobility at 10K and 300K vs $x$ . . . . .	91

4.18 (a) Optical reflectivity of $\text{La}_x\text{Sr}_{1-x}\text{VO}_3$ solid solution thin films, (b) the screened plasma frequency $\omega_p^*$ versus La content. . . . .	93
4.19 Evolution of the effective mass (left axis) of the charge carriers in $(\text{La,Sr})\text{VO}_3$ as a function of the La content in the thin films (red symbols) and in bulk (black symbols, data taken from [27], [28] and [29]). The solid line represents the tetragonal distortion $c/a$ (right axis) of the solid solution thin films. . . . .	95
4.20 (a) $\theta-2\theta$ scan of the (002) reflection of the LSAT and the $\text{La}_x\text{Sr}_{1-x}\text{VO}_3$ solid solution thin films, (b) Out-of-plane lattice parameter evolution with the La content. . . . .	98
4.21 Experimental composition extracted from XPS before and after water treatment versus the nominal composition for LSVO solid solution films grown on LSAT (001). . . . .	99
4.22 XPS Sr 3d core level spectra (black circles) of LSVO solid solution films grown on LSAT (001) with fit: Sr lattice contribution (orange line), Sr surface contribution (green line) and the full simulation (blue line). . . . .	100
4.23 Relative contribution of the XPS Sr 3d lattice signal as a function of the La content. . . . .	100
4.24 XPS V 2p3 core level spectra (black circles) with fit: $\text{V}^{3+}$ contribution (green line), $\text{V}^{4+}$ contribution (yellow line), $\text{V}^{5+}$ contribution (green line), and the full simulation (blue line). . . . .	101
4.25 Relative contribution of the different V oxidation states to the XPS V 2p3 core level as a function of the La content of LSVO/LSAT. . . . .	102
4.26 Resistivity as a function of temperature of the LSVO solid solution thin films on LSAT. . . . .	103
4.27 (a) The fit parameters $\alpha$ (right axis) and $A$ (left axis), and (b) the residual resistivity $\rho_0$ as a function of the La content. . . . .	104
4.28 Optical transparency of the solid solution thin films as a function of wavelength. . . . .	104

4.29	XAS vanadium L2 and L3 edges spectra with helium induced reduction for (a) 0.16 (b) 0.33 (c) 0.5 (d) 0.66. . . . .	106
4.30	XAS vanadium L2 and L3 edges spectra under different atmospheres (oxygen green lines, He violet lines and H <sub>2</sub> O vapor blue line) for (a) 0.16 (b) 0.33 (c) 0.5 (d) 0.66. . . . .	107
4.31	vanadium L2 and L3 edges spectra simulated for different $x$ with V <sup>3+</sup> , V <sup>4+</sup> , and V <sup>5+</sup> references: Initial distribution (first column), after helium reduction (second column), and after oxygen exposure (third column). . . . .	108
4.32	vanadium L2 and L3 edges spectra simulated of the SVO ( $x = 0$ ) and LVO ( $x = 1$ ) thin film with V <sup>3+</sup> , V <sup>4+</sup> , and V <sup>5+</sup> reference: Initial distribution (first column), after helium reduction (second column), and after oxygen exposure (third column) . . . . .	109
4.33	Summary of the V <sup>3+</sup> , V <sup>4+</sup> and V <sup>5+</sup> variation with lanthanum doping: (a) Initial distribution, (b) after helium reduction, and (c) after oxygen exposure. . . . .	110
5.1	$\theta - 2\theta$ scan of the (002) reflection of the LaCrO <sub>3</sub> (a) and the SrCrO <sub>3</sub> (b) thin films at various deposition temperatures. . . . .	115
5.2	$\theta - 2\theta$ scan of the (002) reflection of $x = 0.33$ solid solution grown at different temperatures (a) and under different oxygen atmospheres (b).116	
5.3	(a) $\theta - 2\theta$ scan of the (002) reflection of the LSCO solid solution grown under optimal deposition parameters, (b) Out-of-plane lattice parameter evolution with the La content. . . . .	117
5.4	(a) X-ray reflectivity of LSCO solid solution samples for selected compositions, and (b) Reciprocal Space Map of the (103) reflection of the La <sub>0.33</sub> Sr <sub>0.67</sub> VO <sub>3</sub> solid solution thin film . . . . .	118
5.5	XPS survey spectra of LSCO solid solution thin films for specific La <sub><math>x</math></sub> Sr <sub>1-<math>x</math></sub> CrO <sub>3</sub> compositions ( $x = 0.33$ bottom panel, 0.5 middle panel, and 0.66 top panel) . . . . .	119

5.6	Core level variation with the lanthanum content: (a) O 1s (b) Sr 3d, and (c) Cr 2p. . . . .	120
5.7	Cr L2,3-edge XAS spectra of $\text{La}_x\text{Sr}_{1-x}\text{CrO}_3$ ( $x = 0.33, 0.50$ and $0.66$ ) (LSCO) thin films grown on single crystal STO substrate. . . . .	121
5.8	(a) Resistivity as a function of temperature of the LSCO solid solution thin films, (b) Room temperature resistivity as a function of lanthanum doping. . . . .	123
5.9	Resistivity as a function of temperature of the $\text{La}_{1-x}\text{Sr}_x\text{CrO}_3$ solid solution thin films taken from [18]. Note the different definition of $x$ , being here the Sr content. . . . .	124
5.10	Room temperature conductivity and hole concentration versus Sr content $x$ adapted from [15]. Note the different definition of $x$ , being here the Sr content. . . . .	125
5.11	Hall resistance slope of SVO and LSCO ( $x = 0.33$ ) . . . . .	126
5.12	Optical transmission of the LSCO solid solution thin films as a function of wavelength (a), and the transmittance of the films with different composition at a wavelength of 550 nm (b). Here, the $x = 0.16$ sample was left out for clarity, where the low transmittance is probably due to experimental problems with the substrate. . . . .	127
5.13	$\theta - 2\theta$ scan of the (002) reflection of $x = 0.33$ and $0.66$ $\text{La}_x\text{Sr}_{1-x}\text{CrO}_3$ solid solution thin films on LAO (a) and LSAT (b). . . . .	129
5.14	Reciprocal space maps of the (103) LSCO films and $\text{LaAlO}_3$ substrate, for (a) $x = 0.33$ and (b) $x = 0.66$ . . . . .	129
5.15	Resistivity as a function of temperature of the LSCO solid solution deposited on various substrates: (a) $x = 0.33$ , (b) $x = 0.66$ . . . . .	130
5.16	Room temperature resistivity of the composition $x = 0.33$ and $0.66$ thin films as a function of the lattice deformation $c/a$ . . . . .	131
5.17	Schematics of the band alignment in a solar cell, and an overview of the work function of different materials including F-doped $\text{SnO}_2$ (FTO) and other materials. . . . .	132

---

5.18 $\theta - 2\theta$ scan of the (002) reflection using double target (parent compound), and mono target with specific LSCO $x = 0.33$ composition. . . . .	133
5.19 $\theta - 2\theta$ scan of LSCO deposited on FTO under different conditions. . . . .	134
5.20 Kelvin Probe Force Microscopy (KPFM) measurements for a $x = 0.33$ thin films deposited from two targets at 500 °C (a) surface topography, (b) work function distribution. . . . .	136
5.21 Optical transmission of LSCO thin films deposited on FTO under different growth parameters. . . . .	137
6.1 Graphical representation of figure of merit (electrical resistance and optical transmission) for the LSVO and LSCO thin films in comparison with other typical TCO's. . . . .	141

---

## List of Tables

---

5.1	Table of the deformation $c/a$ of two different $\text{La}_x\text{Sr}_{1-x}\text{CrO}_3$ compositions . . . . .	130
-----	---	-----



# CHAPTER 1

---

## General introduction

---

The use of Transparent Conducting Oxides (TCOs) has become a fundamental aspect within the realm of material science, owing to their exceptional combination of properties namely, excellent electrical conductivity as well as high optical transparency. These properties have contributed to their use in multiple applications, including solar cells, touch screens, light-emitting diodes, and more. Traditional TCOs are typically semiconductor-based, using materials such as Indium Tin Oxide (ITO) or Aluminum-doped Zinc Oxide (AZO). The biggest challenge now is finding the right balance between high electrical conductivity and optical transparency since we want the light to pass through a TCO without important reflection or absorption. The objective is mainly to minimize the scattering of the free carriers while at the same time making sure the light is transmitted in the visible range (energy < 1.75 eV) as introduced in the following expression of the screened plasma frequency, determining the absorption onset of the carriers:

$$\omega_p^* = \frac{e}{\epsilon_0 \epsilon_R} \sqrt{\frac{n}{m^*}} \quad (1.1)$$

where  $e$  is the electronic charge,  $\epsilon_0$  and  $\epsilon_R$  the vacuum and the relative dielectric constant, respectively.  $n$  is the charge carrier density and  $m^*$  is the effective mass.

Based on the screened plasma frequency, in the semiconductor approach, the idea is to dope a wide bandgap material in order to increase the carrier concentration  $n$ . Regardless of their industrial success, these materials have specific disadvantages such as high production costs, limited abundance of critical elements, and challenges in achieving efficient p-type TCOs. Recently, an interesting evolution has been introduced in TCO research with the emergence of a new approach based on correlated metals, exhibiting distinctive electronic and optical characteristics due to their strong electron-electron interactions. This approach has the potential to overcome some of the limitations of semiconductor TCOs, providing an alternative way to synthesize high-performing, cost-effective TCOs, and more significantly, enabling the development of efficient p-type TCOs - a challenge in the field. In this approach, using correlated metals ensures the high carrier concentration, but also the control of the effective electron mass  $m^*$  in order to have a transparent material, while keeping excellent electrical properties.

Two interesting candidates for various technological advancements are lanthanum strontium vanadium Oxide (LSVO) as an n-type TCO and lanthanum strontium chromium Oxide (LSCO) as a p-type TCO. The objective of this thesis is to prepare high quality thin films of these two perovskite-based materials in order to explore the optimization of the TCO properties through charge doping via the La/Sr content and through control of strain via the use of different substrates. Chapter 2 provides a comprehensive overview of the current advancements in perovskite-based materials, specifically highlighting LSVO and LSCO. The importance of these materials in emerging technologies is highlighted, with particular emphasis placed on their structural, electrical, and optical characteristics.

Following this, Chapter 3 presents the methodology used for the preparation and characterization of the thin films, the relevant parameters and the main analysis methods. The intention of this chapter is to introduce the working principle of the techniques and technical approaches used in this thesis, as well as to describe the data treatment and analysis.

Chapter 4 of this manuscript focuses on the investigation of thin film solid solutions of lanthanum-doped strontium vanadium Oxide (LSVO). Our objective is to establish the structural, electronic and optical properties upon doping and to determine the optimal level that enhances material performance for the use as TCO. The effects of strain engineering on the LSVO thin films are also examined, assessing its contribution to the optimization of the film properties and material functionalities. After the report of a p-type conducting phase in LSVO thin films, a special focus will be put on the type of charge carriers in this study.

In Chapter 5, the attention is directed towards thin film solid solutions of lanthanum-doped strontium chromium Oxide (LSCO), a p-type TCO. Again, the influence of La-doping on the structural, optical and electrical characteristics of the films will be investigated, as well as the impact of strain engineering. Furthermore, the integration of LSCO with state-of-the-art materials used in photovoltaic applications will provide insights on the potential of the material for specific applications.

In summary, this thesis investigates the optimization of LSVO and LSCO performance by means of deliberate lanthanum doping and strain manipulation. Our objective is to enhance our knowledge of the fundamental mechanisms that govern the properties of these materials, with the intention of making significant contributions to their potential applications in various technological fields such as electronic devices. The findings of this study exhibit the potential to customize perovskite-derived materials for particular applications, and the knowledge acquired will contribute to the wider comprehension of the design and engineering of a new type of promising TCOs.



## CHAPTER 2

---

### State of the art

---

This chapter will review the most relevant aspects of TCOs and the investigated perovskite solid solutions, that are directly relevant to the scientific work of this thesis. Although there exists significant literature documentation on the topic of LSVO and LSCO bulk materials and their parent compounds, it is impractical to encompass all aspects within a single review. The aim is to focus on the fundamental structural, electrical, and optical characteristics, which play a key part in comprehending their viability as transparent conducting oxides (TCOs).

## 2.1 Transparent conducting oxide

Prior to delving into the potential application of correlated metals as a transparent conducting oxide (TCO), it is necessary to provide a comprehensive overview of the history of TCOs. Transparent conducting oxides represent a unique category of materials that exhibit a combination of electronic conductivity and optical transparency. This combination of properties is essential in various applications such as solar cells [30], touch screens [31], light emitting diodes [32], intelligent windows [33], infrared plasmonics [34] and transparent electronics [32]. The investigation of TCOs has persisted for over a century due to their significant practical applications. Baedeker successfully synthesized the initial TCO thin film in 1907 through the process of thermal oxidation of a Cd film under vacuum, as documented in [35].

Despite exhibiting excellent electron mobility, this TCO is not largely used due to its toxicity. The initial major production of TCOs occurred during the Second World War, wherein  $\text{SnO}_2$  doped with Sb was utilized as a transparent coating glazing material for aircraft windshields. [36] At present, the TCO industry relies on wide bandgap post-transition metal oxides that are degenerately doped with n-type carriers, such as F-doped  $\text{SnO}_2$  and Al-doped ZnO. However, Sn-doped  $\text{In}_2\text{O}_3$  (ITO for Indium-Tin-Oxide) is the most commonly used material, accounting for 90% of the market share for over six decades [37]. The exceptional electrical conductivity of ITO coupled with its high optical transmittance of over 80% is the reason for this massive use. The electrical conductivity of ITO can reach up to  $10^4 \text{ Scm}^{-1}$ . The current state of rising costs of raw materials has prompted extensive research efforts toward identifying alternative options to ITO.

Furthermore, the constitution of transparent electronics and its fundamental building blocks such as p-n junctions, was constrained due to the absence of p-type TCOs with the necessary performances. This was attributed to the challenge of incorporating acceptors into the intrinsic electronic structure of the TCOs, as indicated by previous research [38]. The concept of chemical modulation of the valence band through the hybridization of O 2p orbitals with Cu 3d orbitals was

introduced by Hosono et al in 1997 [39]. The observed phenomenon facilitated a significant degree of dispersion within the valence band, thereby resulting in a reduction in the localization of holes. A multitude of p-type TCOs were formulated utilizing  $\text{Cu}^{2+}$  oxides, specifically of the delafossite type, following this approach. As a result, the p-n junction became a feasible prospect. The initial discovery of the delafossite TCO  $\text{CuAlO}_2$  was made by Hosono et al, who observed a p-type conductivity of  $1 \text{ Scm}^{-1}$  [40]. The aforementioned findings prompted a thorough exploration of numerous delafossite  $\text{CuMO}_2$  compounds (where M represents B, Al, Cr, Ga, Sc, In, or Y) using various deposition methodologies, including Pulsed Laser Deposition, Sputtering, and Molecular Beam Epitaxy. Some of the most promising delafossites include  $\text{CuCrO}_2$ , which exhibits a remarkably high conductivity of up to  $220 \text{ Scm}^{-1}$  [41], and  $\text{CuInO}_2$ , which features bipolar doping [40]. Notwithstanding the commendable electronic proficiency exhibited by delafossites, their optical transmittance falls short of being satisfactory (30 %) and their structural stability is low. Analogously, extensive exploration efforts have been conducted on alternative p-type compounds, including chalcogenides (such as  $\text{Cu}_x\text{Zn}_{1-x}\text{S}$ , where  $x = 0.35$ ) that exhibit electrical conductivity values of up to  $261 \text{ Scm}^{-1}$  and optical transmittance of 58 % [42]. Additionally, spinel oxides have been investigated using the same approach of chemical modulation of the valence band [43]. However, the p-type TCOs proved insufficient in terms of the electrical and optical performances compared to the current n-type TCOs.

The underlying concept of the aforementioned TCOs involves the enhancing of carrier concentration in a semiconductor with a wide bandgap through the process of doping. A novel alternative approach has been suggested by L. Zhang et al for generating TCOs with high electrical conductivity and optical transparency through the utilization of strong electronic correlations [1]. Such materials, namely  $\text{SrVO}_3$  (SVO) and  $\text{CaVO}_3$  (CVO), possess a significantly high concentration of carriers, reaching up to  $2 \times 10^{22} \text{ cm}^{-3}$ , thereby surpassing the semi-conducting TCOs by two to three orders of magnitude. Most of the scientific activities are centered on the 'classical' materials SVO [7, 13, 14, 19, 44–49] and CVO [1, 50–52], but also  $\text{SrNbO}_3$  [49, 53, 54] or  $\text{SrSnO}_3$  [55] have attracted interest. In general, metals exhibit

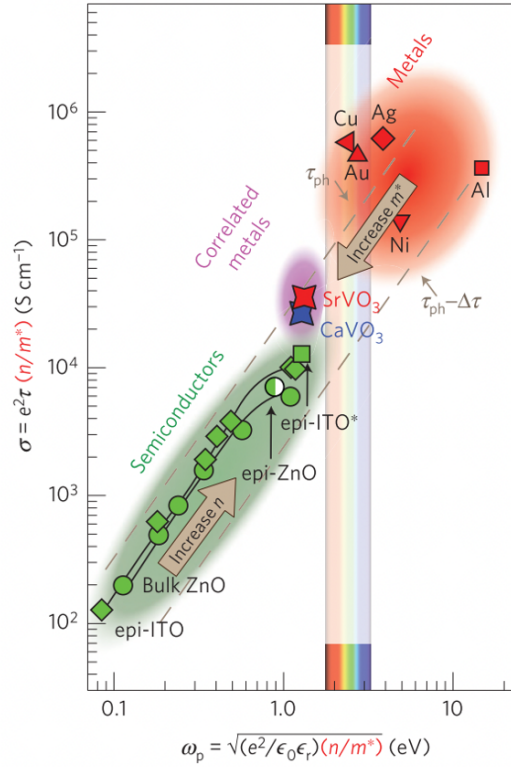


Figure 2.1: Conductivity  $\sigma$  vs screened plasma frequency  $\omega$  of different semiconductor TCOs, metals and correlated metals. Taken from reference [1]

a high electrical conductivity due to the presence of a high number of free charge carriers. These carriers absorb light with a plasma frequency above or in the visible range, thereby resulting in optical opacity. Conversely, a material that exhibits optical transparency is in most cases characterized by a limited quantity of free charge carriers, allowing to avoid the plasma oscillation, but thereby rendering it an electrical insulator. In correlated metals, as proposed by Zhang et al, a high number of free charge carriers is achieved while simultaneously minimizing their photon absorption as presented in Figure 2.1 [1].

### 2.1.1 Band structure differences for correlated metals

Before delving into the main chapters of this thesis, it is important to establish a fundamental understanding of the transparency properties in both correlated metals and semiconductors. These two classes of materials exhibit distinct behaviors related

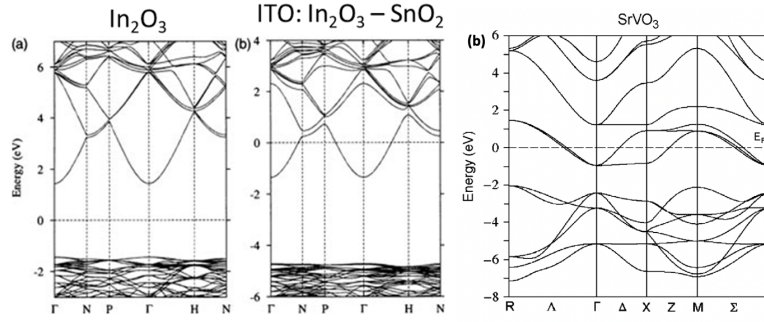


Figure 2.2: Band structure of (a) ITO and (b) SVO. Taken from reference [2]

to their bandgap and electronic correlations, which have significant implications for their optical properties. Gaining insight into these aspects will serve as a crucial foundation for the subsequent exploration of the topics and findings presented in this research. Transparency in semiconductor thin films, particularly in the context of their bandgap, is a fundamental property that has profound implications for various optoelectronic applications. The bandgap represents the energy difference between the valence and conduction bands in a semiconductor, and it determines the material's ability to absorb or transmit light. In semiconductors, transparency is associated with bandgaps that fall within the visible range of the electromagnetic spectrum, allowing these materials to transmit and interact with light in this range. However, in correlated metals, a different mechanism comes into play. The transparency of correlated metals, often referred to as correlated transparency, is distinct from that of semiconductors. This phenomenon arises due to the strong electronic correlations among the constituent electrons in these materials. These correlations lead to a shift in the optical reflection limit, pushing it outside the visible range, thus rendering correlated metals transparent in a manner that is fundamentally different from conventional semiconductors.

Figure 2.2 provides a direct comparison between a typical semiconductor, namely Indium Tin Oxide (ITO), and a correlated metal transparent oxide, strontium vanadium Oxide (SVO). This visual representation underscores the fundamental differences in their band structures. In the case of ITO, a clear and distinct bandgap is evident, and this bandgap is the primary reason for its transparency. The bandgap in semiconductors creates a region where there are no available electronic states for

absorbing light within the visible spectrum, hence allowing light to pass through. On the other hand, in the case of SVO, there is no discernible bandgap, and the conduction bands are closely packed together, leading to a different mechanism for transparency. In the case of SVO, transparency arises from the shift of the optical reflection limit outside the visible range. The strong electronic correlations within SVO drive this shift, resulting in the material being transparent despite the absence of a traditional bandgap.

## 2.2 Perovskite Oxides

Perovskite oxides are a distinctive category of materials that has been extensively studied for a considerable duration. The discovery of the first perovskite structure material  $\text{CaTiO}_3$  is attributed to the geologist Gustav Rose in 1839 [56]. In recognition of the contributions made by the Russian mineralogist Von Perovski, Rose named this class of materials after him. The perovskite structure has since been found to be a common feature in a wide range of functional materials, including superconductors, catalysts, and photovoltaics [57]. Perovskite oxides are characterized by the chemical formula  $\text{ABO}_3$ , wherein A and B represent two distinct cation sites and oxygen serves as the anion. Cation A occupies the edge positions of cuboctahedra, coordinated with twelve  $\text{O}^{2-}$  ions. Cation B is in an octahedral coordination with six  $\text{O}^{2-}$  ions, as presented in Figure 2.3 (a).

Cation A is typically an alkaline element and cation B a transition metal. The intrinsic properties of these materials are directly influenced by the type and size

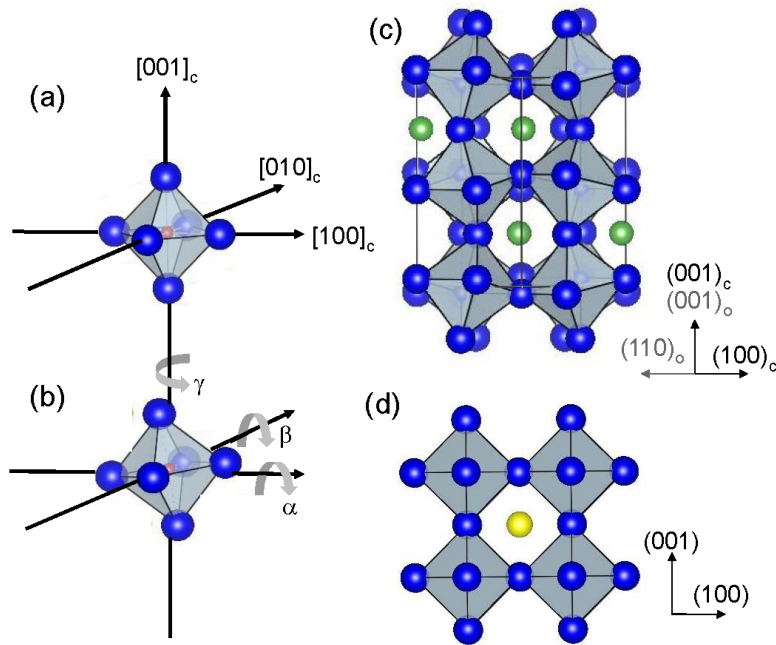


Figure 2.3: The perovskite structure: (a) constituting octahedra in the cubic phase with the orientations using Miller indexes, (b) rotation of octahedra for tolerance factors  $t \neq 1$ , (c) orthorhombic distortion of the cubic perovskite structure, (d) cubic perovskite structure. Taken from reference [3]

of the cations present. The effect of diversification of sizes has been observed to result in a distortion or rotation of the  $\text{BO}_6$  octahedron (Figure 2.3 (b)), thereby reducing the cubic symmetry Pm3m and giving rise to orthorhombic, tetragonal or monoclinic structural variations [58]. The extent of this distortion can be quantified by employing Goldschmidt tolerance factor  $t$  [59]:

$$t = \frac{r_A + r_O}{\sqrt{2}(r_B + r_O)} \quad (2.1)$$

Where  $r_A$ ,  $r_B$  and  $r_O$  are the radius of the A and B cations and oxygen, respectively.  $t$  can be used to approximate the degree of deviation from the state of ideal, cubic symmetry ( $t = 1$ ). For  $t$  values within the range of 0.89 to 1, the structure adopts a cubic configuration. However, for values of  $t$  less than 0.89, the structure changes into a orthorhombic, rhombohedral, or tetragonal arrangement. Finally, for values of  $t > 1$ , the structure assumes a hexagonal configuration.

For thin films, often a pseudo-cubic lattice parameter  $a_{pc}$  is calculated in the case of slightly distorted perovskite structures.  $a_{pc}$  is used to compare the significant lattice distances of the film with those of the substrate and evaluate the metrical misfit. The exact way of calculating  $a_{pc}$  depends on the type of structural distortion of the cubic symmetry and the relative crystallographic orientations of the film and the structure, and will be detailed when applied in this thesis.

The octahedral site holds significant importance in perovskite oxides and has the potential to influence its physical properties. The electronic behavior of the  $\text{ABO}_3$  system is determined by the interactions between the d states of the transition metal B and the 2p states of oxygen, governed by their bond length, i.e. related to the lattice parameter, and angle, i.e. related to possible structural distortions. Furthermore, the electronic properties of the perovskite can be regulated by the substitution of B cations with varying oxidation degrees, thereby facilitating electronic doping. Such effects can also be obtained by the substitution of the A-site cations [60]. Again, size changes may lead to the distortion of the structure and therefore to the B-O bond length and angle, and valence changes will lead in most cases to a change of the B-site oxidation state due to the charge neutrality.

In thin films, another possibility exists to modify the bond lengths and angles,

---

using epitaxial strain. Therefore, the deposition of  $ABO_3$  perovskites on different substrates may influence strongly the observed physical properties.

## 2.3 Epitaxial strain

The selection of a suitable substrate is of utmost importance in the process of thin film deposition, as the quality of the resulting film crystal structure is dependent upon both the degree of structural compatibility and lattice agreement. The lattice constant of perovskite oxides typically falls within the range of 3.7 to 4.20 Å, as illustrated in Figure 2.4. [4]

Epitaxial strain arises when the lattice parameter of a thin film deviates slightly from that of the substrate. Thin films may exhibit structural and atomic adaptations to their respective substrates, resulting in mechanical strains and consequential structural alterations such as tilting and distortion of the octahedra. The resulting epitaxial misfit can be mathematically expressed as  $\sigma = \frac{a_s - a_f}{a_s}$ , where  $a_s$  and  $a_f$  represent the in-plane lattice constants of the substrate and the film, respectively. This factor enables the identification of the type of strain and facilitates its quantification. In the case where the lattice constant of the film is greater than the substrate, it will be subjected to compressive strain. As a result, the octahedral  $\text{BO}_6$  will attempt to alleviate this strain by means of rotations and/or the adjustment of the distance between B and O. This will consequently cause a modification in the B-O-B angle and elastically the out-of-plane lattice parameter of the film  $c_f$ . If the lattice constant of the film is smaller than the substrate, the film will undergo tensile strain. This, in turn, may result in a shorter  $c_f$ , as illustrated in Figure (2.5) [5]. However, in

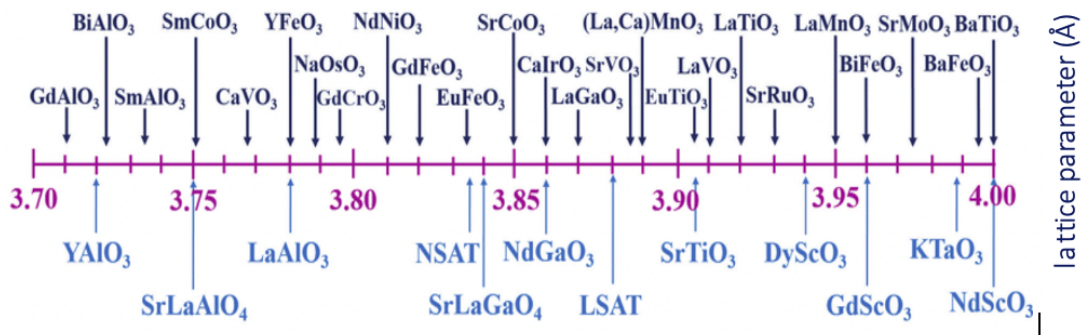


Figure 2.4: The lattice constant of different perovskite oxides. Taken from reference [4].

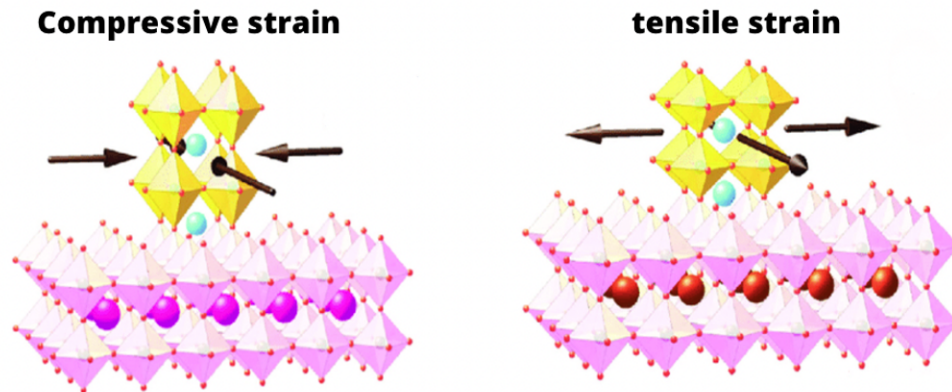


Figure 2.5: Illustration of the adaptation of the film perovskite unit cell to compressive and tensile strain. Taken from reference [5].

this case, it is not possible to adapt an initially cubic structure by the introduction of rotations, and the distortion of the octahedra is the only possible adaptation.

The use of epitaxial strain has been shown to be an effective technique for manipulating the characteristics of diverse transition metal oxides [5,61–67]. Epitaxial strain can be utilized to modulate electrical resistivity and induce metal-insulator transitions in manganites, such as  $\text{La}_{1-x}\text{Sr}_x\text{MnO}_3$  [68,69]). Epitaxial strain has been employed also to manipulate the electrical and structural characteristics of ruthenates such as  $\text{SrRuO}_3$  in a similar manner [70–72]. The aforementioned approach has been implemented in the manipulation of electronic characteristics of  $\text{LaNiO}_3$  [66], and  $\text{SrVO}_3$  [29].

## 2.4 Perovskite Vanadates

vanadium-based  $AVO_3$  perovskite oxides exhibit interesting properties and hold potential for deployment in a variety of advanced technological domains, including photovoltaics, smart windows, and superconductivity [73]. These oxides are characterized by an electronic configuration with partially filled 3d orbitals, wherein the oxidation state of V may fluctuate dependent upon the oxygen stoichiometry or the A cation. In cases where the A cation is a trivalent species, such as lanthanum or rare earth elements, the V cation assumes a  $3d^2$  configuration, indicating the presence of two electrons in its 3d orbitals. On the other hand, in cases where the A cation is divalent, such as with alkaline earth metals, the configuration of the V cation is  $3d^1$ .

This variation in electronic configuration results in a range of electronic and magnetic characteristics within  $AVO_3$  perovskites. The perovskite oxides exhibit a conduction mechanism that entails the involvement of indirect exchange interactions enabled by the oxygen O 2p orbitals. The covalent bonds between oxygen atoms and transition metal cations, such as V, are strong, and the 2p orbitals of oxygen atoms are crucial in enabling charge transfer and electron conduction within the crystal structure. The conduction mechanism can be effectively explained by the Hubbard model (Figure 4.7), which accounts for the strong electron-electron interactions within the 3d orbitals of the transition metal cations. The transfer of localized charges from one V ion to the next is governed by two distinct forms of energy: the charge hopping energy ( $t$ ), which is responsible for the movement of charges from one vanadium atom to another, and the Coulomb repulsion energy ( $U$ ), which arises from the mutual repulsion of two electrons occupying the same atomic site. In transition metal oxides, a contest arises between  $U$  and  $t$ , which may result in a Mott metal-insulator transition (MIT). In the case where the hopping energy  $t$  exceeds the repulsion energy  $U$  (left part of Figure 4.7), the conduction band will feature a high density of states at the Fermi level, the so-called quasi-particle band. This will be reflected in the optical conductivity, which will exhibit three optical transitions, namely the Drude peak, an intra-band peak related to a 3d-3d transfer, and an

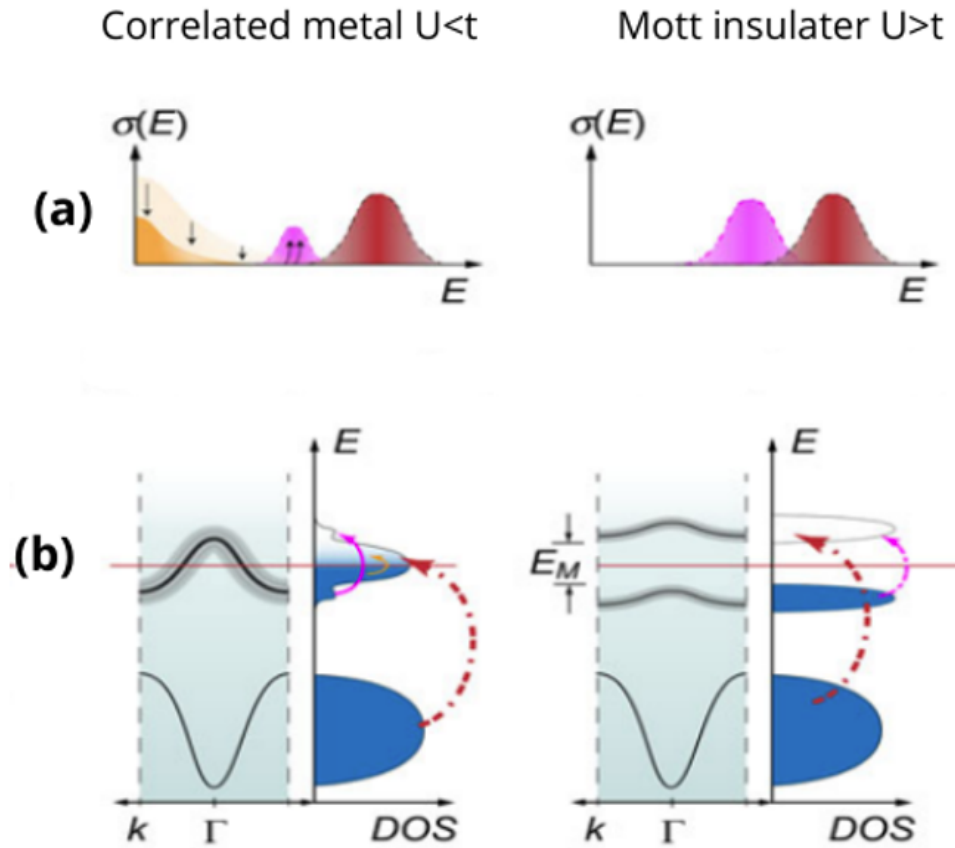


Figure 2.6: Illustration of the optical conductivity (a) and the band structure (b) of a strongly correlated metal ( $U < t$ ) and a Mott insulator ( $U > t$ ). Adapted from reference [6]

inter-band transition related to the 2p-3d transfer. Additionally, the material will display a metallic character of the electronic conduction [74].

The second scenario involves the manifestation of a MIT phenomenon, wherein  $U$  takes precedence over  $t$  (right side of Figure 4.7). Here, the repulsion of the charge carriers leads to the opening of a gap at the Fermi level of the material, the so-called Mott gap, and the splitting of the quasi-particle band in a Lower and an Upper Hubbard Band. Therefore, in the optical conductivity, the Drude peak related to the mobile charge carriers disappears and the spectral weight is shifted to the intra-band peak. Electrically, the material is insulating.

The strontium Vanadate ( $\text{SrVO}_3$ , SVO) is an example of a strongly correlated metal with  $U < t$ . It demonstrates a cubic crystal structure characterized by Pm3m

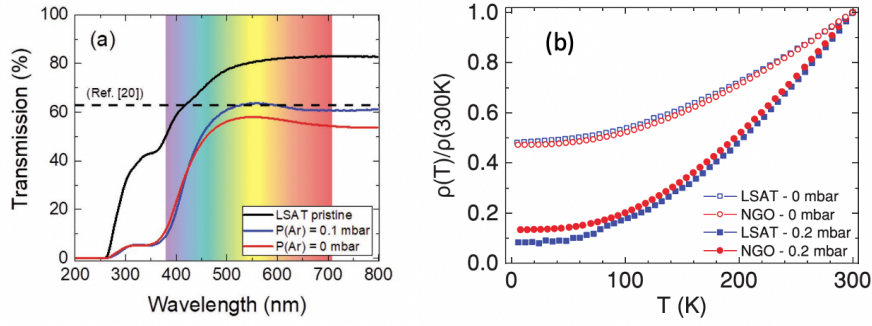


Figure 2.7: (a) Optical transmittance of SVO films on LSAT, about 50 nm thick, deposited either at  $P(\text{Ar}) = 0$  mbar (red) or at  $P(\text{Ar}) = 0.1$  mbar (blue) (b) Temperature dependence of the normalized resistivity  $\rho(T) / \rho(300 \text{ K})$  for SVO films on LSAT and  $\text{NdGaO}_3$  substrates. Taken from reference [7]

symmetry. The lattice parameter is measured to be  $a = 3.84 \text{ \AA}$ . It exhibits vanadium in a  $\text{V}^{4+}$  oxidation state, which is defined by a  $3d^1$  electron configuration in which one electron occupies the  $3d t_{2g}$  orbital. This electronic configuration offers a conductive electrical property. Regarding magnetism, it has been observed that the stoichiometric compound exhibits a Pauli behavior when the temperature exceeds 200 K [75]. The bulk SVO shows a stable electrical properties regarding the oxygen deficiency, as demonstrated in the study by P.Dougier [76], as the oxygen-deficient strontium Vanadate ( $\text{SrVO}_{2.9}$ ) exhibits almost similar metallic behavior to the stoichiometric  $\text{SrVO}_3$ . They also studied the optical properties with a focus on the screened plasma frequency, revealing that the value for stoichiometric compound is 1.36 eV and for the oxygen deficient compound around 1.20 eV.

Delving more into the structural, electrical and optical properties of the SVO thin films, Mathieu Mirjolet et al [7] demonstrate a successful growth strategy by the use of a nonreactive gas during a pulsed laser deposition process for obtaining high-quality  $\text{SrVO}_3$  films with low resistivity, large carrier mobility, and improved optical transparency as presented in the Figure 2.7. The room temperature resistivity values are  $31 \mu\Omega\text{cm}$  ( $\text{SrVO}_3$  grown on  $\text{NdGaO}_3$  (001)) and  $38 \mu\Omega\text{cm}$  ( $\text{SrVO}_3$  grown on  $(\text{LaAlO}_3)_{0.3}(\text{Sr}_2\text{TaAlO}_6)_{0.7}$  (001), LSAT) for about 50 nm thickness.

Many studies explored SVO as a potential transparent conducting oxides. Haiying He et al [77] examined the properties and characteristics of SVO emphasizing

its high electrical properties, which arise from electron interactions. SVO exhibits a carrier concentration of  $2.2 \times 10^{22} \text{ cm}^{-3}$ , conductivity of  $10^4 \text{ Scm}^{-1}$  and a plasma frequency of 1.33 eV. It is worth noting that the properties of the SVO are highly affected by the growth conditions, the substrate, and crystalline quality and the good stoichiometry. For example, SVO deposited by Pulsed Laser Deposition (PLD) on  $\text{SrTiO}_3$  (001) has a resistivity of  $0.187 \times 10^{-5} \text{ } \Omega\text{cm}$  [13], while SVO deposited on LSAT by Molecular Beam Epitaxy (MBE) has a resistivity of  $3 \times 10^{-5} \text{ } \Omega\text{cm}$  [1], and SVO deposited on LSAT by sputtering is showing a resistivity of  $0.2 \times 10^{-5} \text{ } \Omega\text{cm}$  [47]. It is also worth noting that the epitaxial strain and carrier concentration allow fine tuning of optical properties of  $\text{SrVO}_3$  films by modulating the effective mass  $m^*$  due to strain-induced symmetry [13, 29].

Gabriele Sclauzero et al aimed to understand the Mott metal-insulator transition (MIT) in perovskite systems that contain transition metal cations with  $d^1$  and  $d^2$  electron configurations. [78] The selection of  $\text{SrVO}_3$  as one of the three representative materials was made in order to investigate the impact of epitaxial strain on the Mott transition. The aforementioned strain (chapter 2.3) has the capability to modify both the physical and electronic characteristics of the material, thereby offering a mechanism to precisely adjust its performance. This theoretical study has shown that compressive strain may be used on SVO thin films in order to approach the metal-insulator transition. Another theoretical study by A. Paul and T. Birol [79] concerns the evolution of the optical properties, and especially the screened plasma frequency  $\omega_p^*$ , under strain. It is shown that this magnitude, determining the transparency window of the TCO, shifts to lower values under tensile strain, while compressive strain leads to an increase.

Takuji Maekawa et al investigated the mechanical, thermal, and electrical characteristics of polycrystalline  $\text{SrVO}_3$ . [80] According to the findings of the study,  $\text{SrVO}_3$  exhibits metallic behavior over the whole temperature spectrum. Furthermore, the material exhibited values of the Seebeck coefficient that were negative, suggesting that electrons constitute the vast majority of charge carriers.

Vincent Polewczyk et al [19] focused on the surface stability of SVO under various atmospheres. It has been demonstrated that there is a formation of a Sr-rich  $\text{V}^{5+}$

layer on the surface over time, which can be removed by a water treatment. This surface oxidation enhances the understanding of aging effects in perovskite oxides.

Yakel, Bertaut, Forrat, and Geller were the initial researchers in the structural analysis of rare earth-based Vanadates  $RVO_3$  [81]. In these studies, it was established that the structures of  $RVO_3$  (where R ranges from Pr to Lu) and  $LaVO_3$  compounds are orthorhombic and identical to those of  $GdFeO_3$ , respectively.  $LaVO_3$  adopts an orthorhombic structure at room temperature with lattice parameters  $a_o = 5.555 \text{ \AA}$ ,  $b_o = 5.553 \text{ \AA}$ ,  $c_o = 7.848 \text{ \AA}$ , and  $\alpha = 90^\circ$ .  $LaVO_3$  will be referred to as being associated with a pseudo-cubic structure (as introduced in chapter 2.2) in the discussion that follows, with the lattice parameters  $c_{pc} = a_o/\sqrt{2} = b_o/\sqrt{2} = c_o/2 = 3.925 \text{ \AA}$  ( $o$  and  $pc$  denoting orthorhombic and pseudo-cubic cells, respectively). It undergoes a structural transition at 141 K and takes on a monoclinic structure with  $a_m = 5.591 \text{ \AA}$ ,  $b_m = 5.562 \text{ \AA}$ ,  $c_m = 7.751 \text{ \AA}$ , and  $\alpha = 90.129^\circ$  [82].

At this temperature, a new magnetic state appears and the octahedra are shown to rotate stabilizing an orbital order (see Figure 2.3). Rogers and al demonstrated that the  $LaVO_3$  compound exhibits a semiconductor behavior in the 120 – 670 K range with an activation energy of around 0.2 eV [83]. T. Arima and Y. Tokura investigated the optical characteristics and reported a number of optical transitions inside  $LaVO_3$  (Figure 2.8). Charge transfer from the oxygen 2p orbital (O 2p) to the vanadium 3d orbital (V 3d) is associated with two high-energy photonic transitions [8].

Regarding the physical properties of  $LaVO_{3-\delta}$  ( $\delta = 0.08$ ) with oxygen deficiency, it has been demonstrated that it maintains the identical crystal structure as the stoichiometric  $LaVO_3$  [84]. Additionally, it displays a semiconducting characteristic comparable to that of the stoichiometric compound, indicating that the vacancy-induced charge carriers remain confined.

The initial achievement of synthesizing  $LaVO_3$  in the form of a thin film was carried out by W. Choi et al [85]. The deposition of the material onto a  $LaAlO_3$  substrate with a (001) orientation ( $a_{pc} \approx 3.79 \text{ \AA}$ ) was carried out using pulsed laser deposition. The target utilized in this process was  $LaVO_4$ . The epitaxial growth of  $LaVO_3$  was carried out with great precision under a meticulously controlled reduc-

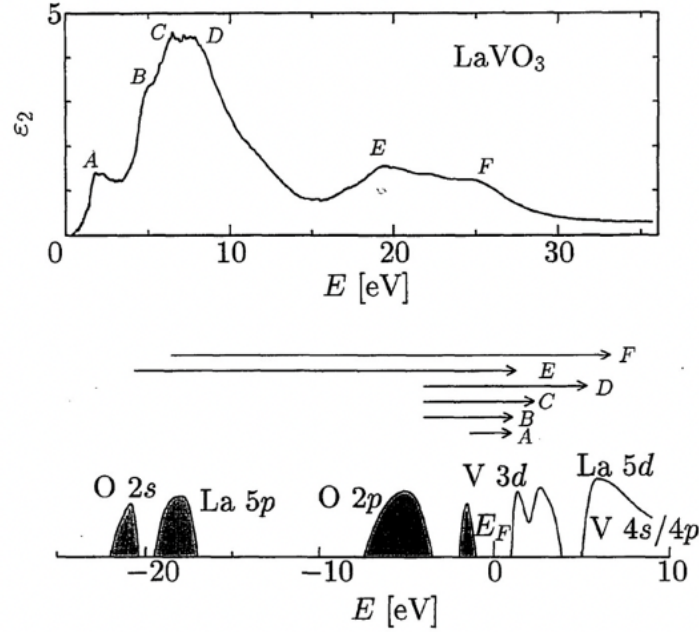


Figure 2.8: Variation of the dielectric function of LVO with energy. Illustration of the electronic structure indicating the different excitations related to the optical transitions. Taken from reference [8]

ing atmosphere at a temperature of 500 °C. Upon conducting an X-ray diffraction analysis of the thin film, the film displayed two distinct out-of-plane orientations, namely  $(110)_o$  and  $(001)_o$ , when it was deposited under vacuum. The present study reveals that the observed diverse orientation is significantly associated with a lattice mismatch of approximately 3.5 % between the substrate and the film. Nevertheless, the emergence of a secondary phase related to (201)-oriented  $\text{LaVO}_4$  was observed upon the utilization of high oxygen pressure. The phenomenon was further investigated by Hotta et al, who analyzed the  $\text{LaVO}_3$  composition variation in relation to growth temperature and pressure (Figure 2.9) [86]. A comprehensive approach involving electron energy loss spectroscopy (EELS) and scanning transmission electron microscopy (STEM) was utilized in order to gain a deeper comprehension of this intricate subject. The focus of their inquiry was on the deposition of  $\text{LaVO}_3$  onto a substrate of  $\text{SrTiO}_3$  (001) while operating under conditions of high oxygen pressure, ranging from approximately  $10^{-5}$  to  $10^{-4}$  mbar. The study revealed the existence of  $\text{V}^{5+}$  in three-dimensional islands of  $\text{LaVO}_4$  [9], as depicted in Figure 2.9.

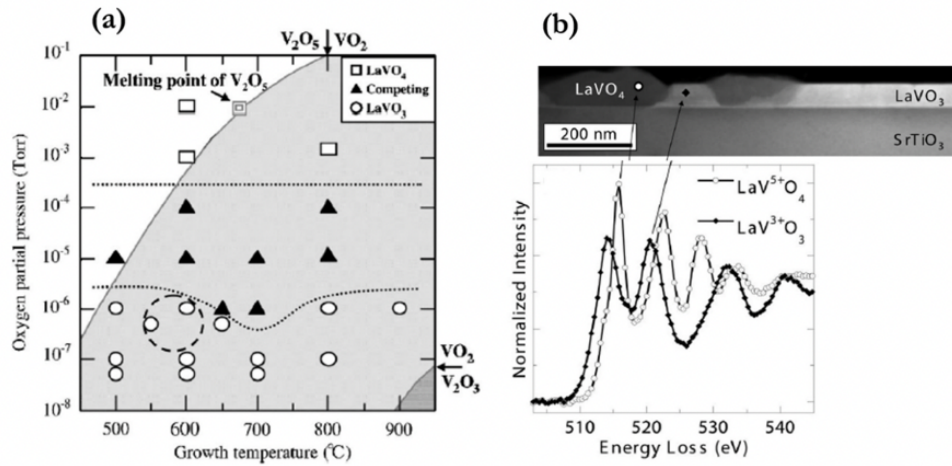


Figure 2.9: (a) Phase diagram of  $\text{LaVO}_x$  under different deposition conditions, (b) Annular dark-field electron microscopy (ADF) showing the presence of 3D  $\text{LaVO}_4$  islands in the  $\text{LaVO}_3$  film. Taken from reference [9]

The aforementioned critical observation has validated that the preparation of a stoichiometric  $\text{LaVO}_3$  thin film needs the utilization of growth conditions characterized by high temperature and low oxygen pressure.

Focusing more into the development of efficient solar cells with Mott insulators, Hai-Tian Zhang et al [10] have grown high quality  $\text{LaVO}_3$  thin films using hybrid

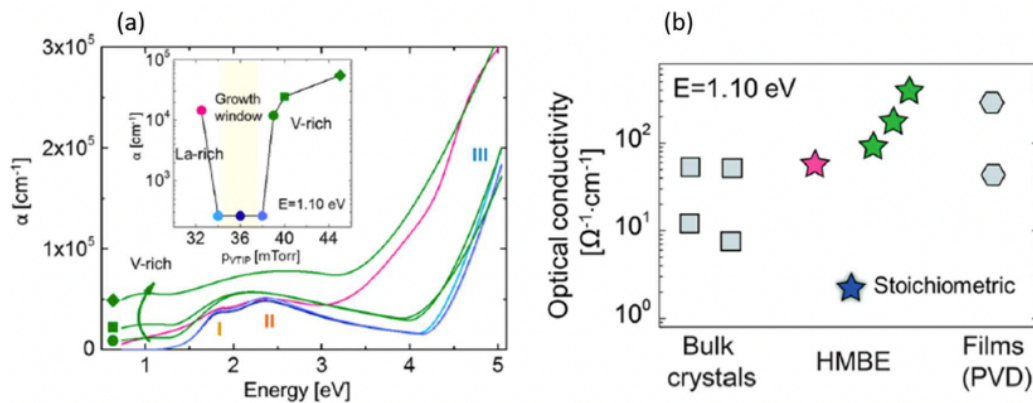


Figure 2.10: (a) Absorption coefficient values of vanadium-rich LVO (green symbols), lanthanum-rich LVO (pink symbols), and stoichiometric LVO (blue symbols), (b) The optical conductivity of bulk LVO compared to LVO deposited by HMBE and LVO deposited by PVD. Taken from reference [10]

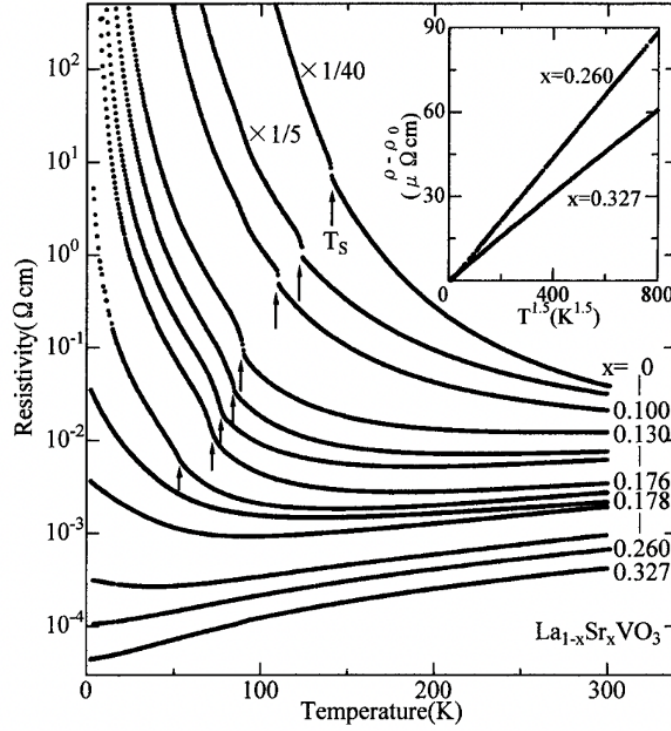


Figure 2.11: Temperature dependent resistivity for a single crystal of the solid solution  $\text{La}_{1-x}\text{Sr}_x\text{VO}_3$ . Taken from reference [11]

MBE in order to investigate the impact of cation stoichiometry on structural, optical, and electrical properties (Figure 2.10). Stoichiometric films demonstrated a high structural quality and low defects, while nonstoichiometric films exhibited an increase in defect concentration. H Rotella et al [87] focused on the influence of growth temperature on the characteristics of the films. The samples demonstrated a significant electronic mobility and a non-linear Hall effect when subjected to low temperatures.

Regarding the solid solution  $\text{La}_{1-x}\text{Sr}_x\text{VO}_3$ , it retains the perovskite structure, and shows a transformation from its parent compound  $\text{LaVO}_3$ , a Mott-Hubbard insulator that exhibits an antiferromagnetic transition, to  $\text{SrVO}_3$ , a paramagnetic metallic conductor (Figure 2.11) [11]. The Mott-Hubbard insulating phase of  $\text{LaVO}_3$  decreases swiftly as the Sr concentration rises, and a change to a metallic state occurs. When the insulating phase no longer exists at the critical concentration, which is commonly found at  $x \approx 0.178$ . The Mott gap disappears due to the decreased charge density. The addition of  $\text{Sr}^{2+}$  leads to an increased part of  $\text{V}^{4+}$  ions with

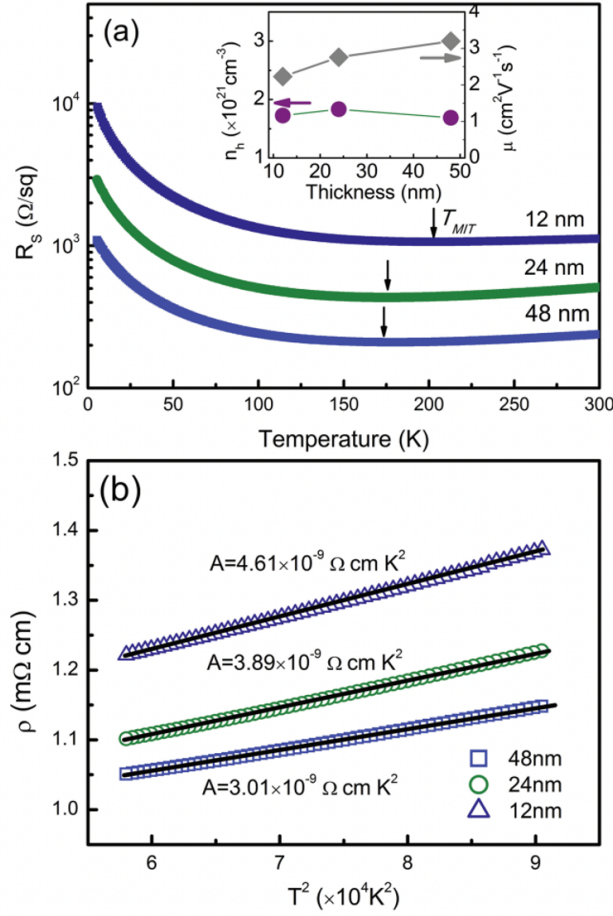


Figure 2.12: (a) Temperature-dependent sheet resistance of the LSVO thin films. (b) Resistivity versus  $T^2$  using the Fermi liquid model in the metallic region for the LSVO thin films. Figures taken from reference [12]

a  $3d^1$  configuration, lowering the charge density, and the resulting lower Coulomb interaction  $U$  (see chapter 2.4) becomes smaller than the hopping  $t$ . Therefore, for  $x \gtrsim 0.18$ ,  $\text{La}_{1-x}\text{Sr}_x\text{VO}_3$  becomes a correlated metal.

Due to its distinctive combination of electrical conductivity and optical transparency, LSVO has recently attracted attention as a conducting transparent oxide. As the bulk LSVO exhibits n-type conduction as was confirmed by measurements of Seebeck coefficient and electrical measurements [11,27,88],  $\text{La}_{2/3}\text{Sr}_{1/3}\text{VO}_3$  thin films deposited on LSAT have been reported to be p-type [12]. At ambient temperature, the conductivity ranges from  $742.3$  to  $872.3 \text{ Scm}^{-1}$ , displaying an exceptionally high conductivity for a p-type conductor and a high-temperature metallic phase (Figure 2.12). Due to its superior conductivity than many other p-type transparent conduct-

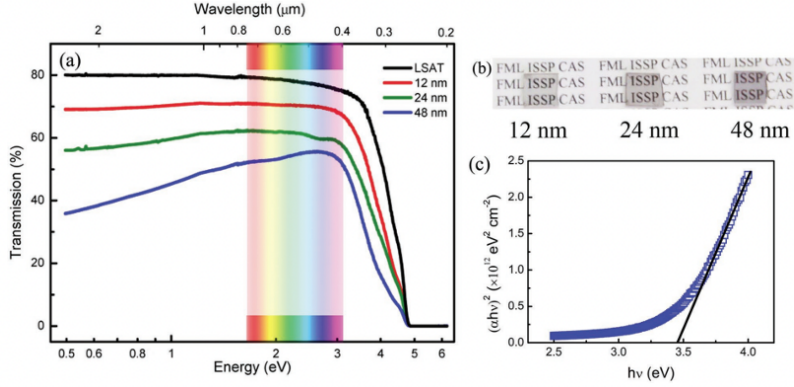


Figure 2.13: (a) Transmission spectrum of the LSVO thin films with varying thickness on LSAT substrates. (b) Photographs of 12, 24, and 48 nm LSVO thin films on LSAT substrates. (c) The plot of  $(\alpha h\nu)^2$  versus  $h\nu$  for the 48 nm LSVO thin film. Figures taken from reference [12].

ing oxides, a p-type LSVO would be a useful conductor in a variety of optoelectronic devices. However, such a p-type conduction has not been observed before, and this study was the main motivation to study the full LSVO solid solution in thin films.

$\text{La}_{2/3}\text{Sr}_{1/3}\text{VO}_3$  thin films also exhibited outstanding optical transparency in the visible range in addition to their high conductivity. The range of transmission values, from 53.9% to 70.1% (Figure 2.13), suggests that the films can let through a sizable amount of visible light.

In contrast to what was observed in the parent compounds, a slight change in the oxygen content can lead to significant variations in the solid solution properties, thereby drastically modifying the functionalities of these materials. L. Hu et al [12] studied the influence of oxygen vacancies on the electronic phase transition and transport properties of thin films  $\text{La}_{2/3}\text{Sr}_{1/3}\text{VO}_3$ . The presence of oxygen vacancies induces a metal-insulator transition through electronic imbalances and lattice distortions. The oxygen stoichiometry of  $\text{La}_{2/3}\text{Sr}_{1/3}\text{VO}_3$  was crucial, and the substrate's oxygen contribution was considered during thin film deposition. The effects of oxygen reduction on transport properties were observed in  $\text{La}_{2/3}\text{Sr}_{1/3}\text{VO}_{3-\delta}$  films and vary depending on the doping level and type of dopant used.

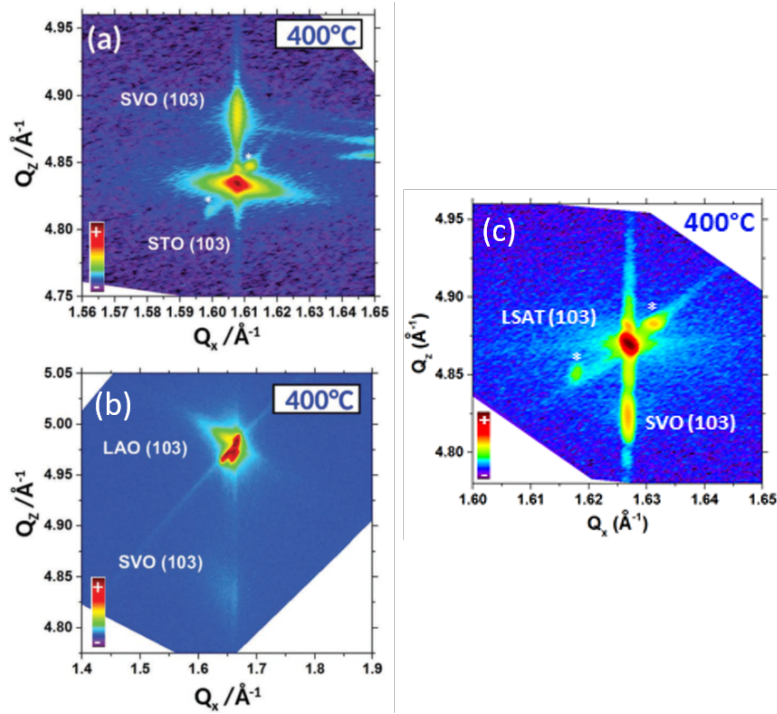


Figure 2.14: Reciprocal Space Maps of the (103) XRD reflection of a SVO film deposited on STO (a), LAO (b) and LSAT (c). The  $Q_x$  alignment of the substrate peak and the film peak indicate the coherently strained growth of the film on the substrate. Figures taken from references [13] and [14].

### 2.4.1 Earlier studies at the CRISMAT

$\text{SrVO}_3$  thin films are a very active research area at the CRISMAT since some years now, with the aim to understand the fundamental mechanisms in this material and develop an industrially viable alternative to Indium-Tin-Oxide (ITO). A number of studies on the growth and the functional properties of this material were carried out during the post-doc of Alexis Boileau and Martando Rath, leading to insights which are indirectly also used in this thesis. The films were grown in the same deposition chamber as the LSVO films being subject of this thesis, under comparable conditions. Some of the main results will be summarized here, and the link to the LSVO thin films developed in this thesis will be highlighted.

One of the main topics of the growth studies of SVO films was the strain state of the material on different substrates,  $\text{SrTiO}_3$ ,  $\text{LaAlO}_3$  and LSAT, all (001) oriented, and the influence on the resistivity of the films. We have shown by measurements of Reciprocal Space Maps (Figure 2.14) that the films grow in a coherently strained

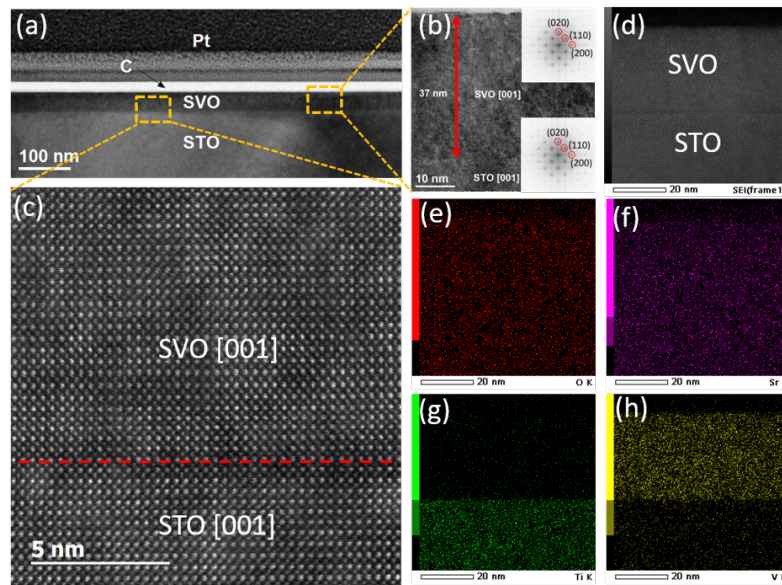


Figure 2.15: (a) Low magnification cross-sectional bright field TEM image of as grown SVO thin film on STO substrate, (b) High resolution TEM image of the sample and insets show fast Fourier Transform (FFT) patterns of SVO grown on the STO substrate, (c) High resolution STEM-HAADF micrograph showing perfect alignment of [001] SVO film on [001] STO. The dotted line indicates the interface position, (d) is a low magnification STEM-HAADF image showing the similar Z contrast between SVO and STO and (e-h) STEM-EDX mappings of the elements O, Sr, Ti and V respectively.

state on all these three substrates [13, 14], where the in-plane lattice parameter of the films corresponds to the lattice parameter of the substrate. Structural studies on  $\text{LaVO}_3$  films carried out on films deposited at the CRISMAT have also shown a coherently strained growth on STO [89]. Therefore, we can infer that the LSVO solid solution also grows coherently strained on these substrates.

A structural study using Transmission Electron Microscopy on cross sections has been carried out by Oleg Lebedev on  $\text{SrVO}_3$  thin films grown on STO (001) substrate. The structural coherence of the films at the substrate interface, as expected from the coherently strained growth, was observed as shown in Figure 2.15. The EDX maps show an homogeneous distribution of the different elements in the film, without interface interdiffusion.

The composition of the SVO thin films have been studied by Rutherford Backscattering (RBS) for SVO films grown on all three substrates by Ramon Escobar-Galindo at the Abengoa Research Laboratory in Sevilla, Spain. The fitting of the obtained

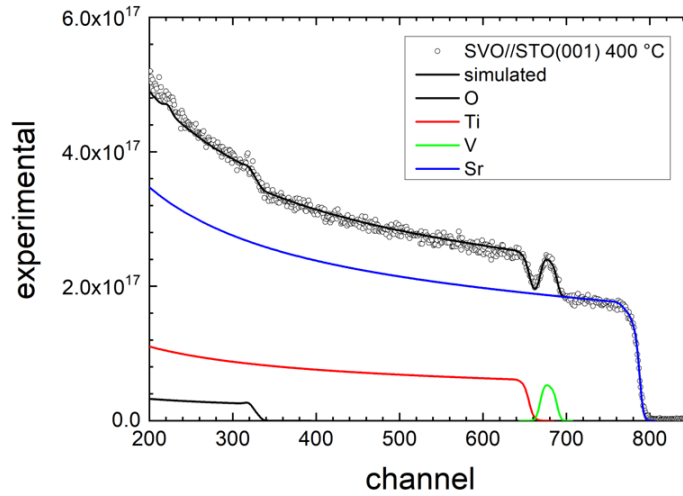


Figure 2.16: Typical RBS spectrum of a thin SVO film on STO (001).

spectra (as an example see Figure 2.16) allowed to determine the relative compositions of the cations and the anions. Concerning the Sr/V ratio, the results show that the same amount of Sr and V are present in the films, i.e. a good cationic stoichiometry has been reached. Concerning the oxygen content of the films, it was observed that the oxygen content depends on the used substrate. On LSAT and STO, the SVO films have a propensity to an oxygen understoichiometry, while for the films grown on LAO, the modeling shows a slight oxygen excess. Such an understoichiometry for the films grown on STO is consistent with the observed improvement of the film properties with a low temperature annealing in air [13].

## 2.5 Perovskite Chromites

lanthanum chromium Oxide, commonly referred to as  $\text{LaCrO}_3$ , is classified as a G-type antiferromagnetic insulator, exhibiting a Neel temperature ( $T_N$ ) of approximately 290 K. It exhibits a charge transfer gap measuring 3.3 eV and assumes an orthorhombic crystal structure (space group Pbnm) with lattice parameters  $a_o = 5.513 \text{ \AA}$ ,  $b_o = 5.476 \text{ \AA}$ ,  $c_o = 7.759 \text{ \AA}$ . [90, 91] and pseudo cubic parameter  $3.89 \text{ \AA}$ . Due to its intrinsic instability,  $\text{SrCrO}_3$  on the other hand is unstable due to the high energy  $\text{Cr}^{4+}$  oxidation state, with just one electron more than the much more stable  $\text{Cr}^{3+}$ . Therefore, in bulk, this compound is difficult to synthesize, although some studies exist showing that  $\text{SrCrO}_3$  assumes a cubic perovskite structure with a lattice parameter  $a = 3.81 \text{ \AA}$  and is a metallic conductor [92], with bond instabilities leading to a semiconducting phase [93, 94]. Thin film studies have shown these same instabilities, combined with a strong oxygen transport at quite low temperatures. [95]. For the following, the solid solution will be referred to as  $\text{La}_{1-x}\text{Sr}_x\text{CrO}_3$  in the literature, as strontium is considered to be the dopant. Note that in our study, the lanthanum is considered as dopant, and so the solid solution in the upcoming chapters would be considered as  $\text{La}_x\text{Sr}_{1-x}\text{CrO}_3$ . The electrical conductivity ( $\sigma$ ) and Seebeck coefficient ( $S$ ) of  $\text{La}_{1-x}\text{Sr}_x\text{CrO}_3$ , in its doped variant, can be modulated. The modulation is attained via partial aliovalent cationic substitution, denoted by the ratio  $x$ , on the A-site of the perovskite configuration. The process of substitution leads to the creation of impurity energy levels that are shallow in nature, and this, in turn, generates mobile hole carriers. [96]

LSCO thin films are of considerable importance because of to its broad range of applications in advanced devices. A few such applications comprise of on-chip thermal energy harvesters that transform dissipated heat into exploitable electrical energy, and coolers that use the Peltier effect to regulate heat in microdevices. Thin films offer advantages to optoelectronic devices by improving the performance of transparent diodes and electrodes. In addition, they assume a crucial function in photocatalysis, an operation used for the purpose of environmental restoration and energy transformation. Furthermore, it plays a crucial role in the emerging domain

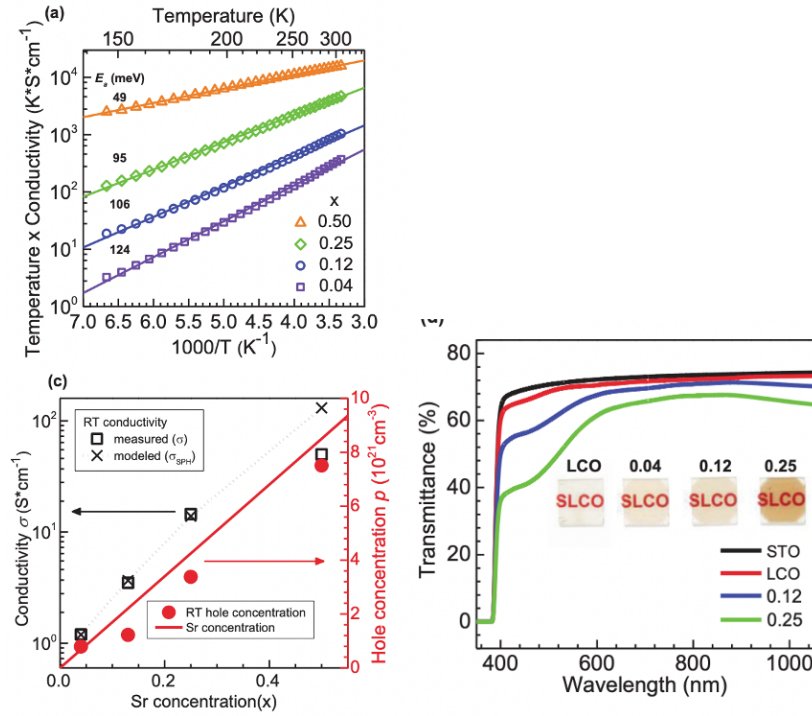


Figure 2.17: Electrical and optical properties of LSCO: (a) Temperature dependence of the conductivity, (b) Optical transmission and photographs of the LSCO films deposited on STO(001), (c) RT conductivity and hole concentration versus  $x$ . Taken from reference [15].

of spintronics, serving as the fundamental component of memory storage devices that exploit the electron spin state. [15,97,98] Zhang et al. focused on the transport properties of  $\text{La}_{1-x}\text{Sr}_x\text{CrO}_3$  thin films and the ability to be tuned depending on the substitution ratio  $x$ . [15,18] An in-depth analysis of the optical transmittance behavior of LSCO indicates a reduction in optical transparency caused by absorption phenomena in the vicinity of the 450 nm wavelength, resulting in a subtle brownish hue. In order to conduct a comprehensive comparative evaluation of LSCO's performance in relation to other p-type TCOs, the authors have intelligently calculated a figure of merit (FOM), which sheds light on the material's relative performances.

Divalent strontium ( $\text{Sr}^{2+}$ ) is partly substituted at the perovskite A site, which facilitates the entry of holes into the valence band and causes the material to change into a p-type transparent conductor. [99] Farrell et al. used a small polaron hopping model, appropriate for materials with very low mobilities, to further investigate the transport features. [100] This approach made it possible to separate the hole

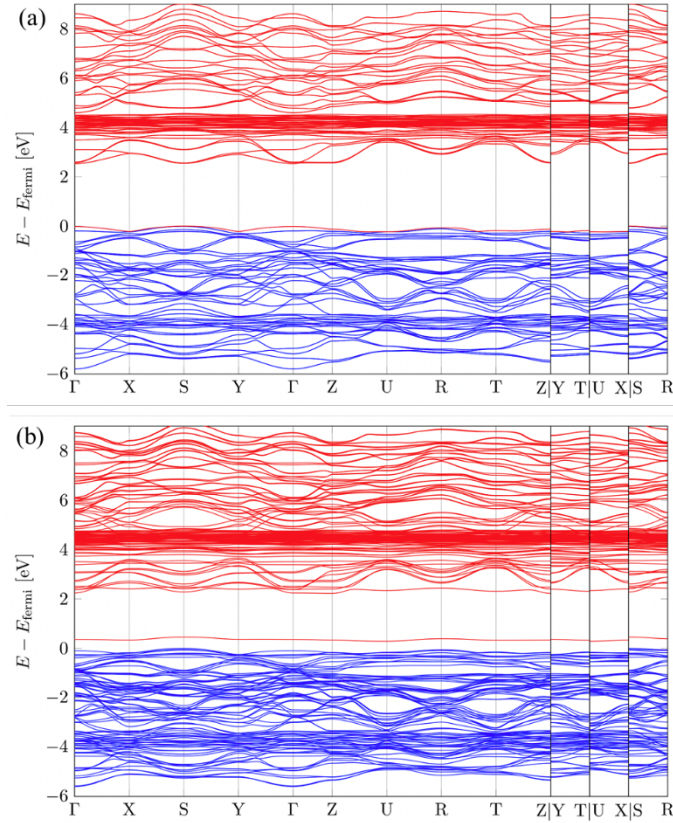


Figure 2.18: Band structure of (a) metallic and (b) polaronic  $\text{La}_{0.75}\text{Sr}_{0.25}\text{CrO}_3$ . Blue states are occupied at  $T = 0$  K. Taken from reference [16]

concentration ( $p$ ) from the Seebeck coefficient ( $S$ ), which gave useful information on the material's inherent behavior. [15] Manipulating strain, the electric conductivity, Seebeck coefficient, and thermoelectrics factor of the LSCO films can be tuned, enhancing the properties as demonstrated by Dong Han et al [101].

Comparative examination of the material's metallic and polaronic phases revealed observable differences in the lengths of the Cr-O bonds and band structures [16]. These results, shown in Figure 2.18, were obtained using ab-initio calculations and demonstrated an enhanced localization of O atoms around a single Cr atom in the polaronic state. Despite the material's naturally poor mobility, Sr substitution for La can significantly increase carrier concentration, leading to an increase in electrical conductivity. According to experimental evidence, modest polaron hopping accounts for transport phenomena for  $x = 0.65$ . [15]

Density functional theory (DFT) simulations have been combined with spectro-

scopic data, including X-ray photoelectron spectroscopy (XPS) and X-ray Absorption spectroscopy (XAS), to provide a thorough understanding of hole introduction as a result of Sr substitution for La [16]. These advanced methods have clarified the valence band chemical potential changes and the origin of split-off empty Cr 3d  $t_{2g}$  / O 2p hybridized orbitals (Figure 4.15). [99]

D. Han and al [17] studied the effect of strain on the electrical and thermoelectric properties of the Sr-doped  $\text{LaCrO}_3$  transparent thin films. Epitaxial strain effects on p-type transparent Sr-doped  $\text{LaCrO}_3$  thin films were systematically investigated by growing high-quality fully-strained  $\text{La}_{0.75}\text{Sr}_{0.25}\text{CrO}_3$  (LSCO) epitaxial thin films on three different (pseudo)cubic (001)-oriented perovskite-oxide substrates:  $\text{LaAlO}_3$ ,  $(\text{LaAlO}_3)_{0.3}(\text{Sr}_2\text{AlTaO}_6)_{0.7}$ , and  $\text{DyScO}_3$ . The lattice mismatch induced in-plane strain from -2.06% (compressive) to +1.75% (tensile), significantly influencing the structural, electronic, and thermoelectric properties. Electric conductivity could be finely controlled over two orders of magnitude (from  $0.5 \text{ S cm}^{-1}$  under tensile strain to  $35 \text{ S cm}^{-1}$  under compressive strain). Similarly, the Seebeck coefficient (S) exhibited tunability by almost two-fold (from  $127 \mu\text{V K}^{-1}$  under compressive strain to  $208 \mu\text{V K}^{-1}$  under tensile strain). These findings highlight the significant influence of epitaxial strain as a potent tool for manipulating the electrical and thermoelectric properties of LSCO, as presented in figure 2.19 and 2.20.

K. H. L. Zhang and al [18] systematically investigated the electronic property evolution in  $\text{La}_{1-x}\text{Sr}_x\text{CrO}_3$  ( $0 \leq x \leq 1$ ) epitaxial films grown via molecular beam epitaxy (MBE), employing a comprehensive set of techniques, including x-ray diffraction, x-ray photoemission spectroscopy, Rutherford backscattering spectrometry, x-ray absorption spectroscopy, electrical transport measurements, and ab initio modeling.  $\text{LaCrO}_3$ , initially an antiferromagnetic insulator, transforms into a metal upon Sr substitution. The incorporation of  $\text{Sr}^{2+}$  for  $\text{La}^{3+}$  introduces holes into the valence band, resulting in  $\text{Cr}^{4+}$  ( $3d^2$ ) local electron configurations. The core-level and valence-band features exhibit a systematic shift to lower binding energy with increasing  $x$ , indicating a downward movement of the Fermi level toward the valence band maximum. A transition from a p-type semiconductor to an insulator-to-metal transition is observed at  $x \geq 0.65$ , particularly when films are subject to in-plane

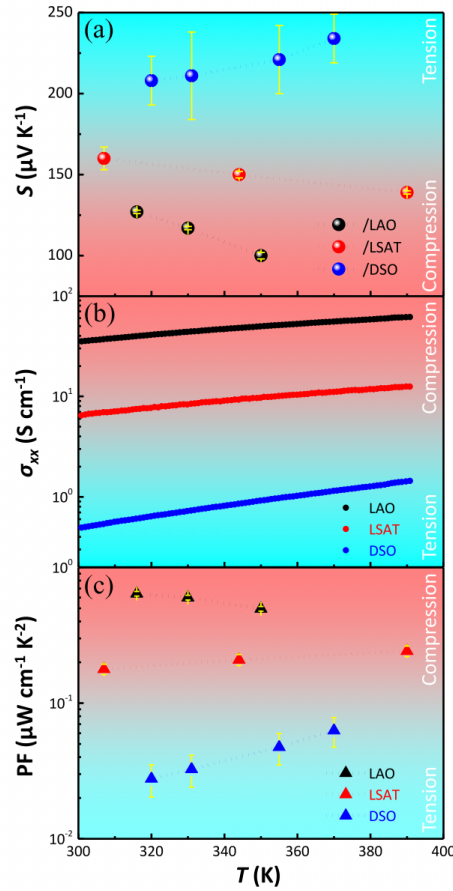


Figure 2.19: Temperature-dependent properties. (a) Seebeck coefficient ( $S$ ), (b) electrical conductivity and (c) thermoelectric power factor ( $\text{PF} = S^2$ ) for each film as a function of the temperature in the range of 300-400 K. Taken from reference [17]

compression through lattice-mismatched heteroepitaxy (figure 2.21).

Valence-band x-ray photoemission spectroscopy reveals a reduction in electronic state density at the Cr  $d_{t2g}$ -derived top of the valence band, while O K-edge x-ray absorption spectroscopy indicates the emergence of a new unoccupied state above the Fermi level as holes are doped into  $\text{LaCrO}_3$ . Density functional theory (DFT) with a Hubbard  $U$  correction of 3.0 eV (DFT +  $U$ ) captures the evolution of these bands with Sr concentration. In the semiconducting regime ( $x \leq 0.50$ ), resistivity data do not conform precisely to polaron hopping or band conduction models but align best with a hybrid model, and the activation energies extracted from these fits are well reproduced by DFT +  $U$ .

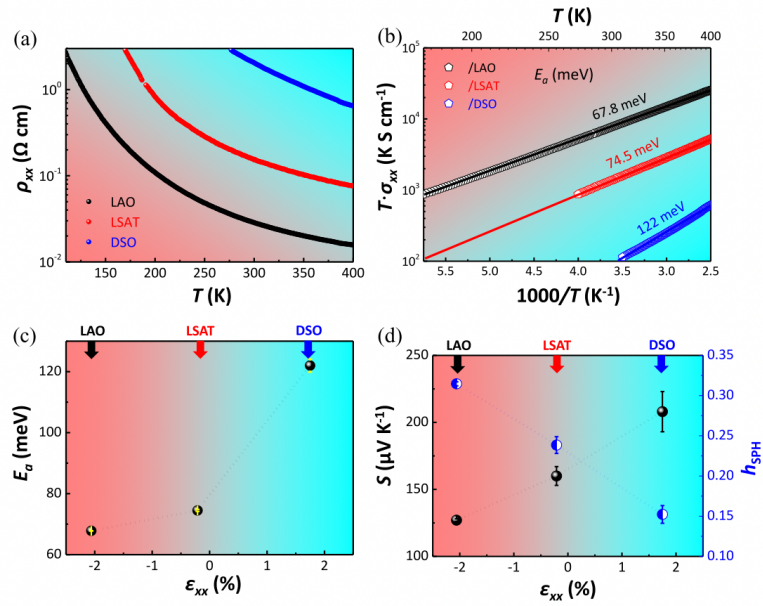


Figure 2.20: In-plane electronic and thermoelectric transport characterizations. (a) Temperature dependence of the resistivity ( $\rho_{xx}$ ) in the 100-400 K range. (b) Corresponding temperature dependence of the conductivity. (c) Activation energies ( $E_a$ ) for small polaron hopping extracted from (b), plotted as a function of in-plane strain. (d) Room temperature Seebeck coefficient ( $S$ ) and fraction of hopping sites occupied with holes ( $h\text{SPH}$ ) estimated from  $S$  and small polaron hopping model, plotted as a function of in-plane strain. Taken from reference [17]

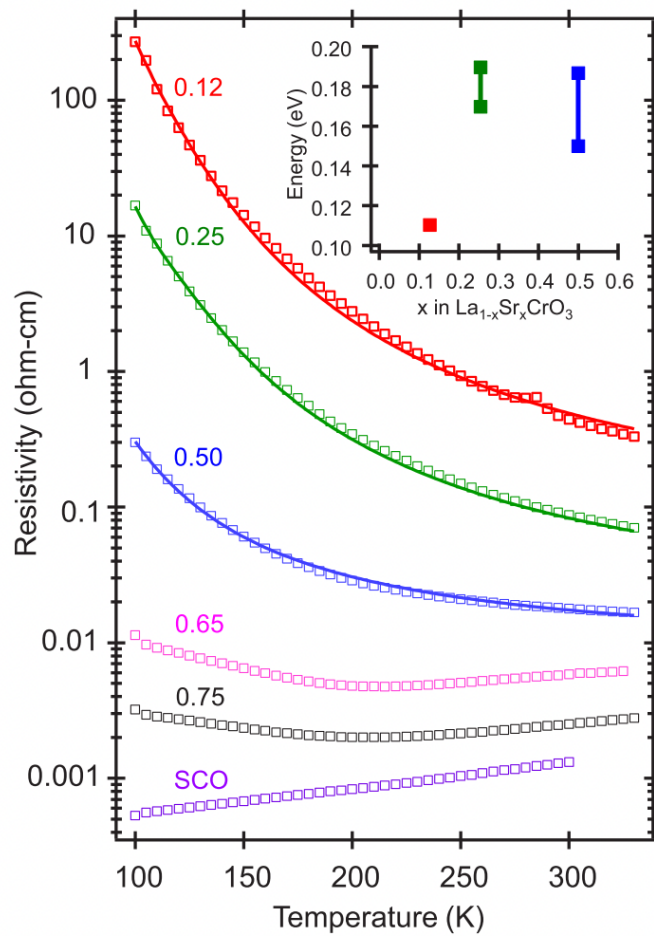


Figure 2.21: Resistivity for the  $\text{La}_{1-x}\text{Sr}_x\text{CrO}_3$  film series (open squares) along with fits for  $x = 0.12, 0.25,$  and  $0.50$  (solid curves). Taken from reference [18]



## CHAPTER 3

---

### Experimental Methods

---

The objective of this section is to present a comprehensive summary of the methodologies used in our study for the growth of thin films, as well as the subsequent analyses conducted to assess their properties. The primary objective is to provide a comprehensive description of the used methodologies and concepts, along with the essential experimental conditions and parameters that played an essential part in achieving the intended outcomes.

### 3.1 Thin film synthesis

A variety of techniques have been developed for the growth of thin films, each possessing unique advantages and drawbacks. This section will present shortly the commonly used techniques of thin film growth, namely physical vapor deposition (PVD), chemical vapor deposition (CVD) and atomic layer deposition (ALD). Pulsed laser deposition (PLD) will be described in detail, and the deposition approach for the films fabricated during this thesis will be presented.

Chemical Vapor Deposition (CVD) entails the chemical reaction of precursor gases or liquids, leading to the formation of a solid material on the substrate surface. These growth techniques present a remarkable degree of homogeneity in the film and quick deposition rates, making them a fitting choice for industrial-scale applications of considerable importance. The deposition of a large number of perovskite oxide thin films has been developed with this technique [102, 103], allowing for high quality thin films, mostly polycrystalline. Perovskite Vanadates have not been largely deposited by CVD techniques, up to our knowledge, but as an interesting material for solid oxide fuel cells (SOFC), the growth of  $\text{LaCrO}_3$  has been demonstrated [104]. However, CVD typically needs elevated temperatures, and the precursors used may be costly, unsafe, or challenging to manage. In addition, the concern of possible contamination arising from leftover precursors calls for thorough supervision of the manufacturing process.

Atomic Layer Deposition (ALD) is a special technique of the CVD family. This process enables precise control over the thickness of the deposited film at an atomic level, as the different precursors are injected and purged sequentially in the growth chamber. Moreover, it exhibits exceptional conformal characteristics, making it a suitable option for the coating of intricate geometries. Notwithstanding the advantages, ALD is hampered by slow deposition rates and frequently necessitates costly and possibly unsafe precursors. Also, the limited deposition temperatures do rarely allow the deposition of crystalline films, and impose an annealing step. As ternary oxides, perovskite oxides are an especially challenging family of materials for ALD. The deposition of  $\text{SrTiO}_3$  is the most investigated one, but due to the industrial

importance of the ALD techniques, a number of perovskite oxides have been investigated [105]. The deposition of  $\text{SrVO}_3$  has been attempted, but the necessary post-annealing step to crystallize the film has led to oxidation problems [106].

A widely used family for the deposition of oxide thin films are the Physical Vapor Deposition (PVD) techniques. This family encompasses various techniques, including thermal and electron beam evaporation, as well as RF, DC, and magnetron sputtering, and also Pulsed Laser Deposition (PLD). One of the primary advantages of physical vapor deposition (PVD) is its versatility and ease of use, as it can effectively apply to a diverse array of materials. PVD techniques frequently encounter challenges such as inadequate deposition rates and issues associated to film homogeneity, particularly on complex geometries. Additionally, these processes typically necessitate the use of high vacuum environments. However, for the deposition of monocrystalline, high quality perovskite oxide thin films, these techniques stay the most important ones.

Molecular Beam Epitaxy (MBE) is an outstanding PVD technique concerning high quality thin films. This process involves the utilization of ultra-high vacuum conditions to evaporate source materials, which subsequently condense onto a substrate, resulting in the formation of thin films. The salient feature is its exceptional level of purity, which is achieved through the implementation of a high vacuum setting that restricts the exposure of the deposited atoms to any extraneous substances that may cause contamination. The MBE technique facilitates the growth of films in an atomic layer-by-layer manner, thereby providing precise regulation of film thickness and composition. The utilization of MBE is highly advantageous in the fabrication of complex configurations such as quantum wells and superlattices. Although MBE offers certain advantages, the process is characterized by a slow deposition rate and necessitates the use of sophisticated and costly equipment, thereby diminishing its cost-efficiency. Almost any standard perovskite oxide has been deposited by MBE. The first studies on  $\text{SrVO}_3$  as a TCO have been prepared using hybrid MBE [1], where a metal-organic precursor was used as the vanadium source. One of the very few successful attempts to deposit  $\text{SrCrO}_3$  thin films has been carried out using MBE [107], and the solid solution LSCO was also investigated

by MBE. [15,18]

### 3.1.1 Pulsed Laser Deposition (PLD)

Pulsed Laser Deposition (PLD) is one of the most used deposition technique for perovskite oxide, principally due to the good trade off between the growth optimization time and the quality of the obtained film. In this technique, we use a high-intensity laser to ablate a target of the to be deposited material, and therefore grow a thin film of this material on a substrate. PLD offers a precise growth of film composition, exhibiting a compatibility with multicomponent or layered structures, and diverse range of materials. Despite its advantages, PLD may encounter challenges related to film uniformity, and its deposition rate is generally inferior to that of alternative techniques. Furthermore, the substantial amount of energy utilized during the procedure may occasionally lead to the incorporation of droplets or particles into the coating. Notwithstanding the aforementioned limitations of PLD, it has been selected as the preferred technique for this study. The reason of using PLD lies in its capability to generate thin films with meticulous regulation of the stoichiometry, a crucial aspect in the context of the materials under investigation.

The properties of the deposited film can be controlled by several process parameters, such as laser fluence, substrate temperature, background gas pressure, and the target-substrate distance. Epitaxial growth is frequently facilitated by elevated substrate temperatures, whereas the oxygen stoichiometry in deposited perovskite oxide films can be regulated by manipulating the oxygen partial pressure.

#### Principle of Pulsed Laser Deposition

A pulsed laser beam is focused in the surface of a target, generally a solid pellet composed of the cationic composition of the desired perovskite oxide. This interaction results in the generation of a plasma plume, containing a variety of material constituents in different states, including atoms, ions, and clusters. The expansion of the plasma plume occurs in the direction of a substrate, which results in the combination and precipitation of elements as a thin layer, as illustrated in Figure 3.1. The selection of the laser is an important factor. Perovskite oxide materials

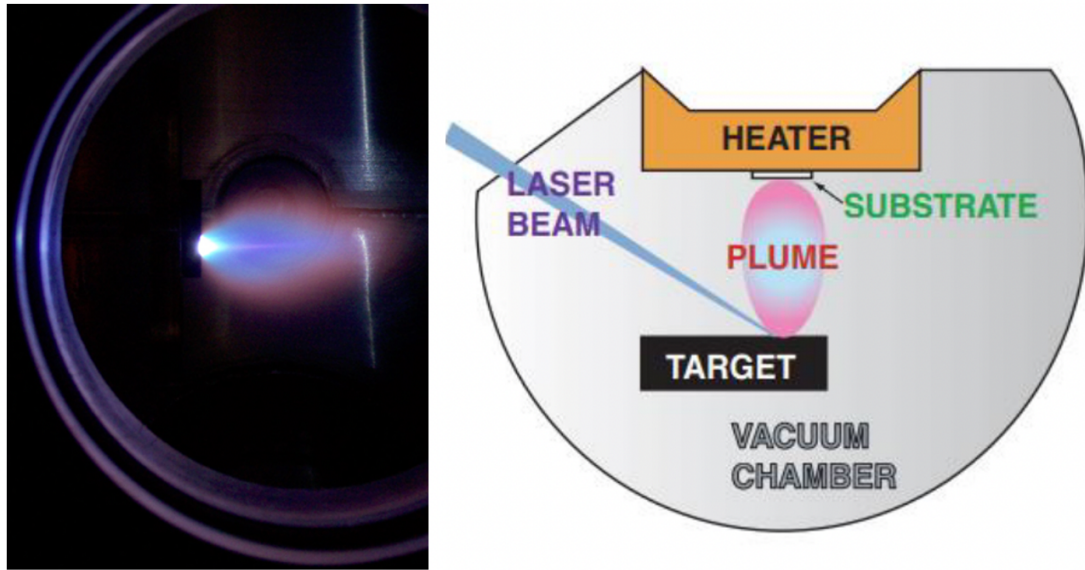


Figure 3.1: Image of the plume generated by the impact of the laser on the target (left side) and schematics of Pulsed Laser Deposition (right side).

often employ excimer lasers, such as KrF or ArF lasers, or solid-state lasers, like Nd:YAG, owing to their notable energy output, which is necessary for the ablation of the target material. The present study employed a KrF laser.

### 3.1.2 Growth parameters

**Laser parameters** The standard laser parameters for the deposition are a wavelength of 248 nm, an outgoing energy of 200 mJ and a repetition rate of 3 Hz, if not mentioned otherwise. Prior to deposition, the laser has been warmed up during 10 min in order to reach stable laser emission. After the warming period, the energy of the laser has been calibrated and adjusted to the desired value.

**Configuration of the targets** A converging lens directs the high-energy laser beam onto the target. The target is fixed on a rotating carousel that can hold up to eight distinct targets, enabling the deposition of many materials in a single run while maintaining the sample under vacuum. In the case of this thesis, targets of the two parent compounds of each solid solution have been used and rotated under the laser beam sequentially. For LSVO, a  $\text{LaVO}_4$  and a  $\text{Sr}_2\text{V}_2\text{O}_7$  target have

been used. These targets have the correct cationic stoichiometry, but the oxygen content is adjusted by the growth atmosphere during the deposition. For LSCO, a  $\text{SrCrO}_x$  target has been used. Here, the oxygen content of the target has not been measured, but the cationic stoichiometry is 1:1. For the other parent compound, a target of  $\text{LaCrO}_3$  was used. Before the deposition, each target is preablated in order to ensure a stable surface composition of the target, with the sample protected from deposition by a shutter. The target and the substrate are kept at a constant distance of 5 cm, which was shown to be optimal on the impact of the energy and density of the species that arrive to the substrate. In the particular PLD machine used for this thesis, the laser was scanned on the surface of the target on a area of about 10 x 10 mm. Therefore, the plume is not fixed in space, but moves. The substrate is placed in the resulting homogeneity area on the substrate holder in order to ensure the deposition of homogeneous films. Compared to other PLD machines with a fixed plume position, the deposition rates with such a scanning configuration are up to a factor of 5 smaller, allowing to deposit the ultra-thin films needed for the constitution of the solid solution and a high variability of the doping rate.

**Substrate preparation** An essential step in promoting the formation of high-quality films is the substrate surface preparation. As part of the process, substrates are carefully cleaned using acetone and ethanol in ultrasonic bath to get rid of any surface impurities. After that, using silver paste to place the substrate onto a heating support, a thermocouple is linked to the sample holder to provide temperature control.

**Conditions of vacuum and atmosphere** The PLD process is carried out under controlled atmospheric conditions. An initial  $10^{-2}$  mbar rough vacuum is attained using a primary pump, and an additional  $10^{-7}$  mbar high vacuum is attained using a turbo-molecular pump. oxygen may be injected into the chamber using mass flow controllers after the required vacuum level has been reached, and the deposition pressure is controlled by a valve in front of the turbo pump. As for the Vanadate solid solution, over-oxidized targets  $\text{Sr}_2 \text{V}_2\text{O}_7$  are used, the deposition was carried out in vacuum. Tests with even small amounts of oxygen in the deposition atmosphere did

not lead to conducting samples. For the Chromite solid solution on the other hand, using oxygen in the deposition atmosphere, was beneficial and has been optimized (see chapter 5).

**Temperature Regulation** Prior to the deposition process, the substrate temperature is carefully regulated. The temperature increases until it reaches 300 °C at a rate of 20 °C/min, before a 3-minute pause. After that, the temperature is raised by 10 °C/min rate until the appropriate deposition temperature is obtained. The management of substrate temperature is essential because it affects the kinetic energy of the depositing species, adatom mobility on the substrate surface, and ultimately the growth mode and crystallinity of the films. The deposition temperature has been one of the main parameter of the deposition optimization, and was chosen in the range between 500 °C and 800 °C in order to allow for the in-situ crystallisation of the film. After the deposition, the sample was cooled down at a rate of 10 °C/min under the deposition atmosphere.

### 3.1.3 Solid solution compositional calibration

A suitable calibration prior to the deposition of solid solution thin films is required for the precise estimation of the parent compound deposition rates, and therefore the composition of the deposited film. The approach of generating solid solutions in-situ, in contrast to using solid solution targets, affords a significant degree of control over the deposition of each parent compound, and a variety of solid solution compositions can be produced by choosing the number of laser pulses applied to the respective targets. Sub-unit cell layers of each parent material are deposited, with the proportion corresponding to the intended composition within the solid solution. By continuously executing this procedure, a film thickness of multiple tens of nanometers is achieved.

Two distinct calibration methods have been tested to ensure the accuracy of the growth rate and, as a result, the composition of the solid solution. The first one is based on the thickness calibration of individual parent compound thin films, but as the deposition rate may differ for extremely thin films, we have also carried out a

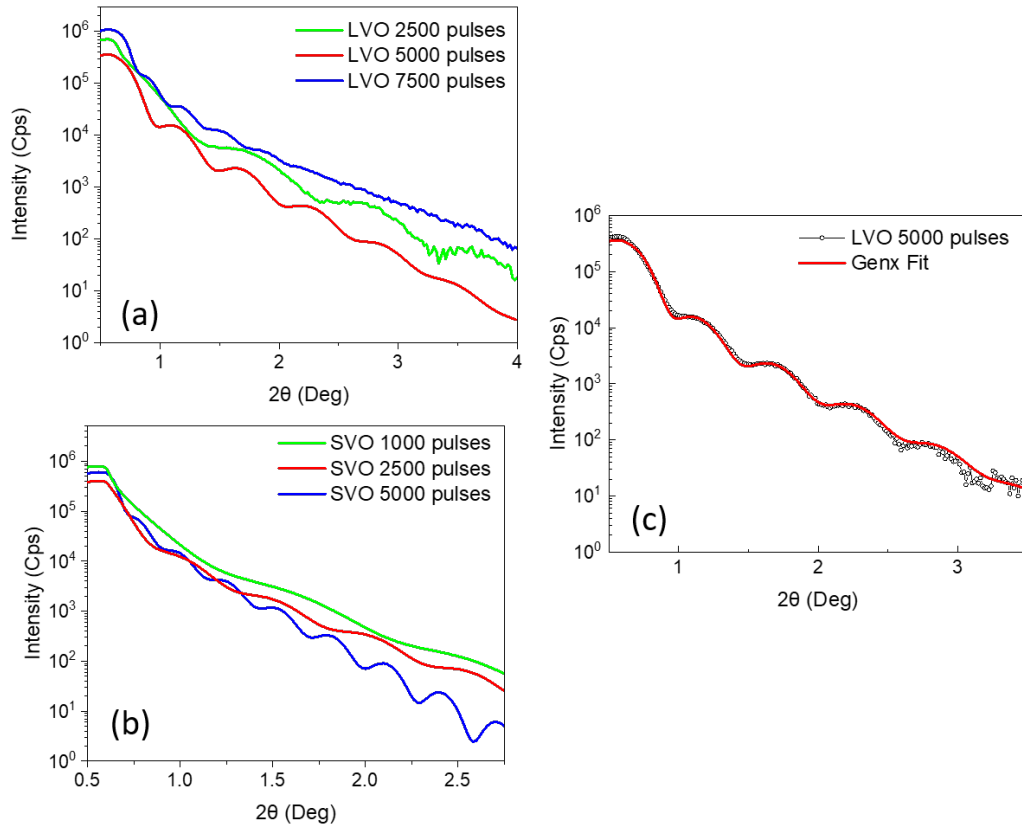


Figure 3.2: XRR of  $\text{LaVO}_3$  on STO (a) and  $\text{SrVO}_3$  on STO (b) single film samples with different numbers of laser pulses, (c) XRR simulation of one of the  $\text{LaVO}_3$  samples with Genx.

calibration process using a superlattice approach, so as to mimic as well as possible the final deposition of the solid solutions.

### Individual Target Deposition Calibration

This calibration procedure entails the growth of six distinctive samples, comprising three single film samples for each parent compound. Samples are grown for each target using varying numbers of laser pulses. Here, we have chosen particularly 2500, 5000, and 7500 pulses, in order to obtain a thickness which is easy to be measured by X-Ray Reflectivity (XRR, see section 3.2.2). A plot is generated by relating the film thickness with the used number of pulses. The slope of this curve yields the deposition rate for every parent compound. This provides a reliable and accurate estimation of the deposition rate, which is crucial in getting the intended

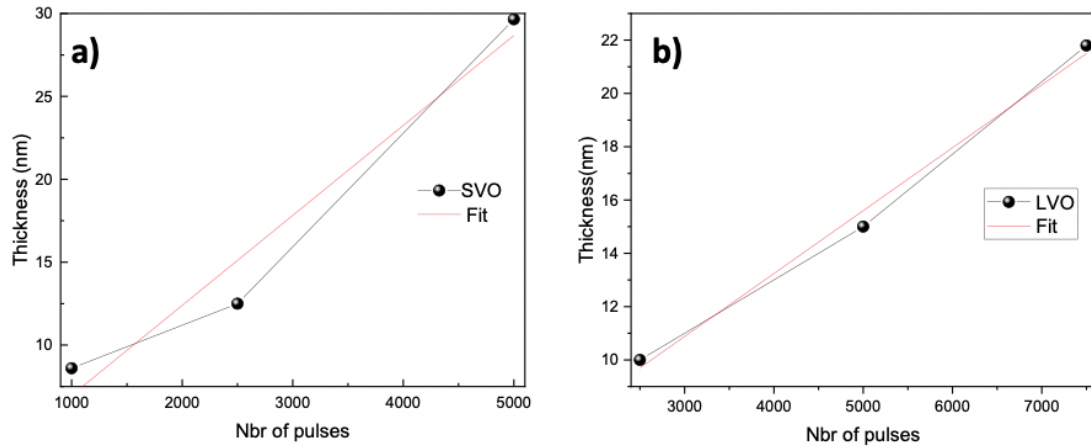


Figure 3.3: The correlation between the thickness of the samples and the laser pulses for (a) SVO and (b) LVO. The red lines are linear fits of the data.

compositions.

In order to provide an actual illustration of this calibration process, we present here an example for the LSVO solid solution. The purpose of this experiment was to calibrate and determine the thickness of three  $\text{LaVO}_3$  samples and three  $\text{SrVO}_3$  samples, as illustrated in Figure 3.2 (a),(b). The estimation of their thickness was accomplished using the  $\sin^2 \theta_m$  estimation method, which will be further explained in the subsequent XRR section. Furthermore, the Genx software was used to assess the precision of this thickness estimation. Figure 3.2 (c) depicts the fit analysis on an  $\text{LaVO}_3$  sample using this software, thereby providing additional validation. The Genx fit is giving a thickness value of 14.1 nm and a film roughness of 0.7 nm in this case.

The Figure 3.3 (a),(b) illustrates a linear regression that demonstrates the correlation between the thickness and the number of laser pulses for both SVO and LVO samples. The present analysis yielded highly precise deposition rates of 0.00543(10) nm/pulse for SVO and 0.00236(2) nm/pulse for LVO. The accurate quantification of the deposition rate per pulse allows the prospect for precise adjustment of laser pulses on the target, thereby enabling effective tuning over the composition. Significantly, it is imperative to point out that the deposition of one unit cell calls for 71 pulses for SVO and 169 pulses for LVO in this specific case.

### Superlattice Deposition Calibration

An alternative method for a solid solution calibration is based on the deposition of superlattices. The use of a superlattice-based approach has been found to bring notable advantages in comparison to the individual target calibration, especially in the case that one of the parent compounds is not stable as a single film, as for example  $\text{SrCrO}_3$ . The superlattice calibration involves the growth of three distinct laminate samples, all of which are subjected to identical deposition parameters, though with varying quantities of laser pulses on the two parent compound (PC) targets. The pulse numbers ( $n_{PC1}/n_{PC2}$ ) used in the calibration were  $(1000/1000) \times \#_{SL1}$ ,  $(1000/100) \times \#_{SL2}$ , and  $(100/1000) \times \#_{SL3}$ , where  $\#_{SL1}$ ,  $\#_{SL2}$ , and  $\#_{SL3}$  denote the respective numbers of repetitions required to attain comparable overall superlattice thicknesses. The thickness of each superlattice sample is determined experimentally and the deposition rate of each parent compound is calculated accordingly. The aforementioned procedure entails the measurement of the total superlattice thickness, followed by the division by the number of repetitions  $\#_{SL}$ , thereby enabling to derive the thickness of each PC1/PC2 bilayer. The mean bilayer thickness  $\Lambda_{SL}$  is then used to solve graphically the linear equation  $\Lambda_{SL} = \tau_{PC1} \times n_{PC1} + \tau_{PC2} \times n_{PC2}$ .  $\Lambda_{SL}$ ,  $n_{PC1}$  and  $n_{PC2}$  being known, a line can be drawn for each SL in a plot correlating the two deposition rates  $\tau_{PC1}$  and  $\tau_{PC2}$ . The intersection of the three lines denotes the common solution, i.e. the actual values of the deposition rates.

In order to provide a more comprehensive understanding of the calibration process, we present here an example of the calibration carried out prior to a set of LSCO solid solution. Figure 3.4 (a) displays the XRR measurements of the three calibration superlattices that were examined. Based on the determination of the overall thickness and using the GenX software, a series of equations were derived to establish the relationship between the bilayer thickness and the rate of deposition:

$$\begin{aligned}
 4.43nm &= \tau_{SCO} \times 300 + \tau_{LCO} \times 1000 \\
 5.28nm &= \tau_{SCO} \times 1000 + \tau_{LCO} \times 300 \\
 6.22nm &= \tau_{SCO} \times 1000 + \tau_{LCO} \times 1000
 \end{aligned} \tag{3.1}$$

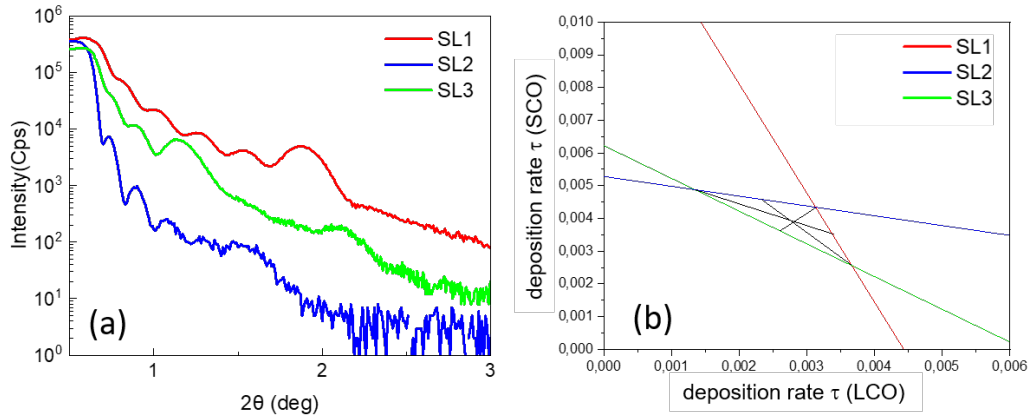


Figure 3.4: (a) XRR measurements of the different calibration superlattices for  $\text{SrCrO}_3/\text{LaCrO}_3$ , (b) Graphical solution of the three superlattice equations.

Figure 3.4 (b) illustrates the graphical representation of the solution to these three equations. The lines do not cross in a single point, due to the measurement uncertainties. In this case, the middle of the obtained triangle is used, displaying deposition rates of 0.003899 nm/pulse for SCO and 0.00279 nm/pulse for LCO.

This methodology offers a notable benefit of enhanced precision over the count of laser pulses for every parent compound, with a reduced number of samples and lower variability in comparison to the individual target calibration. Therefore, we have chosen this calibration method for the studies carried out in this thesis. The calibration has been carried out before each deposition campaign in order to take into account changes in the machine or the targets. The reproducibility was typically in the range of 10 % for the deposition rates. From the calibrated growth rates, the respective number of pulses on the parent compound targets has been calculated by depositing the unit cell fraction corresponding to the desired La doping  $x$ . The chemical composition of the solid solution samples has been controlled by the adapted techniques in some cases, showing that the developed calibration procedure is reliable.

### 3.1.4 Surface cleaning of Vanadate films

Perovskite Vanadate thin films, and especially those containing an unstable V oxidation state as  $\text{V}^{4+}$  as  $\text{SrVO}_3$  were shown to be subject to surface ageing [108]. The

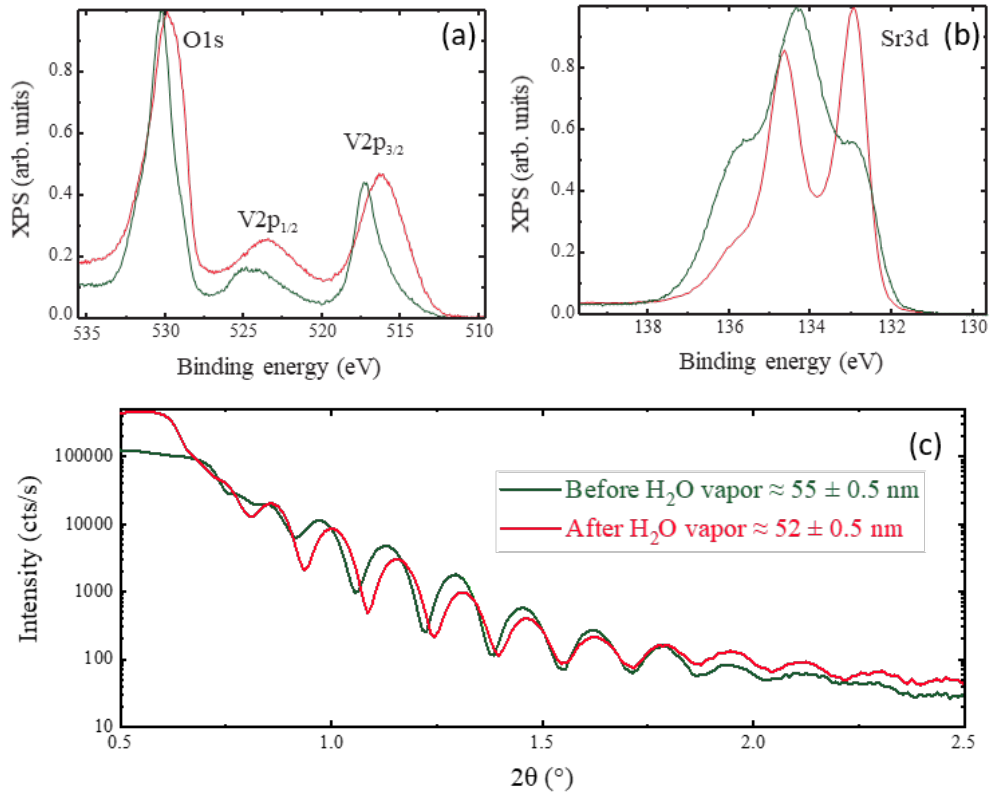


Figure 3.5: O 1s and V 2p<sub>3/2</sub> (a), and Sr 3d (b) XPS spectra recorded before (dark green) and after liquid water cleaning procedure of 1 min (red). (c) XRR spectra before and after the water cleaning. Figures taken from reference [19]

transformation to a higher oxide allowing for the V<sup>5+</sup> state, as Sr<sub>3</sub>V<sub>2</sub>O<sub>8</sub> or Sr<sub>2</sub>V<sub>2</sub>O<sub>7</sub> was shown to take place under oxygen annealing at high temperature [109], with an insulating character [110]). We have also observed the deterioration of the surface resistivity of single SrVO<sub>3</sub> films after some months. Artificial ageing experiments under ambient atmosphere have shown a decrease of the resistivity of monocrystalline and polycrystalline films during annealings at temperatures from 150 °C on, and a full destruction of the conducting perovskite phase at a temperature of 250 °C [111]. Therefore, a slow deterioration at room temperature of the surface due to reaction with the ambient atmosphere on the time scale of some months becomes possible.

This aspect is especially important for this thesis, as surface-sensitive spectroscopic techniques are employed (see chapter 3.3) in order to determine the chemical composition of the films, and the V oxidation state. Bourlier et al [108] have pro-

---

posed a water treatment of the SrVO<sub>3</sub> films, which allows to dissolve the higher oxides in a rapid way and restore the surface of the originally deposited sample. We have adapted this treatment to the LSVO films, by emerging and stirring them in distilled water for one minute. In Figure 3.5 (a) and (b), the effect of this cleaning can be observed by XPS analysis. Without entering into the details of the line shapes, both the V and the Sr signal change the shape after the cleaning, in the same way as observed by Bourlier et al (cite Bourlier), restoring the V<sup>4+</sup> state of the SVO film. The detailed analysis of this data was reported in [19]. In order to estimate the thickness of the chemically modified surface layer, the film thickness was measured before and after the water treatment by XRR, showing a reduction of the film thickness of about 3 nm. With such a small thickness, the surface modification does not influence macroscopic measurements as X-ray diffraction, optical or electrical characterisation, but will influence the spectroscopic measurements. Thus, in these cases, we have applied the water treatment systematically to the sample after a first reference spectra on the aged surface. The spectra presented in this thesis were made on water cleaned surfaces.

## 3.2 Structural characterization

The structural characterization of the deposited thin films allows to determine the structural phase and the orientation of the epitaxial films, but also to determine important film characteristics, as for example their lattice parameter and the film thickness. This characterization was carried out in this thesis using two techniques of X-ray diffraction, where the high angle measurements in the Bragg-Brentano configuration (section 3.2.1) allow for the analysis of the structural parameters of the thin films, while low angle measurements (section 3.2.2) are used to determine the thickness of the films.

### 3.2.1 X-Ray Diffraction

A crystalline arrangement of atoms is made up of a precise three-dimensional periodic lattice with a fundamental elementary cell defined by three lattice vectors that describes completely the arrangement of atoms. Three lattice parameters,  $a$ ,  $b$ , and  $c$ , as well as three angles  $\alpha$ ,  $\beta$ , and  $\gamma$ , define these lattice vectors, which result in 14 Bravais lattices with different symmetries. The elementary cell described the minimal structural unit being reproduced periodically in the lattice, by distributing the atoms in a pattern at each node of the lattice. Every plane that runs through three nodes is referred to as a lattice plane. An infinity of identical planes, each identified by the three Miller indices  $(hkl)$  and characterized by an interplane distance  $d_{hkl}$ , form a family of lattice planes when the periodicity of the lattice is taken into consideration.

In order to characterize this periodic unit cell, the interaction of X-rays with the constituting atoms is used. The technique entails exposing a crystalline lattice to X-rays with a fixed wavelength  $\lambda$  under a varying incidence angle  $\theta$ . When  $\lambda$  is an integer multiple  $n$  of the inter-lattice spacing  $d_{hkl}$ , a fraction of the incident X-ray beam is diffracted when it interacts with the crystalline lattice, leading to positive interferences of the diffracted beam (Figure 3.6). Bragg's law allows to capture quantitatively this situation:

$$n\lambda = 2d_{hkl} \sin \theta \quad (3.2)$$

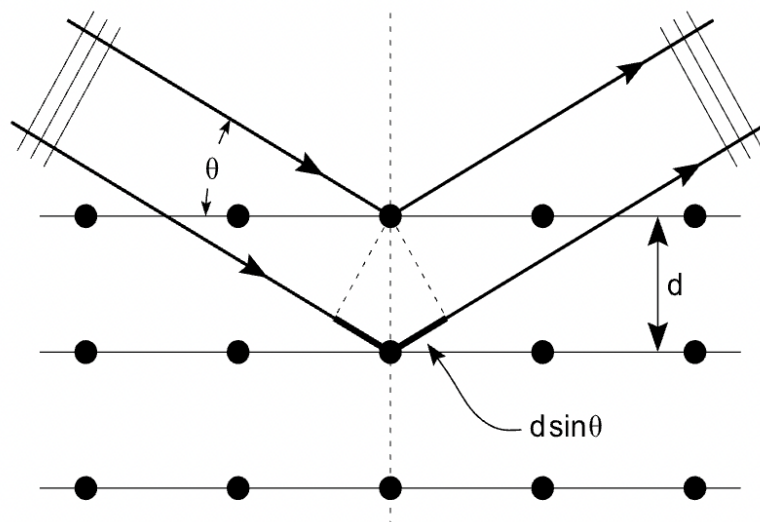


Figure 3.6: Schematic representation of the X-ray measurement principle, with the incident beam on the left side with an incident angle  $\theta$ . The crystalline lattice is characterized by the interplane distance  $d$ . [20]

This techniques can be used to determine the lattice parameter outside the plane of the acquired phase as well as the interplanar distance  $d_{hkl}$  separating two planes belonging to the same family which make it a potent tool for describing the crystal structure of materials.

The measurement is carried out in a X-ray diffractometer with the Bragg-Brentano configuration. In this measurement setup (Figure 3.7), the X-ray tube's location and detector's angular position are both changed at the same time. The diffraction vector, defined by the incident and the outgoing beam, stays normal to the sample's surface while the incidence angle  $\theta$  and detection angle  $2\theta$  are increased, but its length changes. As for positive interference, the diffraction vector has to coincide with the lattice plane vector, only the crystallographic planes parallel to the sample surface are accessible in this measurement mode. A large angle  $\theta - 2\theta$  scan gives access to both the substrate's and the deposited film's diffraction peaks. As a result of the interference of the diffracted beams at the film/substrate interface and the surface of the deposited film, oscillations of finite thickness may be also observed. The number of deposited atomic planes and subsequently the thickness of the film may be determined by mathematically modeling these oscillations, as shown by the

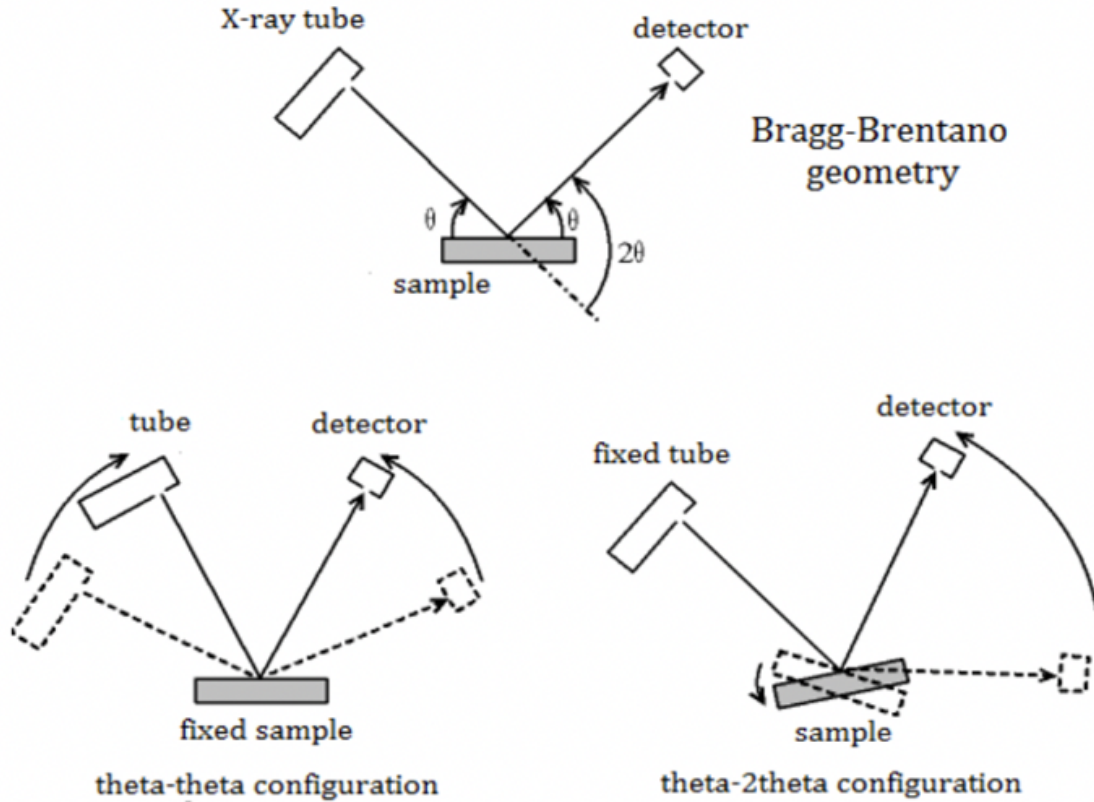


Figure 3.7: Schematic representation of the X-ray measurement configurations. [21]

expression:

$$I = \left( \frac{\sin(2\pi N c \sin(\frac{\theta}{\lambda}))}{\sin(2\pi c \sin(\frac{\theta}{\lambda}))} \right)^2 \quad (3.3)$$

where  $c$  is the out-of-plane film lattice parameter and  $N$  is the total number of scatterers, i.e. the number of atomic layers deposited during growth. As these oscillations are related to the periodic arrangement of a reduced number of scatterers, their appearance in the  $\theta - 2\theta$  measurements is a sign of a good periodicity, and therefore a high crystalline quality of the deposited film.

In this thesis, a Bruker D8 Discover diffractometer has been used with a Cu X-ray source. Before interacting with the sample, the beam crosses a monochromator selecting the Cu  $K_{\alpha 1}$  with a wavelength  $\lambda = 1.5406 \text{ \AA}$  and a slit of typically 0.2 mm to shape the beam. The diffracted beam is again selected by a number of slits with the same opening of 0.2 mm, before being detected by a point detector. Before the

$\theta - 2\theta$  measurement, the sample is aligned with the diffractometer. The height  $z$  of the sample is optimized so that it cuts half of the direct incident beam, and the incident angle  $\theta$  is adjusted using a substrate diffraction peak in order to compensate for misalignments of the sample with the beam. The typical scan parameters of the  $\theta - 2\theta$  measurements (if not stated otherwise) are a step of  $0.1^\circ$  and a time per step of about 1s.

### 3.2.2 X-ray reflectivity

In addition to diffraction, X-rays may also reflect from a sample's internal and external surfaces. Information about the thickness, roughness, and density of thin films can be deduced from this reflecting behavior. When the incident X-ray beam is small enough, the beam is reflected from the surface of the sample. When increasing the incident angle above the critical angle  $\theta_c$ , the beam enters the sample, and is reflected at the interfaces between areas with different refractive index  $n$ , as predicted by Snell's law. This refractive index is related to the electron density, so that the intensity of the reflected beam depends on the difference of the total electron density of the different materials, i.e. the film and the substrate. When entering the sample, the same mechanisms as in a Fabry-Pérot interferometer applies. When the path difference  $\Delta l$  between the reflected beam from the surface and the reflected beam from an internal interface (such as the substrate/film interface or the interfaces between different layers), is an integral multiple of the X-ray wavelength  $\lambda$ , the X-ray beam's constructive interference results in intensity fringes in XRR measurements. The thickness of the film  $d$  affects  $\Delta l$ , which controls the periodicity of the fringes.

$$\Delta l = 2d\sqrt{n^2 - \cos^2 \theta} \quad (3.4)$$

The relationship between the film thickness  $d$  and the order number of the fringes  $N$  can be calculated by rearranging this equation accounting for the requirement for constructive interference, as following:

$$\sin^2 \theta_m = \frac{\lambda^2}{4d^2} N^2 + 2\delta \quad (3.5)$$

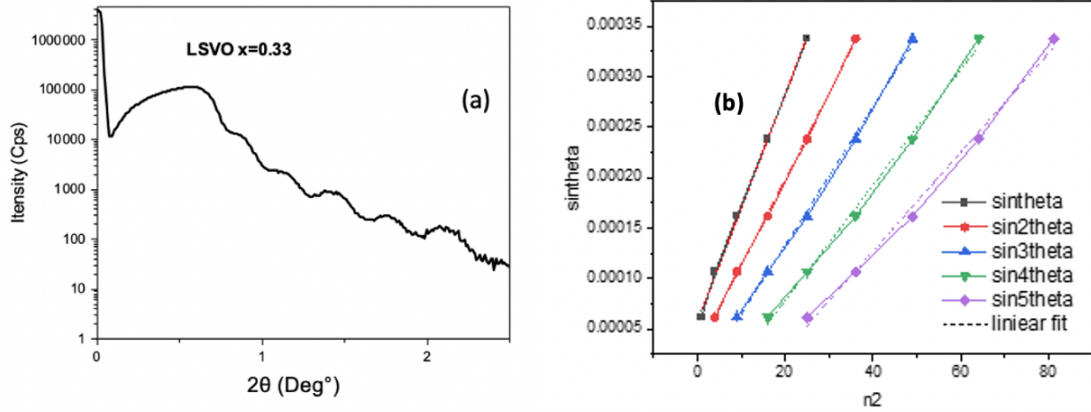


Figure 3.8: Thickness determination methodology (a) Typical XRR profile (b)  $\sin^2 \theta$  as a function of  $n^2$  (considering  $n = 1, 2, 3, 4$  and  $5$ ) and the linear fits. In the shown example,  $n = 2$  is chosen as the correct linear dependence.

Here,  $\theta_m$  is the position at which a maximum of the XRR oscillations is observed, and  $\delta$  denotes the refraction term. This equation indicates an easy method to determine the film thickness. Plotting the measured angles  $\sin^2 \theta_m$  as function of the order number  $N^2$  yields a linear connection, when the good  $N$  is assumed. The film's thickness is given by the slope  $B$  of this line:

$$d = \frac{\lambda}{2\sqrt{B}} \quad (3.6)$$

Consequently, the thickness of the film may be estimated in XRR measurements by determining the slope of this linear connection.

For the measurements, the same Bruker D8 Discover diffractometer as described above has been used, with a monochromatic beam and a slit opening of 0.2 mm. Prior to data collection, exact alignment of the sample height  $z$  and the incidence angle  $\theta$  was done, in order to guarantee the correctness of the acquired data. Here, the  $\theta$  alignment is done using the reflected  $\theta$  beam at an angle above  $\theta_c$ , typically at  $1^\circ$ .

To provide an actual illustration, Figure 3.8 demonstrates the process of estimating thickness. In Figure 3.8 (a), a typical X-ray Reflectivity profile is displayed, basically a LSVO sample with a composition of  $x = 0.33$ . In Figure 3.8 (b),  $\sin^2 \theta$  as a function of  $n^2$  (considering as the order number  $n = 1, 2, 3, 4$  and  $5$  of the first visible

oscillation) is highlighted as the approach employed for thickness determination. As shown, the slope of the optimal fit is used in the equation, yielding an estimation of the LSVO thin film thickness. For this specific example, the estimated thickness is to 22.9 nm.

As PLD samples are rather small ( $0.5 \times 0.5 \text{ cm}^2$ ), the beam size is larger than the sample at low angles. Therefore, the measurements for  $2\theta$  angles below about  $1^\circ$  may include an intensity variation related to the change of the reflected beam size. This contribution is difficult to take into account in an analytical way, so that the analysis of  $\theta_c$  allowing for the determination of the film density is not possible. However, it is possible to integrate the sample size in XRR simulations using dedicated softwares, as for example GenX [112]. In this thesis, the full simulation of the XRR (as for example shown in Figure 3.2) was used only to confirm the thickness values determined by the  $\sin^2 \theta_m$  method. Tests were also carried out in order to determine if the value of  $\theta_c$  and its relation to the electron density can be used to determine the solid solution composition, but the variation was too small to be detectable. The roughness was extracted from the tests showing typical roughness values of atomically smooth interfaces and surfaces.

### 3.3 Spectroscopic measurements

In this thesis, one of the main issues is the demonstration that a solid solution was actually formed in the thin films, deposited by sequential deposition from the parent compound targets. The first aspect is the composition of the thin film, and especially the La/Sr ratio, to confirm the La content in the films. The second aspect is to observe the oxidation state of the transition metal ions, which should undergo a change of the oxidation state when Sr is substituted by La as a sign of the effective introduction of charge in the system. Both of these aspects can be evaluated using spectroscopic measurement allowing for the quantification of the atomic species and the oxidation state. X-ray photoelectron spectroscopy has been carried with Damien Aureau and Mathieu Frégnaux from the ILV Versailles, as well as Vincent Polewczyk, Giovanni Vinai and Piero Torelli from Elettra Trieste. Here, also X-ray absorption spectroscopy (XAS) has been carried out, especially during a beam time in september 2022, reuniting all persons involved in the XPS and XAS measurements.

#### 3.3.1 X-ray photoelectron spectroscopy (XPS)

X-ray photoelectron spectroscopy (XPS) is a technique used for identifying the chemical composition and valence state of elements. It involves the use of X-rays to excite the core-level electrons of atoms within a certain distance of the sample surface in the range of less than 5 nm. In a conventional experimental setup, X-rays of defined energy are directed towards the surface of a sample. These X-rays interact with the core electrons of the sample, resulting in their photoemission, a phenomenon widely recognized as the photoelectric effect as shown in Figure 3.9.

Consequently, the creation of ionized states occurs, leading to the generation of a photoelectron with a certain kinetic energy. This energy can be determined by the difference between the energy of the incident photon and the binding energy of the core electron that has been photoexcited. Additionally, the work function, which varies depending on the material being analyzed, must also be considered. In the context of a solid, the phenomenon of photoemission can be effectively explained

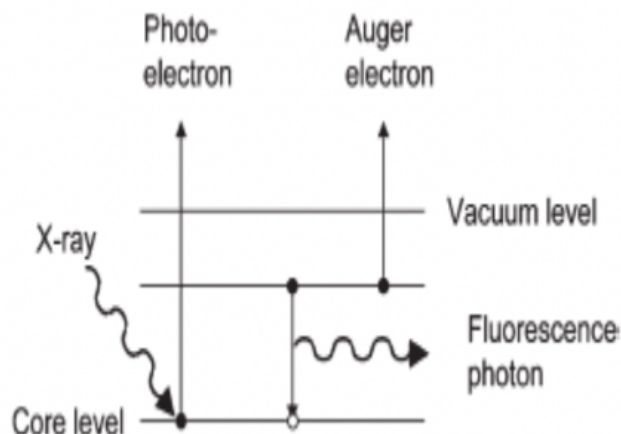


Figure 3.9: Schematic representation of the photoabsorption process of X-rays. [22]

through the production of photoelectrons and Auger electrons initiated by the interaction between X-ray radiation and matter, the scattering processes as they move through the solid surface, and subsequently, the photoelectrons are then liberated from the surface into the surrounding vacuum.

By examining the highest binding energy, we can gain insight into the electronic configuration of the occupied states of the atoms within the sample. Due to the distinct binding energies associated with each element, an XPS spectrum exhibits selectivity in the identification of elements present within the sample being investigated. Furthermore, XPS is not just used for the identification of chemical elements, but also for the identification of alterations in atomic bonding configurations. This phenomenon is observed through modifications in many aspects of the spectrum, including shifts in binding energy, modifications in peak widths and shapes, and the existence of bonding satellites or modifications in the valence band. The chemical shift, denoting a difference in binding energy relative to the elemental state, gives insights into the oxidation states of an element.

At ILV, the XPS measurements were performed on the surface of the samples using a Thermo Scientific  $K\alpha$  X-ray photoelectron spectrometer. Complementary measurements were performed at the Elettra APE beamline using synchrotron radiation as well. The survey spectra were obtained in a binding energy range of 0 – 900eV and fitted. This fitting was an essential part of comprehending the chemical

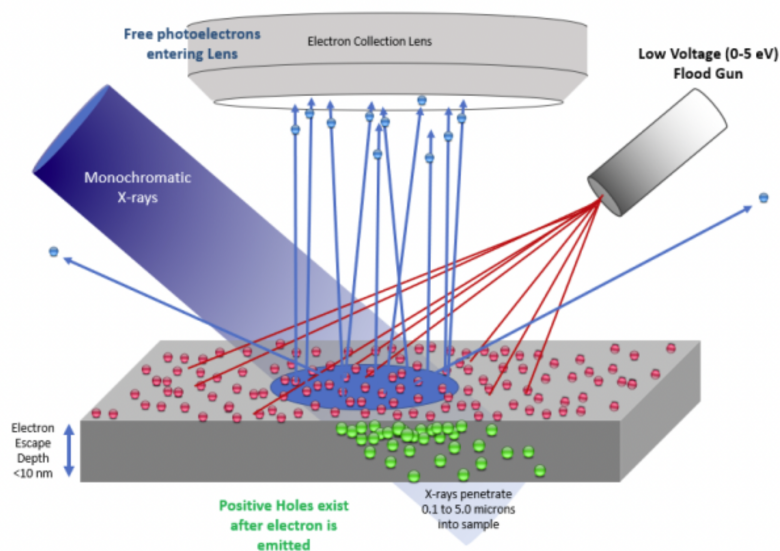


Figure 3.10: Charge compensation using flood gun during the XPS measurement. [23]

environment and bonding that are present in the samples. We applied the Shirley background subtraction approach, which is well regarded for its capacity to account for inelastic background contributions in the core level spectra. In addition, in order to further improve the accuracy of our findings, we utilized symmetric peak morphologies and put constraints on peak locations, widths, and intensity ratios.

The accumulation of surface charge, which can expand and move the peaks and decrease measurement accuracy and precision, is one of the difficulties in XPS analysis. The reason for this charge building is because the sample surface's X-ray photoelectrons have a negative charge that can collect and reject later electrons that are released. A flood gun is frequently employed to get around this problem (Figure 3.10). During the measurement, a flood gun is a low-energy electron source that discharges low-energy electrons onto the sample surface. The electrons released by the flood gun have the same sign (negative) and lower kinetic energy than the photoelectrons released, which balances the surface charge and prevents charge accumulation. In order to neutralize the positive charge that accumulates during XPS measurement, the flood cannon emits low-energy electrons onto the sample surface. These electrons then interact with the surface. The sample surface quickly absorbs the low-energy electrons that are released by the flood cannon due to their short

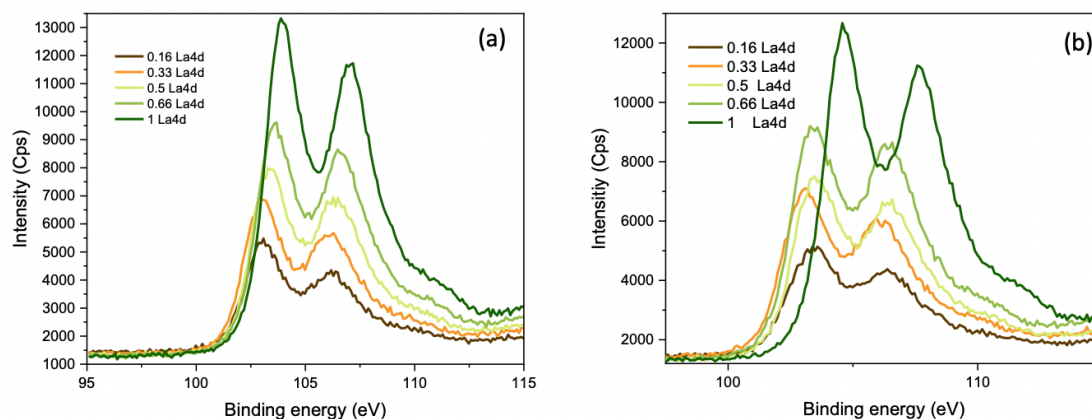


Figure 3.11: La 4d core level XPS spectra of the solid solution thin films (a) with flood gun, (b) without flood gun.

mean free path. As a result, the negative charge is neutralized, allowing surface charging to not obstruct the photoemission process. For accurate measurements, a flood gun is required, especially for insulating materials that have a propensity to charge more quickly. Such a flood gun was used at ILV, and eliminates spectral distortions, increases measurement accuracy and precision, and enables the collection of high-quality spectra by neutralizing the surface charge.

The effect of the flood gun on the reliability of the obtained XPS spectra is well illustrated by measurements on LSVO solid solution films. In Figures 3.11, 3.12 and 3.13, measurements of the core levels of the interesting elements (La, O, V, and Sr, respectively) with and without the flood gun are shown for different solid solution composition. The influence of the sample charging can be observed as shifts of the spectra and intensity differences. When using a flood gun, these features disappear and a reliable analysis of the core levels become possible. All XPS measurements used for the in-depth analysis of the sample composition in this thesis have been conducted with the use of a flood gun.

The experimental procedure involves multiple steps, including the sample preparation, which is typically cleaned and prepared by mounting it on a sample holder. It is worth noting that we performed the experiment on non-water treated samples, before another one of the same samples, but water cleaned. The chamber is evacuated to a vacuum to lower molecules that could interfere with the experiment.

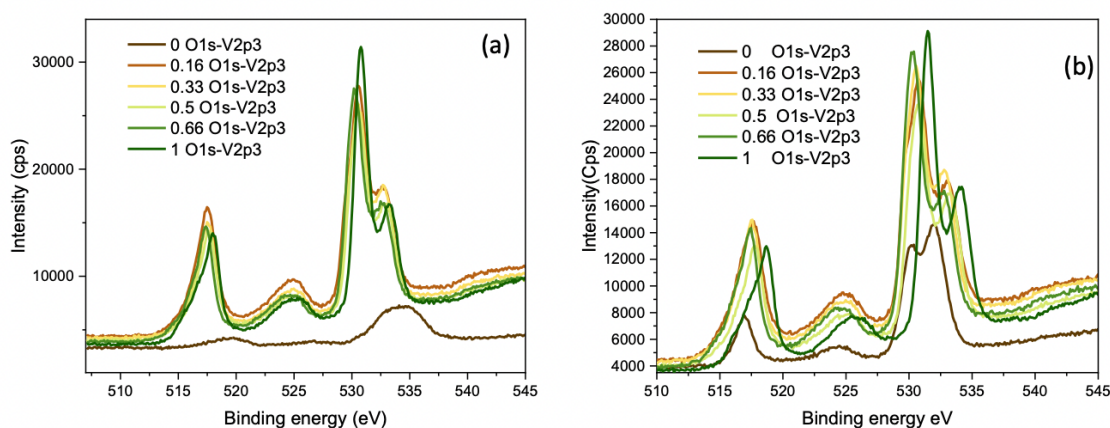


Figure 3.12: O 1s - V 2p3 core level XPS spectra of the solid solution thin films (a) with flood gun, (b) without flood gun.

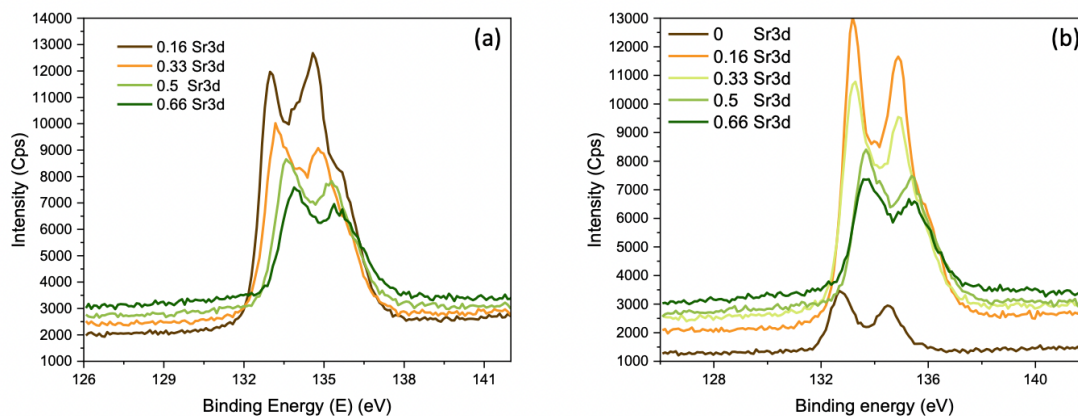


Figure 3.13: Sr 3d core level XPS spectra of the solid solution thin films (a) with flood gun, (b) without flood gun.

Monochromatic X-ray beam generated by aluminium anode irradiates the surface of the sample. The ejected electrons are analyzed using an cylindrical electron analyzer, allowing the measurement of the binding energy.

### 3.3.2 X-ray absorption spectroscopy (XAS)

Electro-magnetic radiation absorption can be used in a wide range of applications to learn plenty of information about a material's physical and chemical properties. X-rays are forms of electromagnetic radiation that have frequencies between UV and  $\gamma$ -rays in the electromagnetic spectrum. The referred to as soft X-rays (100 eV –

3 keV range) and hard X-rays (energies over 3 keV) categories further divide the X-ray radiation. X-rays in particular are able to interact with the internal electrons of the material, or the core electrons. The absorption is the subsequent electronic excitation of the core electron towards an empty molecular orbital, leaving a core-hole. It is known that absorption processes depend on the photon energy of the incident radiation. The electronic structure of the empty states of the absorbing atom is therefore depicted by an X-ray absorption spectrum, which is a scan of the absorption intensity in a given photon energy range, taken in proximity to a particular absorption edge. This electronic structure is associated to certain electronic transitions. This makes it possible, for instance, to learn more about the oxidation state of the atom that is absorbing. The strong localization of the core electron on the absorbing atom, which makes the absorption process highly dependent on its immediate surroundings, is another key benefit of XAS spectroscopy. As a result, core spectroscopies are especially instructive since they may give precise details on the atom's immediate chemical and geometrical environment.

Experimentally, XAS analyzes a sample's absorption coefficient as a function of the incident radiation energy  $I_0$ . For a homogeneous, isotropic material, this absorption coefficient  $\mu$  is described by the Lambert-Beer equation:

$$I = I_0 e^{-\mu D} \quad (3.7)$$

where  $I$  is the intensity of the beam at the distance  $D$  inside the body. For a crystalline solid,  $\mu$  is equal to the sum of the absorption cross sections  $\sigma$  for each of the  $n$  chemical constituents of the unit cell:

$$\mu = \frac{1}{V} \times \sum_{i=1}^n \sigma_i \quad (3.8)$$

where  $V$  is the volume of the unit cell.

When the excitation energy is similar to the binding energy of core electrons, there is a net increase in absorption, which results in the formation of the absorption edges. In non-resonant areas, the absorption coefficient drops with increasing photon energy. Accordingly, each core electron will produce a distinct absorption edge,

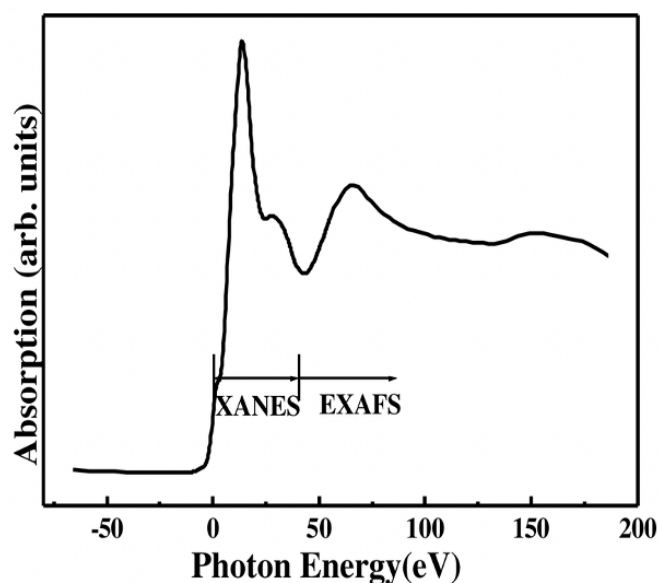


Figure 3.14: X-ray absorption spectrum with the NEXAFS and EXAFS regions.

depending on where in the electronic structure it starts off energetically. This leads to one of the key characteristics of XAS: the ability to choose a single absorption edge by adjusting the incident photon energy. Even with a sample made up of several chemical species, the XAS spectra of a single element may be isolated since the absorption edges of the elements are often energetically separated. Moreover, depending on the initial core level of the excitation, it is also feasible to distinguish various absorption edges for the same element.

The Extended X-ray Absorption Fine Structure (EXAFS) extends from the upper limit of the Near Edge X-ray Absorption Fine Structure NEXAFS (or XANES) region to several hundreds of eV above the absorption edge. The NEXAFS region (Figure 3.14, which covers the energetic range starting from few eV before the absorption edge to 50 eV above it, is divided into three regions according to the X-ray photon energy: the pre-edge, main-edge, and post-edge sections of the NEXAFS region that each provide distinct information about the sample's electronic structure. Experimentally, the sample is exposed to monochromatic X-rays, the energy of which is scanned through a few eV range around the absorption edge of an element.

Due to its extensive energy tunability and special characteristics (high brightness, collimation, and high level of polarization), Synchrotron radiation is the best X-ray

source for carrying out XAS studies. The core-excitation of empty virtual orbitals that takes place when the beam strikes the sample results in a core-hole and the creation of a particle state. Since the excited state has a brief lifetime, the core hole's fate is to be filled, which can occur by one of two processes: fluorescence emission (a non-radiative process) or Auger electron emission (a radiative process). Figure 3.9 illustrates the process of fluorescence, which is the action of an electron in an external shell filling the core-hole and producing a photon with a certain energy. Instead, the Auger effect uses two electrons: the first one fills the core-hole as it decays, but it also transfers energy to the Auger electron, which is subsequently released into the continuum.

In addition, in-situ measurements are possible in order to gather more pertinent information. The extreme sensitivity of Total Electron Yield (TEY) detection, where an electrical contact on the sample is used to collect electrons generated by the absorption of the X-rays, allows to observe carefully all the near-edge features with a probing depth of around 5nm. At the Elettra beamline APE-HE, a well-established cell allowing to perform operando XAS at 1bar fluxing mixture of gases (He, H<sub>2</sub>O vapor and O<sub>2</sub>) at variable temperature was used. The environmental chamber is dedicated to conducting in situ/operando ambient pressure X-ray absorption spectroscopy (AP-XAS) in order to investigate the physical-chemical properties. APE-HE's X-ray Absorption Spectroscopy identifies atomic species located on the surface or buried within the material, exhibiting distinct absorption edges within the energy range of interest (150-1600 eV). AP-XAS experiments are carried out using the TEY mode, which provides surface sensitivity with a probing depth of a few nanometers. To obtain XAS spectra, three picoampmeters are employed. The first picoampmeter records the drain current at the entrance of the sample holder to normalize the incoming intensity, the second measures the drain current of the sample under X-ray radiation, and the third records the drain current of a reference sample that covers the entire energy range. This reference sample serves as a baseline for the photon energy.

The experimental procedure involves a sample preparation and introduction to the chamber. Note here that according to the protocol we developed the samples are

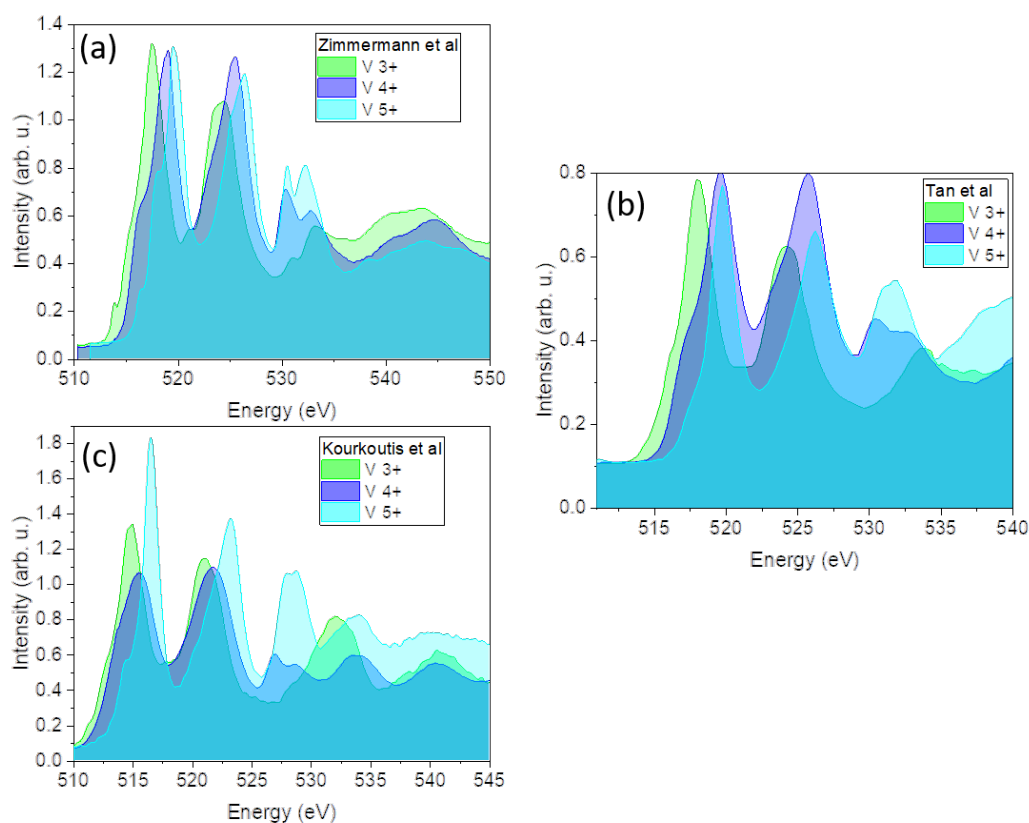


Figure 3.15: L2 and L3 absorption edges of the different oxidation states of vanadium (a) adapted from [24] (b) adapted from [25], and (c) adapted from [9].

cleaned with water before introduction to the chamber. Selecting the appropriate energy range of X-rays, setting up the monochromator, and aligning the X-ray beam. The absorption of the X-rays since they match the binding energy of core electrons, that are detected to create absorption spectrum.

In our study, we developed a method to accurately quantify the oxidation states of vanadium by analyzing the L2 and L3 absorption peaks. Upon existing literature data on vanadium oxidation states (3+, 4+, and 5+), we selected three distinct references from Zimmerman et al [24], Kourkoutis et al [9], and Tan et al [25], representing each oxidation state. Figure 3.15 presents the L2 and L3 absorption peaks for these references, revealing noticeable differences in L2 and L3 intensity.

Figure 3.16 showcases the comparison between each oxidation state of the three different references. We observed that the Zimmerman reference displayed a subtle peak at the L3 bottom, setting it apart from the other references. It's important

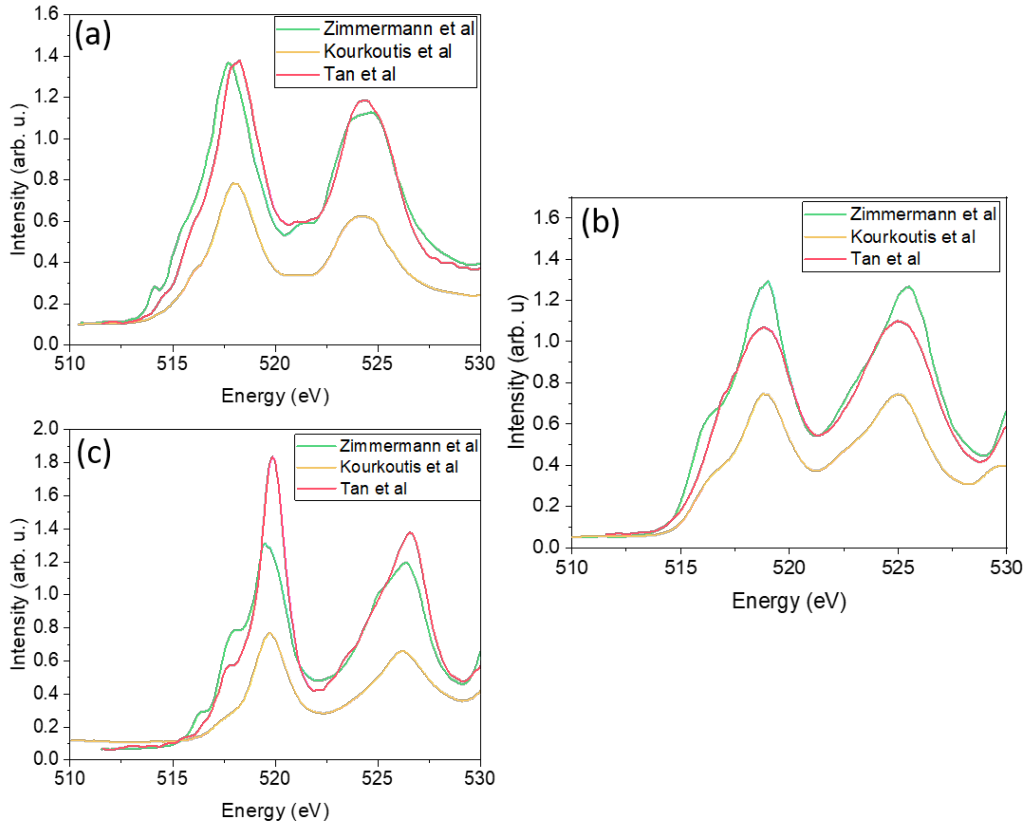


Figure 3.16: Comparison between the three adapted references (a)  $V^{3+}$ , (b)  $V^{4+}$ , and (c)  $V^{5+}$ .

to mention that to overlap the references for comparison, we vertically manipulated the reference data. The Zimmerman [24] and Tan [25] references exhibited similar shapes, while the Kourkoutis [9] reference exhibited slight deviations in the edges of the L2 and L3 peaks. Following this comparison, we opted for the Tan reference due to its closest alignment with our experimental XAS results. Our protocol also delved into different approaches for establishing baselines for both experimental and reference data. We determined that aligning the baselines of L2 and L3 peaks at the same level for all LSVO experimental curves and the Tan reference of  $V^{3+}$ ,  $V^{4+}$  and  $V^{5+}$  yielded the best fit outcomes.

### 3.4 Electrical measurements

In order to ascertain the electrical transport characteristics, it is important in this thesis work to investigate the electrical properties of the thin films. We can identify the electrical conduction modes of our samples by examining the temperature-dependent behavior of the electrical resistance. By tracking the evolution of the resistance under the influence of a perpendicular magnetic field (Hall effect), it becomes feasible to analyze transport characteristics such as the charge carrier density  $n$  and the mobility  $\mu$ . In this work, the electrical characteristics were characterized using a Quantum Design 9 T physical property measuring system PPMS (Figure 3.17). The sample is glued with a thermally conducting, but electrically insulating varnish to the sample puck. Three samples can be measured on the same puck. The sample is connected to the electrical contacts on the side of the sample holder, which is introduced into a chamber in the PPMS, under He. The puck is connected to an electrical contact in the bottom of the PPMS chamber so that the sample is sitting in the center of superconducting coils allowing it to generate fields up to 9 T perpendicular to the plane of the puck. The electronics of the PPMS generate the necessary signals for the measurements and collect the data.

Figure 3.17 (a) illustrate the schematic representation of the PPMS. Inside, stage

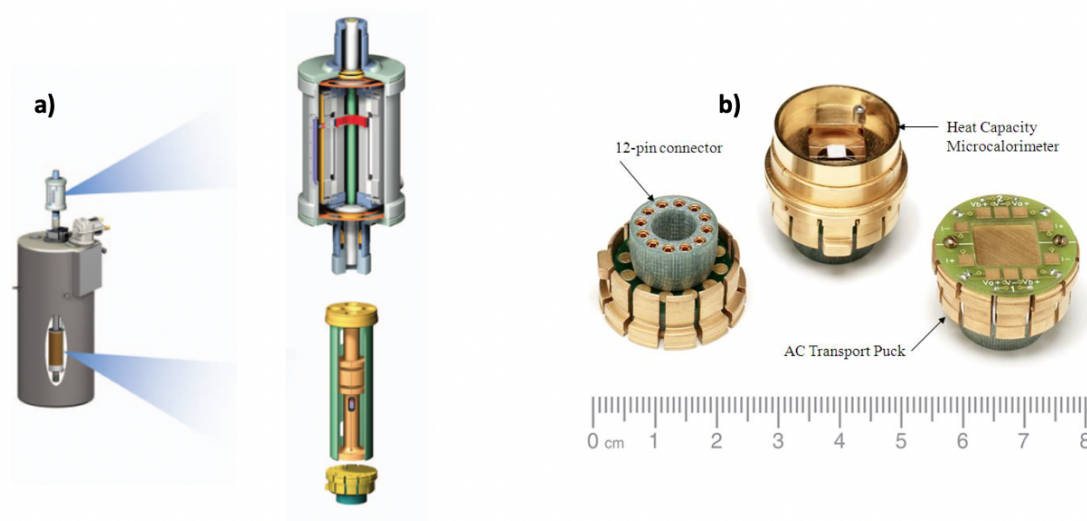


Figure 3.17: (a) Schematic representation of the PPMS, (b) details of the sample puck

for holding different samples, cooling system using liquid helium and a refrigerator to reach very cold temperatures, strong magnet to reach important magnetic field, sensors to measure temperature, windows to see the experiments, and systems to control gases or vacuum conditions. Figure 3.17 (b) on the other hand shows typical sample puck holder used to carry 3 samples in our case.

### 3.4.1 Electrical resistivity

The experimental procedure for measuring electrical resistivity on a thin film sample involves using a four-point arrangement. In contrast to the two-point design, the measurements of intrinsic resistance in this setup are not influenced by contact resistance. A West Bond ultrasonic wirebonder was used to establish electrical contacts between the sample and the measurement support, using a 25  $\mu\text{m}$  Si-doped Al wire. This alloy allows for low resistance contacts on the sample surface and exhibits remarkable stability at low temperatures. The electric potential is determined by the voltage difference between  $V^+$  and  $V^-$ , while the current is injected in the direction from  $I^+$  to  $I^-$ . The contacts are distributed over the surface in the van-der-Pauw geometry, where the four contacts are made in the four corners of the square samples. The voltage contacts are located on one side of the samples, while the current contacts are located on the other side, with parallel polarisation. The experimental procedure involves analyzing the resistance evolution within the temperature range of 10 to 300K. This analysis is conducted using a PPMS (Physical Property Measurement System), which possesses a sensitivity capable of measuring values ranging from  $10^{-4}$  to  $10^7 \Omega$ . The injected current is automatically optimized for the voltage range being measured. Using the following formula, the electrical resistivity  $\rho$  is determined from the measured resistance  $R$  in the van-der-Pauw configuration:

$$\rho = R_S \times t = \frac{\pi R t}{\ln 2} \quad (3.9)$$

where  $t$  is the film thickness and  $R_S$  is the sheet resistance.

The temperature dependent resistance measurements were carried out during cooling from 300K to 5 or 10 K; with a cooling rate of 4K/min in order to ensure

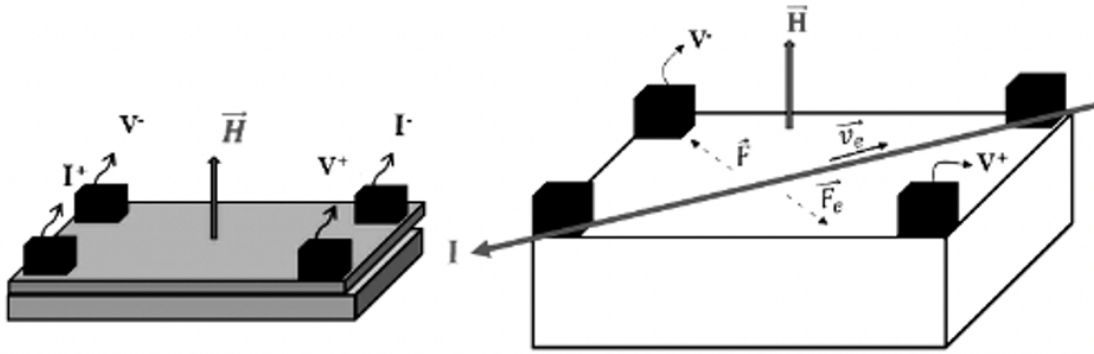


Figure 3.18: Hall measurement in Van Der Pauw configuration. [26]

the good thermalization of the sample.

### 3.4.2 Hall effect

The Hall effect of the thin films were also measured using the Van Der Pauw set-up (Figure 3.18). The same contacts were used as for the resistivity measurements, but the attribution was changed so as to measure the perpendicular resistance, i.e. the Hall resistance, as depicted in Figure 3.18(a). The velocity of charge carriers is dependent on the current density, and their motion generates a Hall electric field ( $E_H$ ) in response to the Lorentz force related to the magnetic field  $H$ . The outcome entails a perpendicular deviation and the emergence of a Hall resistance denoted as  $R_{xy}$ . The Hall coefficient, or  $R_H$ , is the term used to denote the slope of  $R_{xy} = f(H)$ .

$$R_H = \frac{\Delta R_{xy}}{\Delta H} \quad (3.10)$$

This enables using the following equations to calculate the charge carrier density  $n$  and the mobility  $\mu$ :

$$\begin{aligned} n &= \frac{1}{R_H \times e} \\ \mu &= \frac{1}{en\rho} \end{aligned} \quad (3.11)$$

where  $e$  is the electronic charge.

The Hall effect measurements were carried out scanning the magnetic field from -9 T to +9T at different temperatures distributed from 10 K to 300K. Linear fits were carried out to determine  $R_H$  at each temperature.

## 3.5 Optical measurements

### 3.5.1 Perkin Elmer Spectrophotometer: Measurement of optical transmission and reflection.

Optical properties manifest in at least three effects: transmission, reflection, and absorption. These three effects can be characterized by the following parameters: Transmittance (T), Reflectance (R), refractive index (n), and also the absorption coefficient (k).

During this thesis work, the optical transmission and reflection of our samples were measured using a Perkin Elmer 1050 Lambda UV-Vis-NIR spectrophotometer and a Universal Reflectance Accessory (URA). Optical transmission measurement involves directing a monochromatic light beam onto the sample. From an experimental perspective, the incident beam is first split into two, after passing through a monochromator, using a splitter to irradiate both the sample area and the reference area (see Figure 3.19 ). This will serve as a reference to determine the optical transmission of the sample. Indeed, before each measurement, it is necessary to calibrate the optical transmission to 100% by placing a reference material such as fused silica, which has a transmission of 95%.

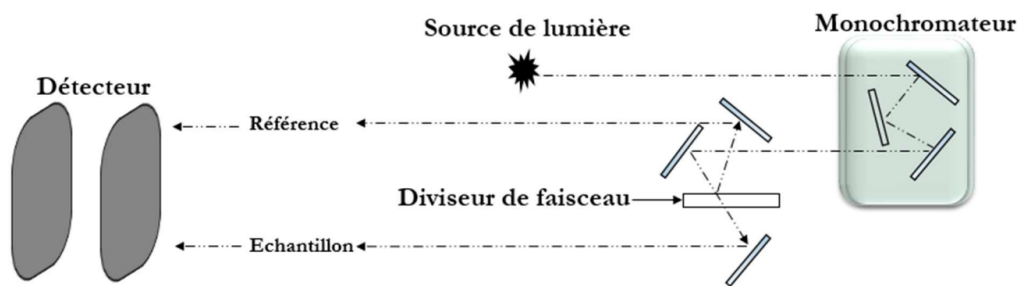


Figure 3.19: Schematic representation of Perkin Elmer 1050 UV-vis-NIR

Optical reflection, on the other hand, was measured in the visible range using a URA spectrophotometer. As illustrated in Figure 3.20, the light beam is focused along an optical path onto the sample. During this work, the sample is illuminated at a nearly normal incidence angle of  $8^\circ$  by a monochromatic beam with a size of  $(2 \times 2 \text{ mm}^2)$ . It is important to calibrate the system before each measurement. To do this, by adjusting mirrors, the beam from the compensator is focused directly onto the detector to set the initial optical reflection to 0%.

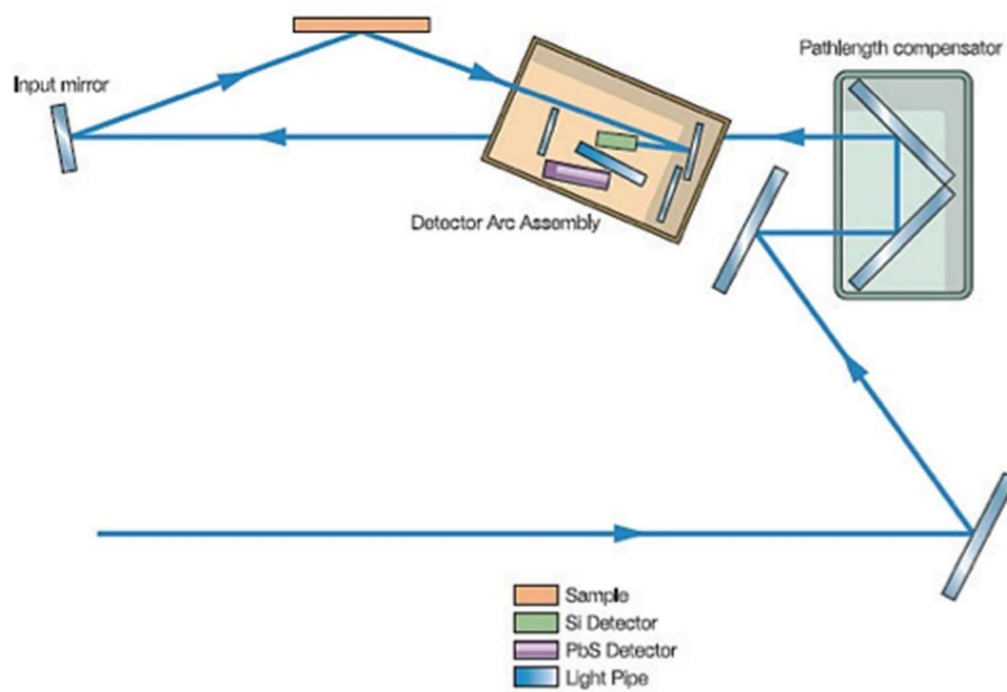


Figure 3.20: Schematic representation of Perkin Elmer 1050 UV-vis-NIR



## CHAPTER 4

---

### (La,Sr)VO<sub>3</sub> solid solution thin films

---

The lanthanum strontium vanadium Oxide (LSVO) system has attracted a lot of interest because of the properties that make it of potential use in transparent electronics, optoelectronics, solar cells, and solid oxide fuel cells. This Perovskite-type transparent conducting oxide (TCO) has generated a great deal of interest because of the unusual combination of optical and electrical properties it possesses. The effects of doping (section 4.2) and strain engineering (section 4.3) on the structural, electrical, and optical characteristics of the LSVO system will be covered in this chapter, after a thorough analysis of the structural quality and the effective formation of a solid solution (section 4.1). Also, the chemical modification of the surface will be studied, in order to understand the influence of La doping on the chemical instabilities of SVO (section 4.4).

## 4.1 Growth of solid solution thin films

### 4.1.1 Growth optimization

In order to assess the optimal growth conditions of the solid solution thin films, first, the growth of the parent compound single films has been studied and the influence of the main growth parameters. We have decided to grow the thin film material on a (001) oriented SrTiO<sub>3</sub> (STO) substrate to assess the effect of the La concentration on the material. This choice was made because the thin film will experience less strain than on other substrates, such as the commonly used (LaAlO<sub>3</sub>)<sub>0.3</sub>(Sr<sub>2</sub>TaAlO<sub>6</sub>)<sub>0.7</sub> (LSAT). Using STO, we can isolate the impact of the doping content on the material's characteristics without interference from excessive strain. The growth of LaVO<sub>3</sub> (LVO) has been optimized earlier during the thesis of H el ene Rotella at the CRISMAT [87, 113, 114], and the growth of thin films of SrVO<sub>3</sub> (SVO) deposited on STO was optimized by Alexis Boileau [13, 14], so that only a reduced optimization process was necessary, taking into account mainly the deposition temperature. The other parameters were fixed to the standard parameters mentioned in chapter 3.1.1.

Figure 4.1 shows the XRD  $\theta - 2\theta$  scan of about 20 nm thick films of SVO and LVO on STO (001) substrates, deposited at temperatures between 400 and 700 °C. The position of the Bragg peak of the SVO films does not depend on the depo-

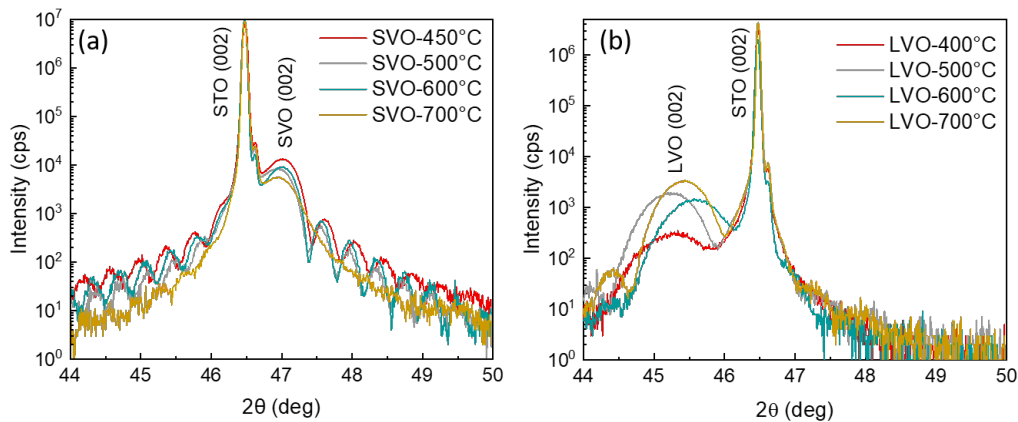


Figure 4.1:  $\theta - 2\theta$  scan of the (002) reflection of the STO and the SrVO<sub>3</sub> (a) and LaVO<sub>3</sub> (b) thin films at various deposition temperatures

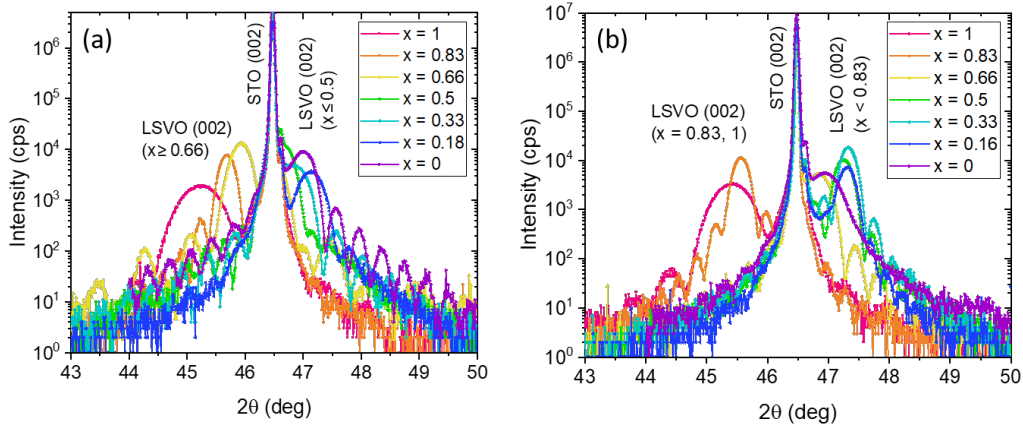


Figure 4.2:  $\theta - 2\theta$  scan of the (002) reflection of the STO and the LSVO solid solution set for a deposition temperature of (a) 500 °C and (b) 700 °C.

sition temperature, but the film quality does. With elevated temperature, above 600 °C, the intensity of the Laue fringes of the Bragg peak decreases, indicating a deteriorating film quality. On the other hand, the LVO films show a stronger temperature dependence regarding the Bragg position, but also its width. Here, the low deposition temperatures lead to a wide and less intense Bragg peak, indicating lower film quality. When enhancing the deposition temperature, the Bragg peak becomes more intense and narrow, and some Laue fringes are observed for a deposition temperature of 700 °C. Therefore, while SVO shows a better quality at low deposition temperatures (as was already observed before [13]), LVO needs high deposition temperatures for a good quality.

Based on the parent compound optimization results, the optimal growth temperature for the solid solution required two distinct temperatures, mainly 500 °C and 700 °C. For both temperatures, five different compositions of  $\text{La}_x\text{Sr}_{1-x}\text{VO}_3$  thin films were grown with values of  $x$  as following: (0,0.16,0.33,0.5,0.66,0.83,1). While the subsequent section will delve more deeply into the set grown at 500 °C, it is essential to present some experiments and findings from the solid solution set grown at 700 °C, which contributed to the choice of pursuing the study at 500 °C.

Figure 4.2 depicts the XRD  $\theta - 2\theta$  of the different solid solution compositions grown on STO substrates at a temperature of 500 °C (a) and 700 °C (b). For both deposition temperatures, Bragg peaks are observed of the thin film for all compo-

sitions. The Laue fringes prove the good level of crystalline quality observed in all of the solid solution samples. It is interesting to note that although 500 °C is not an optimal temperature for pure LVO, the presence of Laue fringes sets in at  $x = 0.83$ , showing that even a small content of Sr stabilizes the film. A comparable mechanism is observed for the 700 °C solid solution on the Sr rich side: although the pure SVO film shows a rather feeble crystalline quality, the only lightly La-doped solid solution  $x = 0.16$  shows the presence of Laue fringes. Therefore, both deposition temperatures lead to high quality solid solution thin films. XRR measurements were conducted on all solid solutions, revealing a thickness of approximately 20 nm for all thin films, consistent with the calibration procedure results. Here, the genX software was employed to determine the thickness by fitting the XRR curves.

The observed shifts in Bragg peaks, which increase in position with increasing La content, provide confirmation of the distinct compositions achieved in the solid solution. In principle, the structural characterization confirmed the successful growth of the set at both temperatures, thereby demonstrating a good level of crystalline quality. Figure 4.3 illustrates the evolution of the out-of-lattice parameter with the lanthanum doping, presenting in both cases a non-linear trend. The observed behavior will be thoroughly explained in the following sections of the LSVO solid solution grown at a temperature of 500 °C, but some general features should be noted here. First,  $c$  differs for  $x \leq 0.5$ , where the samples grown at 700 °C show smaller values than for the samples grown at 500 °C. This behaviour was also observed for pure SrVO<sub>3</sub> grown on SrTiO<sub>3</sub> [13], which was shown to be strongly related to the presence of oxygen vacancies, due to the higher diffusion mobilities at higher deposition temperature. The La-rich solid solution  $x = 0.83$  film show on the other hand quite comparable lattice parameters for both deposition temperatures.

The main obstacle was encountered during the process of electrically characterizing the solid solution grown at 700 °C. As illustrated in Figure 4.4, most compositions for  $x \leq 0.66$  showed a metallic temperature dependence. But significantly, Figure 4.4 (b) presents the Hall effect observed in the 0.66 composition, demonstrating an S-shape Hall effect, which is commonly associated with hall anomalies. This observation suggests the existence of magnetism or the simultaneous presence of two

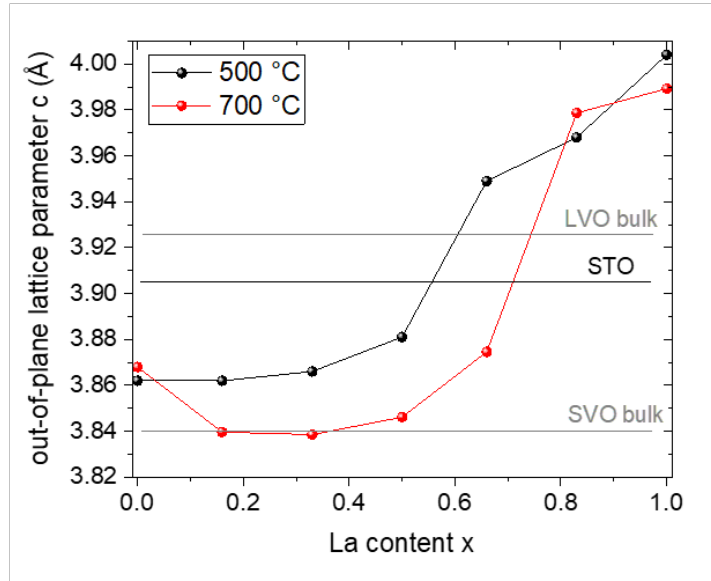


Figure 4.3: Evolution of the out-of-plane lattice parameter  $c$  with lanthanum content  $x$  for the two deposition temperatures. The horizontal lines indicate the lattice parameters of  $\text{SrVO}_3$ ,  $\text{LaVO}_3$  and  $\text{SrTiO}_3$  bulk value.

types of charge carriers, which may be again related to oxygen vacancies either in the substrate [115] or the film. Therefore, based on the absence of electrical anomalies within the samples grown at 500 °C as will be presented in the following sections, the 500 °C temperature was chosen to be the optimal parameter for the LSVO solid solution study.

From the measurements of reciprocal space maps of the (103) reflections of the film and the substrate (an example is shown in 4.5), the coherently strained state of the whole solid solution on the STO substrate is observed, as was also reported in earlier studies on SVO [13] and LVO [114]. The analysis of the out-of-plane lattice parameter  $c$  (Figure 4.4) with the evolution of the lanthanum content  $x$  in the solid solution shows two different regimes (1) and (2). In the first domain (1) with  $x < 0.4$ ,  $c$  slowly increases from 3.86 Å ( $x = 0$ ) to 3.87 Å ( $x = 0.33$ ). Exceeding 40% La doping, the slope changes, and  $c$  seems to increase more quickly from 3.88 Å ( $x = 0.5$ ) to 4.00 Å ( $x = 1$ ). Therefore, the  $c$  evolution with La content is not linear throughout the LSVO solid solution. Such a non-linear evolution is often interpreted in bulk as a sign of lacking substitution. However, in thin films, the strain also plays an important role on the obtained  $c$ . The change of the slope is

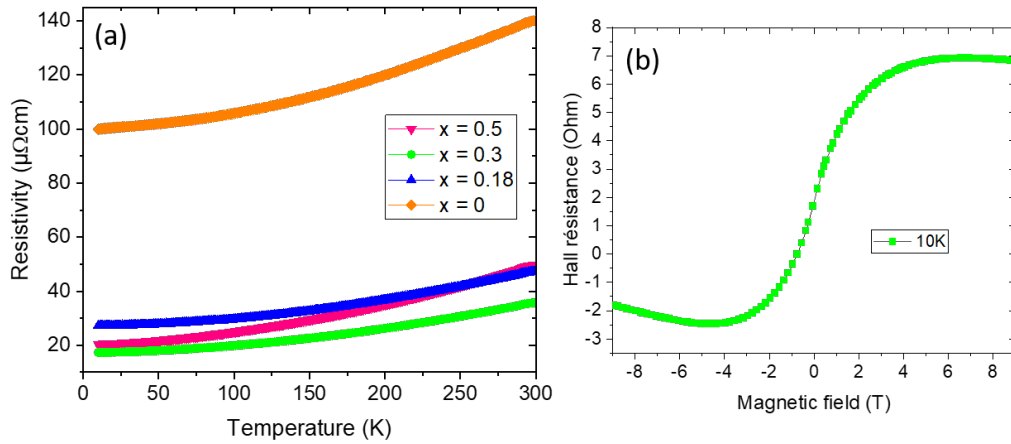


Figure 4.4: (a) Evolution of the resistivity of the conductive LSVO samples with the temperature (b) Hall effect at 10K of the composition  $x = 0.66$ .

observed when  $c$  becomes larger than the STO lattice parameter,  $a_{STO} = 3.905 \text{ \AA}$ . Therefore, the strain state of the film changes from tensile strain in regime (1) to compressive strain in regime (2), corresponding to a strain-reduced  $c$  in regime (1) and a strain-enhanced  $c$  in regime (2). Thus, the obtained evolution is coherent with

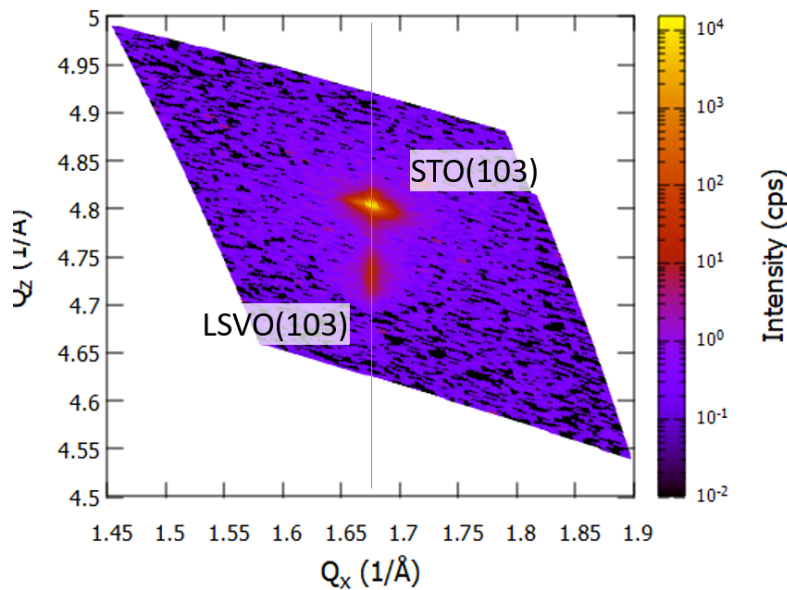


Figure 4.5: (a) Reciprocal Space Map of the (103) reflection of the STO substrate and the LSVO film with a La content of 83 %

a homogeneous solid solution and the related lattice parameter change, undergoing a strain state change on the chosen substrate.

### 4.1.2 Chemical characterisation

In order to determine more precisely the La content and the effect of La substitution on the V oxidation state, spectroscopic measurements were carried out on the solid solution grown at 500 °C. Figure 4.6(a) shows the XPS survey measurements used to determine the composition of the film by the relative intensity of the signal related to the different elements. After Gaussian fitting and Shirley background removal, the content of the single elements was calculated from the O, C, Sr, La and V peak regions. A spectrum decomposition with holographic deconvolution was used to identify spectral lines, with a targeted peak deconvolution algorithm. In order to corroborate the XPS quantification, a scanning electron microscope with energy-dispersive X-ray spectroscopy (EDS) was also performed. Due to the thin film form of the sample, the EDX measurements suffer from a small interaction volume of the beam with the interesting material, and the presence of Sr in the substrate is a second hindrance to quantify exactly the La/Sr content of the film. We have used comparative measurements of the single film  $\text{LaVO}_3//\text{SrTiO}_3$  sample with the solid solution samples, and we were able to estimate a La content, but the reliability of these results is small, accounting for the large error bars. Figure 4.6(b) shows the experimentally obtained composition of the samples for three compositions, using the average of the XPS and EDX results. It can be observed that the experimental values are slightly higher than the nominal values for  $x \leq 0.5$ , but stay very close. Therefore, the calibration process is reliable, and in the following, the nominal compositions will be used for the analysis.

In order to confirm the homogeneous integration of the lanthanum into the solid solution, XPS measurements of the La4d core spectra were carried out on all the solid solution films containing La. Figure 4.7(a) shows the evolution of the spectra with the doping content. As  $x$  increases, a corresponding increase in the intensity of the La 4d core level signal can be observed, as assessed by the increase of the integrated area of the peaks (Figure 4.7(b)). This indicates that, as the number

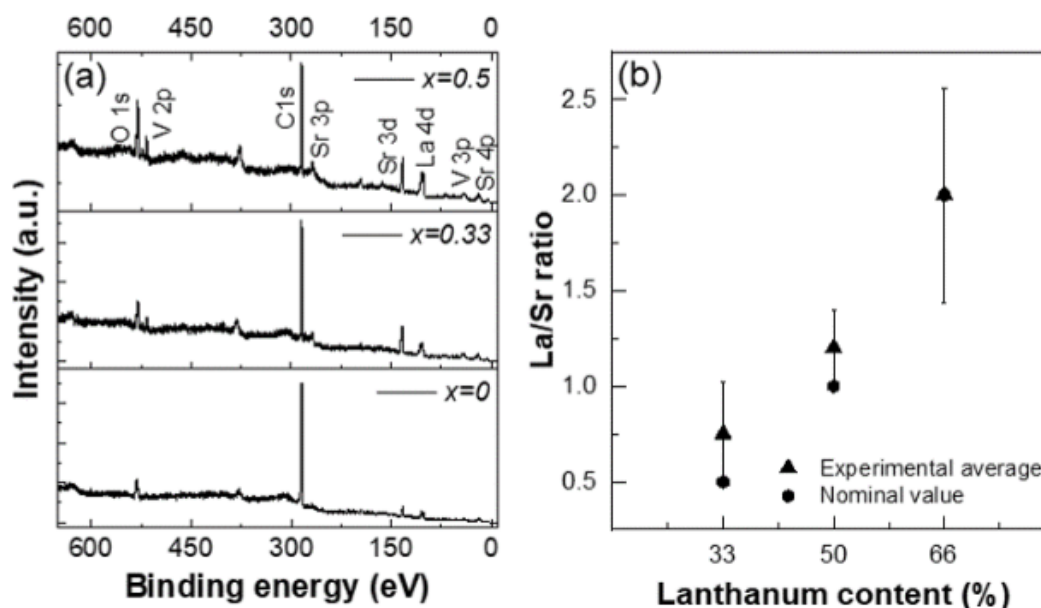


Figure 4.6: (a) XPS survey spectra of LSVO solid solution thin films for specific  $\text{La}_x\text{Sr}_{1-x}\text{VO}_3$  compositions ( $x = 0$  bottom panel, 0.33 middle panel, and 0.5 top panel) (b) Experimental composition extracted from the average of XPS and EDS vs nominal composition.

of laser pulses on the  $\text{LaVO}_4$  target increases, the La concentration within the film increases also. The shift in La core levels is due to the change of the binding energy caused by the changes in the chemical environment of the atoms. The doping alters the electronic structure of the material, leading to changes in the band structure and Fermi level, and thus a shift of the core levels. At the same time, the intensity of the Sr core level (Figure 3.13 in section 3.3.1) decreased as the doping concentration increased. Nevertheless, no discernible changes in the intensity of the V 2p3 and O 1s core levels were seen (Figure 3.12 in section 3.3.1). Therefore, on the whole solid solution range, La is well substituted for Sr.

Analyzing core levels can provide us a variety of details on the surface's chemical composition and electrical structure. But also, the chemical state of the atoms on the surface, including the existence of chemical bonds and their kind, may also be determined via core level analysis. The Figure 4.8 shows an insight on the core levels of the  $x = 0.5$  solid solution set before and after water treatment. Collecting the measurements with and without water treatment allowed for a precise evaluation of the solid solution's surface composition while taking into account the possible

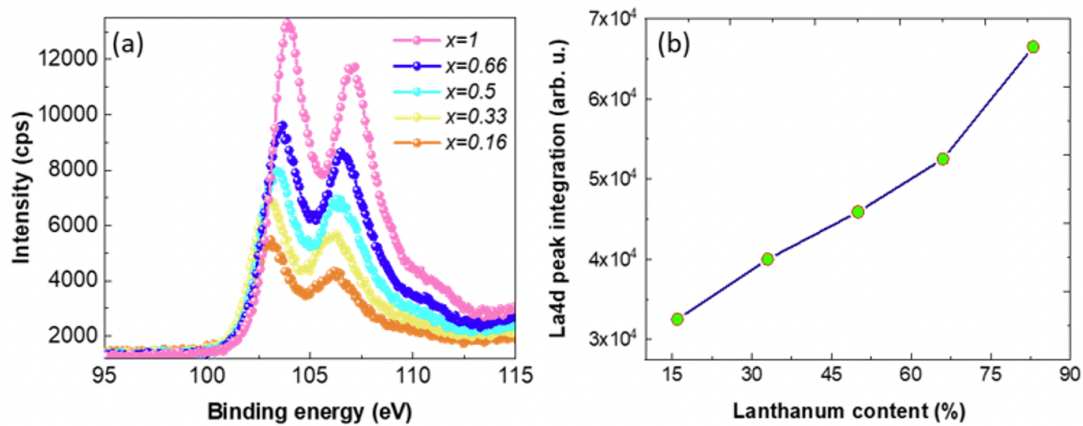


Figure 4.7: La 4d core level XPS spectra (a) of the solid solution films and (b) the integrated area of the core levels.

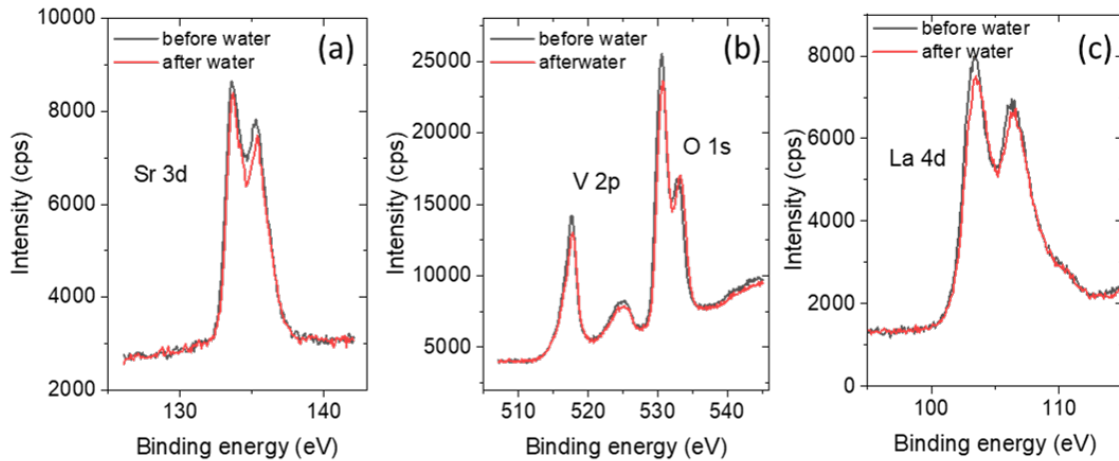


Figure 4.8: Core level XPS spectra of the  $x = 0.5$  solid solution thin film before and after a surface water treatment.

surface oxidation of lanthanum strontium Vanadate. In Figure 4.8, only a very small difference is observed between the pristine surface and the water treated one, indicating a less reactive surface as for pure SVO. This is either related to the fact that the La doping stabilizes the  $V^{4+}$  at the film surface, or that the La doping leads to a non-solubility in water of the  $V^{5+}$  containing surface oxides.

The La/Sr ratio has also been determined before and after the water treatment (Figure 4.9). The determined ratio is very similar before and after the water treatment, and also to the nominal value. This observation indicates that the measured La/Sr ratio is robust against surface ageing or surface treatment, again enhancing

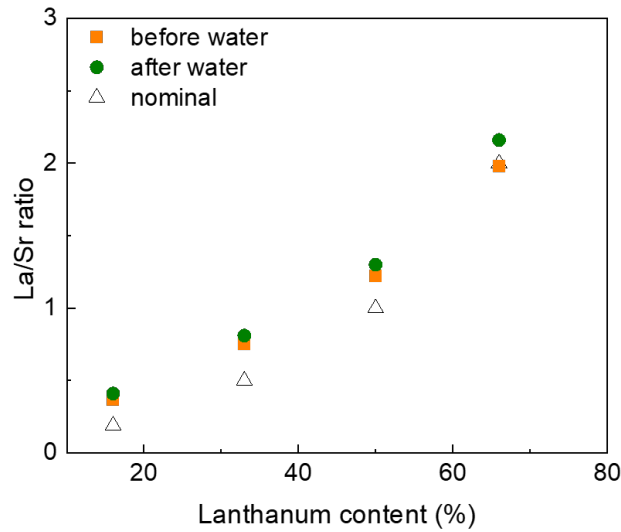


Figure 4.9: Experimental La/Sr ratio determined from XPS measurements before (orange squares) and after (green circles) the water treatment of the LSVO solid solution samples. The nominal La/Sr ratio is indicated by open triangles.

the reliability of the calibration process and the deposition process.

Figure 4.10 shows the fitting performed on the Sr 3d core levels for 4 different compositions. strontium exhibits two prominent peaks, denoted as Sr 3d<sub>5/2</sub> and Sr 3d<sub>3/2</sub>. The observed peaks serve as distinctive markers, that indicate the interconnections between strontium and other elements. The Sr 3d<sub>3/2</sub> peak exhibits a slightly higher energy level (1.8 eV) compared to the Sr 3d<sub>5/2</sub> peak. Two Sr contributions are observed in the spectra. The one at lower energy relates to the strontium atoms located in the perovskite structure in close proximity to the surface, specifically within the lattice component. The high-energy region corresponds to the presence of termination on the surface of the perovskite. [108]

The results highlight an increase of the surface strontium contribution in the sample, which is pretty coherent with the segregation of the strontium on the surface with the ageing effect. This observation confirms that the water treatment seems to be less effective on the highly-doped lanthanum samples, as the composition  $x = 0.5$  shows more pronounced surface strontium than the composition  $x = 0.16$  or  $x = 0.33$ .

To learn more about the development of the vanadium oxidation state, we carried

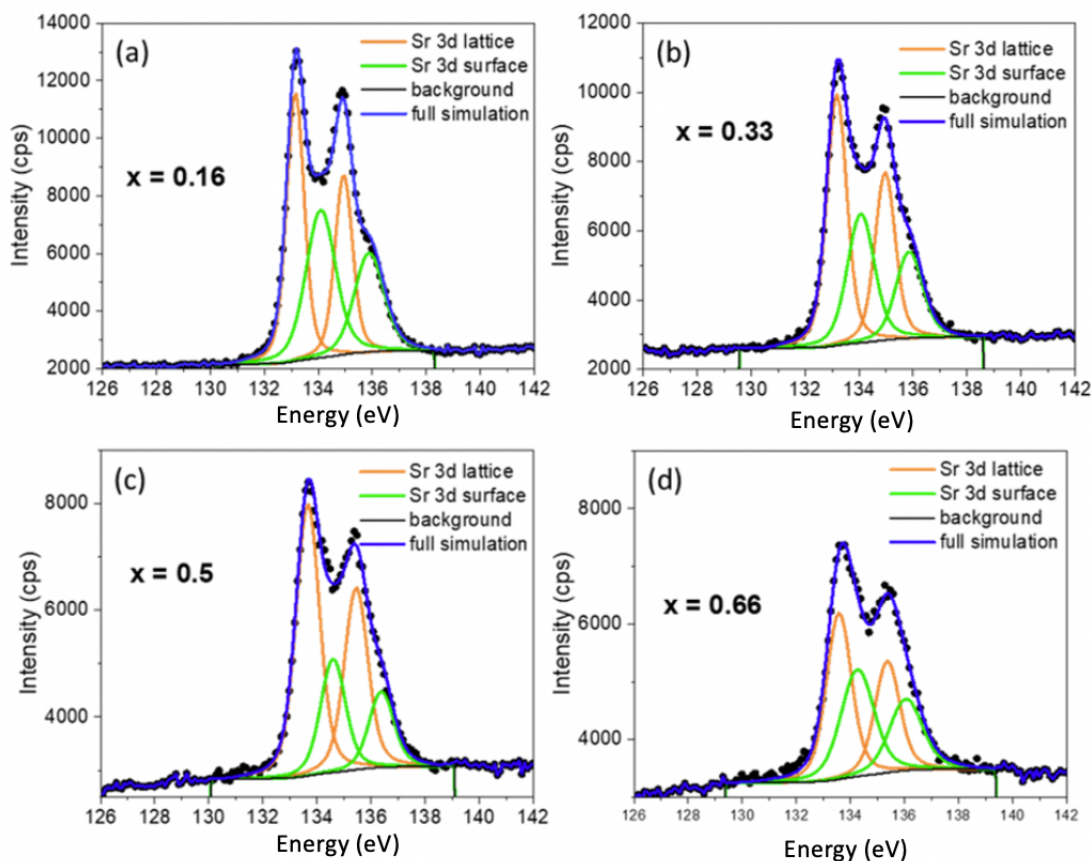


Figure 4.10: XPS Sr 3d core level spectra (black circles) with fit: Sr lattice contribution (orange line), Sr surface contribution (green line) and the full simulation (blue line).

out a similar experiment on the V 2p3 core levels (Figure 4.11). The examination of the variations in vanadium oxidation states within the solid solution presents an intriguing outcome. The variation of oxidation states is not as significant as expected, especially when compared to the noticeable impact of lanthanum doping. Therefore, the application of X-ray Absorption Spectroscopy (XAS) presents itself as a highly appealing process for further investigation.

The XAS spectra of the vanadium L2 and L3 edges for compositions  $x = 0.16$ , 0.33, 0.5, and 0.66 are presented in Figure 4.13, together with the parent compound single films.

It was possible to identify the proportionate contribution of each vanadium oxidation state inside the thin films by fitting the experimental XAS data with these three components, giving us a more comprehension of the electrical structure and

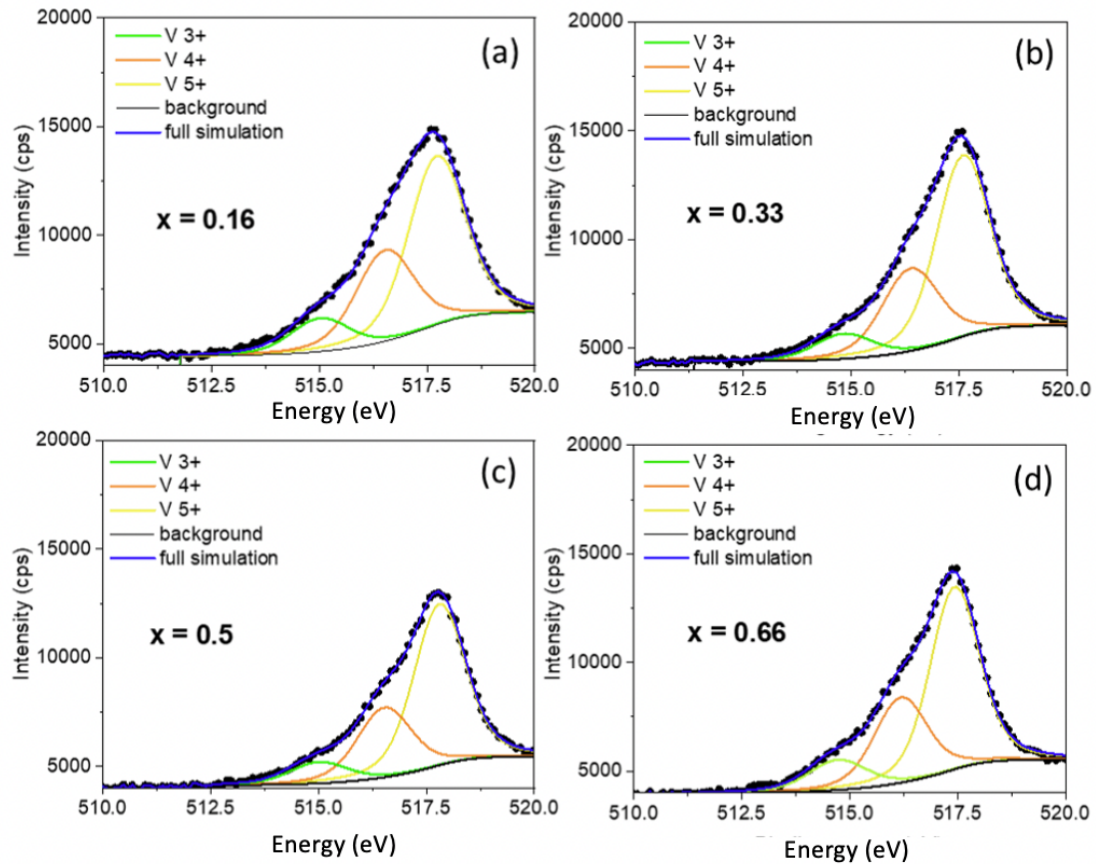


Figure 4.11: XPS V 2p<sub>3</sub> core level spectra (black circles) with fit: V<sup>3+</sup> contribution (green line), V<sup>4+</sup> contribution (yellow line), V<sup>5+</sup> contribution (green line), and the full simulation (blue line).

local atomic environment. This quantitative approach enables an evaluation of the function of lanthanum doping and its influence on the distribution of vanadium's oxidation states in the presence of various gaseous environments.

Regarding the vanadium oxidation states and their relationship to lanthanum doping levels, focusing first on the initial state, which occurs before any gas exposure. As the lanthanum doping level increases, there is a noticeable rise in the V<sup>3+</sup> oxidation state. Therefore, the V ions change their oxidation state upon introduction of La into the lattice, which is a sign of the effective charge doping of the solid solution. As the composition changes from pure strontium Vanadate (SVO) to lanthanum-doped strontium Vanadate with  $x = 0.16$  (LSVO), the fraction of the V<sup>4+</sup> state is not strongly impacted. However, when  $x$  outreaches this value, the V<sup>4+</sup> contribution strongly decreases, while the V<sup>5+</sup> contribution increases. Several

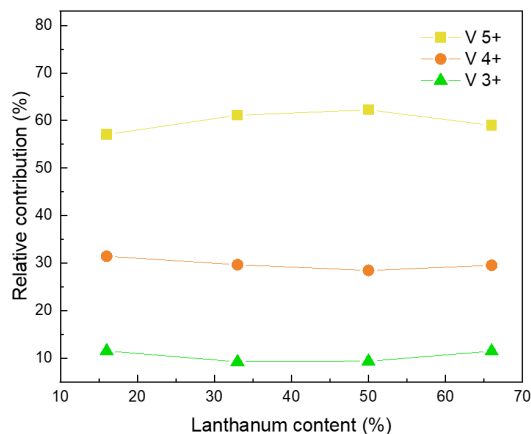


Figure 4.12: Relative contribution of the different V oxidation states to the XPS V 2p3 core level as a function of the La content

causes may have contributed to this V<sup>5+</sup> and V<sup>4+</sup> oxidation states' development. The effect of lanthanum doping on the local atomic and electronic structure of the vanadium site is one hypothesis that could apply. lanthanum may produce local distortions when it enters the lattice, changing the chemical environment of vanadium and impacting the distribution of its oxidation states. Additionally, fluctuations in the lattice parameters due to the ionic radii differences between the Sr and La ions may affect the vanadium oxidation states. It is significant to highlight that the fitting procedure used to deconvolute the vanadium L2 and L3 edges is naturally complicated, and several difficulties were encountered throughout the study. Therefore, to enable comparisons between the various spectra, our main attention was on recreating the contour of the L2 edge, while placing less emphasis on the L3 edge. This decision was taken as a result of the L2 edge's more well-defined characteristics and greater signal-to-noise ratio, which make it more suited for such analyses. The quantification of the vanadium oxidation states, however, may be affected in various ways by this method, perhaps resulting in an under- or overestimation of some of the oxidation state fractions.

Another possibility is that the water treatment, to which these samples were submitted before the measurements, is less effective when La is doped into the lattice. In pure SrVO<sub>3</sub>, the chemical modification of the surface leading to the V<sup>5+</sup>

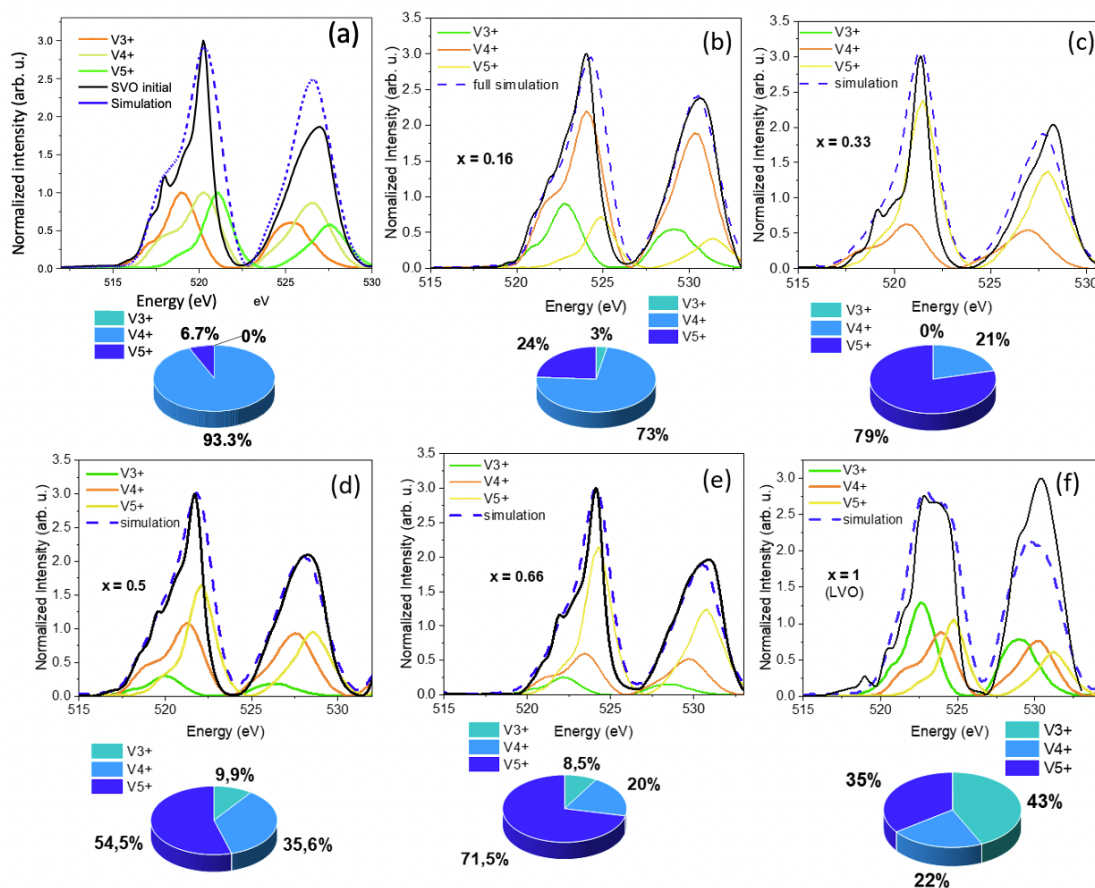


Figure 4.13: XAS spectra of the V L<sub>2,3</sub> edge for a SVO single film (a),  $x = 0.16$  (b),  $0.33$  (c),  $0.5$  (d) and  $0.66$  (e), and a LVO single film (f). Data is shown in black, the contributions of the V<sup>3+</sup>, V<sup>4+</sup> and V<sup>5+</sup> as green, orange and yellow line, respectively. The full simulation is shown as a blue dashed line. In the bottom of the panels, the quantification of the relative contribution of the three V oxidation states is displayed in shades of blue.

state is related to the formation of Sr<sub>2</sub>V<sub>2</sub>O<sub>7</sub> [116] or Sr<sub>3</sub>V<sub>2</sub>O<sub>8</sub> [109]. These oxides are soluble in water [117], leading to the cleaning effect of the water treatment. However, when doped with La, also these surface oxides will be doped with La, reducing their water solubility. This may be also the reason why the XPS shows a stable V oxidation state distribution with La doping, as the small penetration depth of the technique does not allow to sample the film underneath the chemically modified surface.

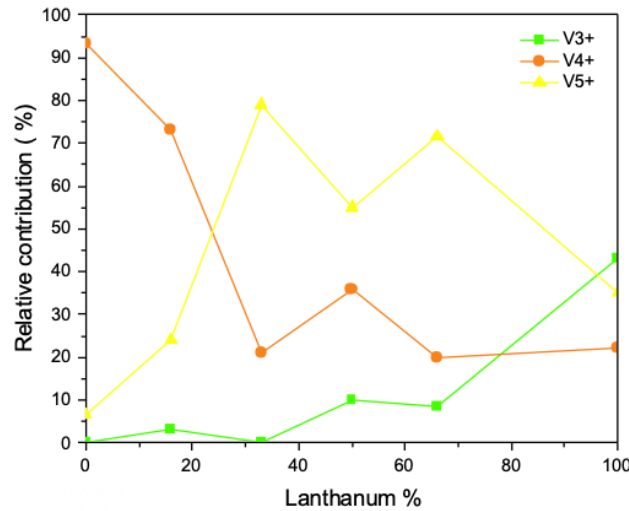


Figure 4.14: Relative contents of V<sup>3+</sup>, V<sup>4+</sup> and V<sup>5+</sup> oxidation state vs the La content.

## 4.2 (La,Sr)VO<sub>3</sub> as a transparent conducting oxide

After having established the high crystalline quality of the fabricated solid solution thin films and the effective charge doping, the focus is to establish the functional properties, i.e. the electrical transport properties and the optical properties, throughout the solid solution. The optimal doping content will be determined, as well as the influence of thin film form on the properties.

### 4.2.1 Electrical resistivity

The electrical resistivity of the LSVO solid solution thin films was measured between 10 and 300 K as presented in Figure 4.15 (a). The resistivity displays a high resistance that exceeds the measuring range of our present experimental set-up for compositions with a La content  $> 0.66$ . Therefore, it was not possible to measure the temperature dependence of the  $x = 0.83$  solid solution or the LaVO<sub>3</sub> parent compound thin film. In bulk material, a metal-insulator transition (MIT) is known to occur at  $x \approx 0.8$  (see chapter 2.4), which is consistent with the insulating behaviour of the La-rich films. For films with  $x \leq 0.5$ , a noticeable metallic temperature dependency of the resistivity is observed. The resistivity values for  $x = 0$  are discovered to be similar with those often seen in strontium Vanadate (SVO)

films on STO deposited by PLD [13, 109]. Moreover, these values resemble those of semiconducting n-type transparent conducting oxides (TCOs), including indium tin oxide (ITO) [77]. Also, the SVO films in question outperform other TCO materials such as fluorinated tin oxide (FTO) and antimony-doped tin oxide (ATO) in terms of resistivity values [118]. The electrical characteristics of the SVO film ( $x = 0$ ) significantly improve after being doped with lanthanum. Pure SVO's resistivity, which was measured at  $270 \mu\Omega\text{cm}$  at 300 K, significantly decreases to  $159 \mu\Omega\text{cm}$  for the composition with an  $x$  value of 0.5. This decrease in resistivity underlines how well lanthanum doping works to improve the material's electrical performance. The addition of lanthanum atoms likely modifies the electronic structure of the SVO lattice, changing the concentrations and mobility of charge carriers and eventually enhancing electrical properties.

Figure 4.15 (b) shows the evolution of resistivity for all conducting samples between room temperature and 10 K. It is crucial to note that the decrease in room temperature resistivity is followed by a noticeably greater decrease in the low temperature resistivity. This finding shows that variations in the La content may be causing changes in the transport mechanism. When  $x$  increases, the resistivity decreases at room temperature. This development may be due to the presence of more charge carriers, which raise the material's total electrical conductivity. The resis-

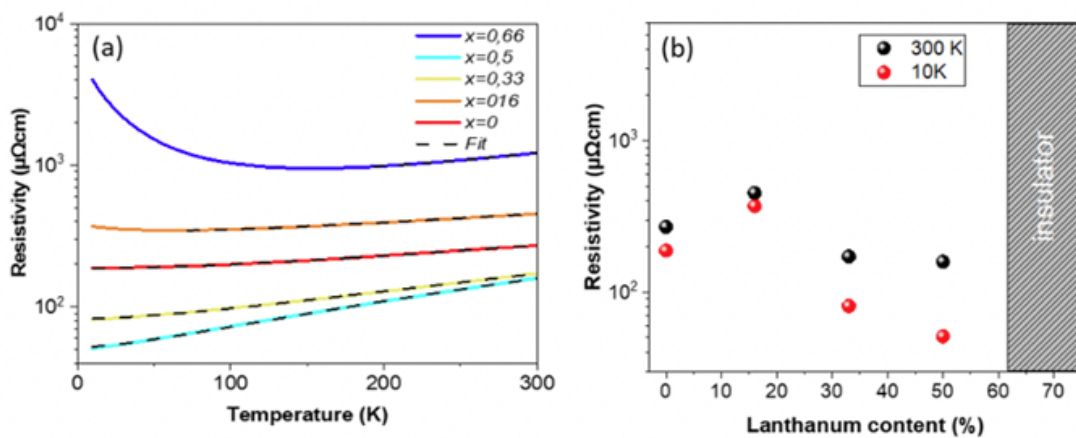


Figure 4.15: (a) Resistivity as a function of temperature of the LSVO solid solution thin films, and (b) evolution of resistivity with lanthanum content.

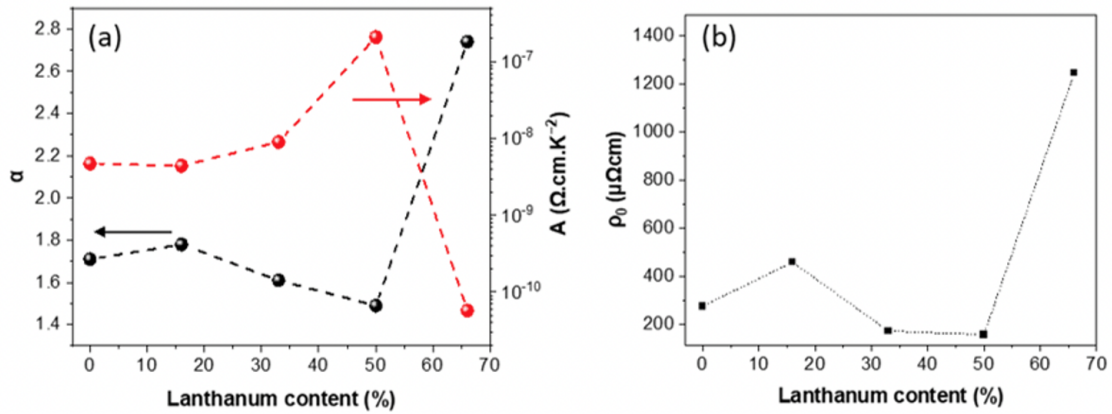


Figure 4.16: (a) The fit parameters  $\alpha$  (left axis) and  $A$  (right axis), and (b) the residual resistivity  $\rho_0$  as a function of the La content.

tivity of the samples continues to drastically decrease when the temperature drops to 10 K, suggesting that the low-temperature transport processes may be affected differently by the lanthanum doping. A number of causes, including a decrease in charge carrier scattering, modifications to the electronic band structure, or the formation of new transport channels, might explain the larger drop in low-temperature resistivity. Even more, the variation of the La content may lead to changes in the crystal lattice, which can change the dispersion of charge carriers and, as a consequence, have an impact on the material's low-temperature transport capabilities. Including lanthanum atoms into the lattice may also result in modifications to the electronic band structure, which might result in the opening or closure of certain electronic channels that affect the general transport behavior. In the following, we will investigate some of the properties of the charge carriers in order to identify the underlying mechanism of this decrease of the resistivity upon La doping.

In a correlated metal, the temperature dependence of resistivity can be expressed by the equation  $\rho(T) = \rho_0 + A \times T^\alpha$ , where  $\rho_0$  represents the residual resistivity at 0 K,  $A$  denotes the electronic interactions in a strongly correlated metal, and the exponent  $\alpha$  is a measure of the Fermi liquid nature of the material. This equation offers a helpful foundation for comprehending the electrical characteristics of correlated metals, such as LSVO. The evolution of the  $\alpha$  and  $A$  values as the lanthanum doping level varies is shown in Figure 4.16 (a). strontium Vanadate (SVO) in bulk

displays metallic behavior like a Fermi liquid, with a value of  $\alpha = 1.85$  and  $A$  values in the  $10^{-9}$  cm.K<sup>2</sup> range [119]. These numbers are quite consistent with our values. Considering the evolution of these parameters with lanthanum doping, the  $\alpha$  values range between 1.8 and 1.5, reaching a minimum for the  $x = 0.5$  film. At the same time, the  $A$  values dramatically rise and approach the  $10^{-7}$  range. This suggests that the  $x = 0.5$  film has stronger electronic correlations. Nonetheless, once the doping content exceeds 0.5, the value significantly rises while the  $A$  value sharply declines. The first reason is probably the small temperature range on which the metallic behaviour is observed, before changing to an insulating temperature dependence. The used model doesn't seem to apply for explaining the sample with  $x = 0.66$  temperature dependence. This shows that the thin film solid solution may have a smeared metal-insulator transition (MIT). The difference from the predicted behavior suggests that other variables or mechanisms, such as modifications to the electronic band structure, distortions of the lattice, or the impact of impurities on the material's electrical characteristics, may be the reason.

Figure 4.16 (b) presents the evolution of the residual resistivity at 0 K as a function of lanthanum doping. There are several variables that may affect the connection between residual resistivity and doping content, including the concentration of the dopant, the crystal structure, and the existence of impurities or defects in the material. In this specific case, the residual resistivity decreases as the lanthanum doping concentration increases, reaching a minimum value at a concentration of  $x = 0.5$ . This reduction in residual resistivity could be attributed to the improved electrical properties resulting from the introduction of additional charge carriers due to the lanthanum doping. On the other hand, a dramatic rise in residual resistivity is seen when the doping level exceeds  $x = 0.5$ . This rise is probably the result of impurities and defects brought on by the high lanthanum content in the crystal lattice. These defects and impurities may cause more charge carrier dispersion, which lowers the material's total electrical conductivity. In addition to the effects of impurities and defects, the metal-insulator transition (MIT) may also play a role in the observed increase in residual resistivity. As the lanthanum doping concentration increases beyond  $x = 0.5$ , the material may be approaching or undergoing the MIT, which could

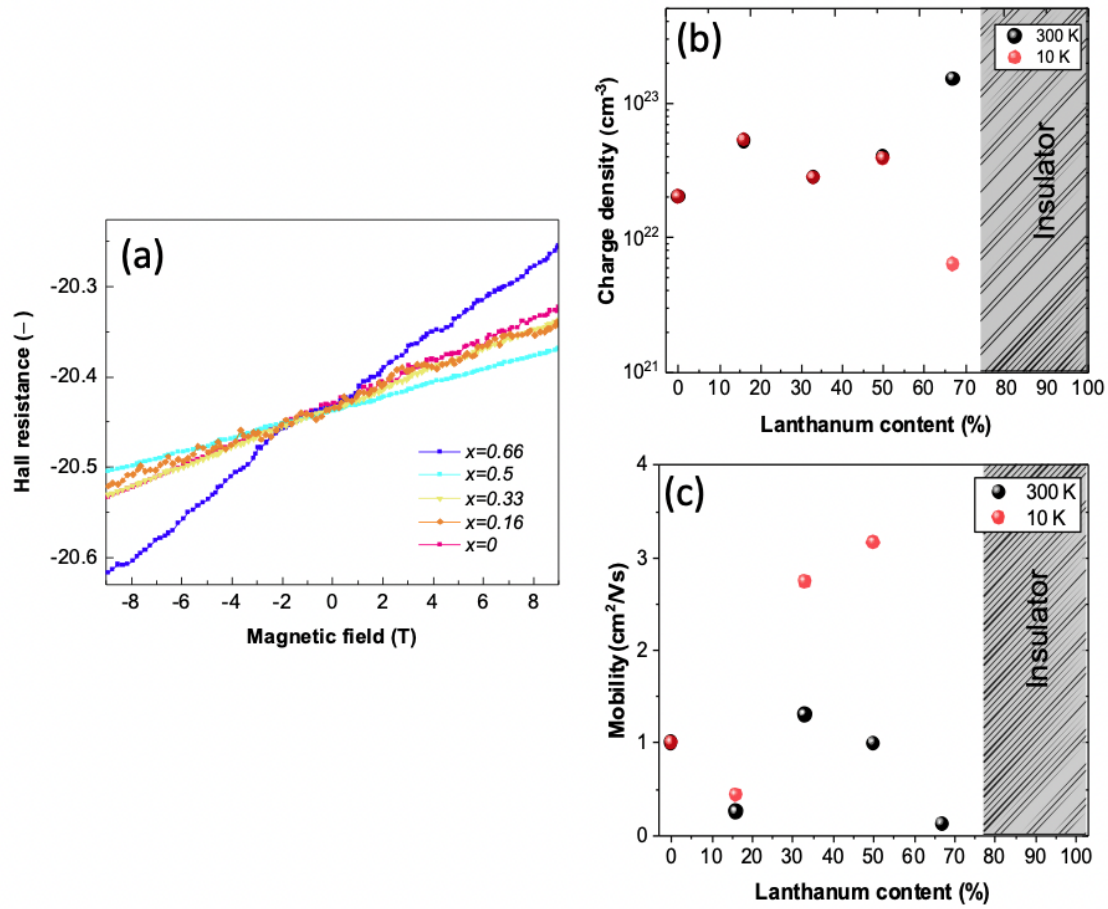


Figure 4.17: (a) Hall resistance as function of magnetic field of the LSVO solid solution films (b) Charge density  $n$  at 10K and 300K vs  $x$  (c) Carrier mobility at 10K and 300K vs  $x$ .

significantly alter the electrical properties of the material. The interplay between the impurities, defects, and MIT may collectively contribute to the substantial increase in residual resistivity observed for doping levels exceeding  $x = 0.5$ .

## 4.2.2 Hall effect

In order to gain a deeper understanding of the charge carrier type and charge density  $n$  in the LSVO solid solution, Hall effect measurements were conducted, as shown in Figure 4.17.

The  $\text{La}_{0.83}\text{Sr}_{0.17}\text{VO}_3$  solid solution and the pure LVO are not presented because of the high resistance of the samples. All curves show the same sign of the Hall effect,

including the pure SVO film, where the n-type conduction is well established [1]. An analysis of our measurement set-up and the respective current and field direction also confirm n-type charge carriers. Therefore, we do not observe p-type conduction as was reported for a thin film composition of  $x = 0.66$ , [12] which is clearly an n-type conductor in our study. It should be noted that in the reference [12], no comparative Hall measurements with either the known p-type semiconducting phase for La concentrations higher than 0.8 are shown, nor with the known n-type metallic phase with lower La concentrations. Also, a positive sign of the Seebeck coefficient indicated in the bulk study of La<sub>0.75</sub>Sr<sub>0.25</sub>O<sub>3</sub> [120] is complicated to interpret in the vicinity of the MIT and at high temperature, as shown by Uchida et al [121]. The Seebeck coefficient of compositions next to the MIT changes sign with temperature as a result of the crossover between the low energy and the high energy regime, and it is the sign of the Seebeck coefficient at low temperature indicating the carrier type. In this reference, the compositions around the MIT show a negative Seebeck coefficient at low temperature, confirming the here observed n-type conduction.

The slope, representative of the Hall constant, is rather similar for the samples with  $x \leq 0.5$ , and changes strongly for the  $x = 0.66$  film. Therefore, the  $x = 0.66$  film is on the verge of the MIT. Regarding more in detail the evolution for  $x \leq 0.5$ , the La doping leads to a small increase of the charge carrier density. For SVO and its 3d<sup>1</sup> vanadium configuration, a charge density of  $1.7 \times 10^{22} \text{ cm}^{-3}$  is expected. The here observed value is slightly smaller, indicating that only few oxygen vacancies are present in the film. When doping with La, a second 3d electron is introduced in the system, explaining the growing charge density when increasing  $x$ . The mobility shows a maximum for the  $x = 0.33$  sample. The mobilities are ranging between 1 and  $3 \text{ cm}^2/Vs$ , which is comparable to pure SVO thin films prepared by PLD [13,29].

### 4.2.3 Optical measurements

The electrical transport characterizations have shown that the LSCO solid solution thin films display a high charge carrier density. The opening of an optical transparency window in the visible range is, however, prevented by the tendency of charge carriers to absorb and reflect visible light. A high charge carrier density must be

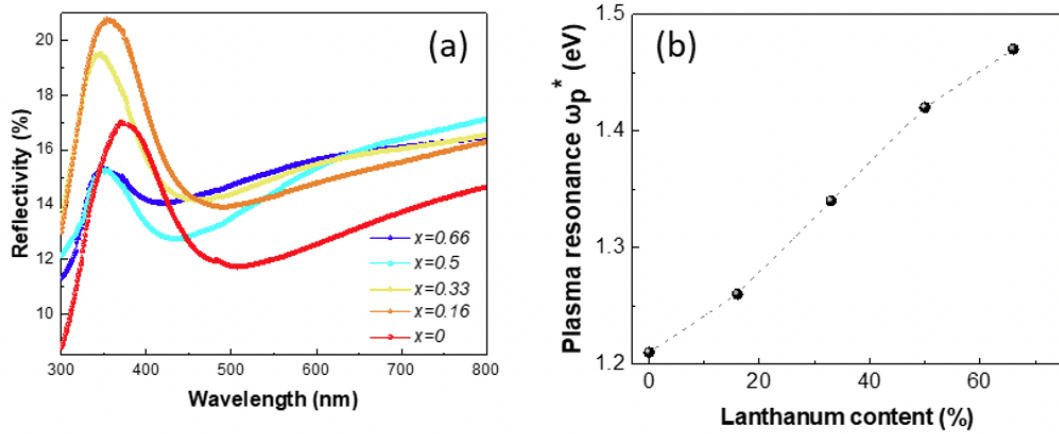


Figure 4.18: (a) Optical reflectivity of  $\text{La}_x\text{Sr}_{1-x}\text{VO}_3$  solid solution thin films, (b) the screened plasma frequency  $\omega_p^*$  versus La content.

maintained while minimizing photon absorption on one hand and shifting the reflection threshold towards the infrared region on the other hand in order to achieve TCO properties. Absorption takes place at high energy, whereas the light reflection threshold, which is determined by the screened plasma frequency  $\omega_p^*$ , is located at low energy (1.75 eV). This enables the visible domain optical transparency window to be opened.

In order to establish the optical reflection limit for the functional parameters, optical reflectivity measurements in the visible spectrum (350–850 nm) were conducted. These measurements were carried out by Sylvain Duprey of the CIMAP laboratory in Caen.) Due to the presence of silver paste on the back side of the samples, it was not possible to measure the optical transparency. However,  $\text{SrVO}_3$  films on  $\text{SrTiO}_3$  have typically a transmittance of above 80 % [13], indicating that solid solution thin films have comparable transmittance.

Figure 4.18 (a) shows how the resulting signal from the LSVO solid solutions may be split into two domains on each side of the wavelength (about 500 nm) where the reflectivity has a local minimum. A peak connected to an intra-band transition within the vanadium 3d orbitals is seen at low wavelengths. This transition results from the excitation of the energy levels in the O 2p, which increases reflectivity at shorter wavelengths. Yet, the reflectance increases towards high wavelengths when there are free charge carriers present. The lowest reflectivity in the wavelength

range between these two regions denotes the reflectivity minimum, sometimes referred to as the plasma edge. This minimum is linked to plasma resonance, which is a phenomenon that happens when a material's free charge carriers are activated by external radiation and evenly oscillate. The major indication of TCO transparency in the visible range is the plasma frequency  $\omega_p^*$ , which is a fingerprint of the transparency of TCOs in the visible range. This latter is related to the unscreened one by the following formula  $\omega_p^* = \omega_p / \sqrt{\epsilon_r}$ , where  $\epsilon_r$  is the relative permittivity of SVO. According to previous studies on SVO,  $\epsilon_r$  is determined from the real part of the dielectric function at the energy where the optical interband first occurs [122]. As shown in Figure 4.18(b), the value of  $\omega_p^*$  was obtained by using the relative permittivity value ( $\epsilon_r = 4$ ) [13].  $\omega_p^*$  varies linearly with the La content, increasing up to a value of 1.5 eV for  $x = 0.67$ . The obtained values are coherent with the reference range of SVO, which is reported to be between 1.3 and 1.4 eV. [122] However, all values stay below 1.75 eV, and indicate therefore optically transparent materials. The linear increase of  $\omega_p^*$  with  $x$  shows that the minimum reflection should move towards the visible range compared to pure SVO.

#### 4.2.4 The effect of La doping on electronic correlations

The above-shown results allow for a more detailed analysis of the role of the La doping in terms of electronic correlations and the interaction with the strain. The screened plasma frequency as presented in the general introduction can be expressed as

$$\omega_p^* = \frac{e}{\epsilon_0 \epsilon_R} \sqrt{\frac{n}{m^*}} \quad (4.1)$$

where  $e$  is the electronic charge,  $\epsilon_0$  and  $\epsilon_R$  the vacuum and the relative dielectric constant, respectively. With the measurement of  $\omega_p^*$  and  $n$ , the effective mass  $m^*$  can be calculated, when the  $\epsilon_R$  is known. For SrVO<sub>3</sub>, the commonly used value is 4 [122], and for LaVO<sub>3</sub>  $\epsilon_R = 5$  was used [28]. These values are estimations, and the evolution of  $\epsilon_R$  in the solid solution is not determined. Therefore, for simplicity, we have used  $\epsilon_R = 4$  as an estimation for the whole solid solution.

With the above measured values of  $\omega_p^*$  (Figure 4.18 (b)) for the whole solid

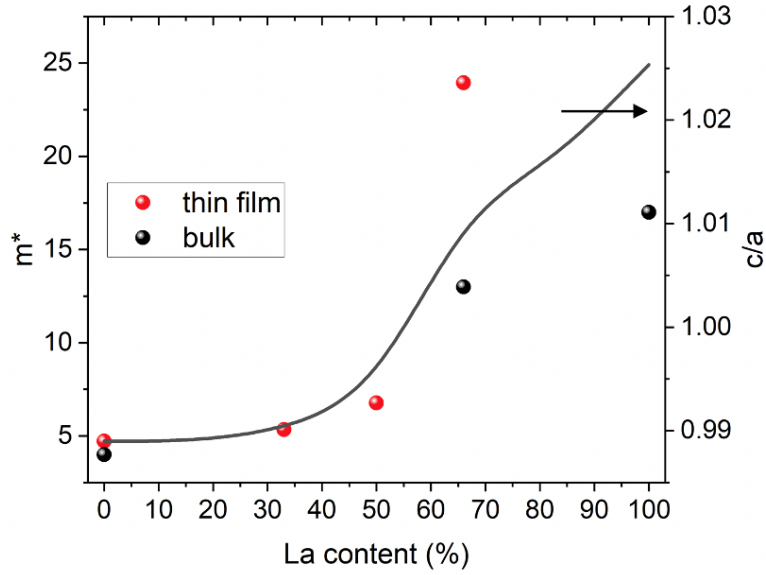


Figure 4.19: Evolution of the effective mass (left axis) of the charge carriers in (La,Sr)VO<sub>3</sub> as a function of the La content in the thin films (red symbols) and in bulk (black symbols, data taken from [27], [28] and [29]). The solid line represents the tetragonal distortion  $c/a$  (right axis) of the solid solution thin films.

solution and  $n$  for the conducting samples (Figure 4.17 (b)), the evolution of  $m^*$  along the solid solution has been calculated for the thin films, as shown in Figure 4.19. The value of the pure SrVO<sub>3</sub> film coincides well with what was determined in other studies on thin films [29]. It is interesting to note that  $m^*$  increases only slightly up to a La content of 50 %, while the film with 66 % shows a strong increase to about 25. The same La content in bulk samples shows a lower  $m^*$  value of about 13 [28], and even pure LaVO<sub>3</sub> has a lower value of about 17 [27]. The enhancement of  $m^*$  with La content in the bulk solid solution is related to the increasing orthorhombic lattice distortions by octahedral rotations and therefore enhanced electronic correlations. When comparing to the observed macroscopic lattice distortion related to the substrate misfit (Figure 4.19, right axis), it becomes evident that the strong increase of  $m^*$  takes place when the films go over from a tensile strain indicated by the  $c/a$  value  $\leq 1$  to a compressive strain ( $c/a \geq 1$ ).

Thus, the strain modified crystalline structure may play a governing role: for films under tensile strain, octahedral rotations are suppressed, as they tend to reduce the V-O-V in-plane distance. In this range for a La content below or equal to 50%,

the La dopants enhance the charge density in the system, but the bulk octahedral rotations are blocked by the tensile strain state. This may be an explanation of the observed decrease of the resistivity and the optimal value of the 50 % La film. In the bulk solid solution, the enhancement of the charge density is accompanied by lattice distortions and stronger electronic correlations, compensating the effect on the resistivity. On the other hand, when the strain state of the film goes over to compressive at La contents above 50%, the introduction of octahedral rotations is a very efficient way to compensate the compressive strain. Thus, octahedral rotations will be rather enhanced compared to the bulk material, leading to an enhanced effective mass. This would also indicate that the Metal-Insulator-Transition may occur at lower La contents in compressively strained films, which would have to be confirmed by smaller doping steps in these thin films.

## 4.3 Strain engineering

As shown in the previous section, a method that is promising for modifying the characteristics of transparent conducting oxide perovskite thin films is strain engineering. It can largely modify the electrical and optical properties of these materials by varying the strain, which opens up new opportunities for improvements and applications. We will go into detail about how strain engineering affects the characteristics of lanthanum strontium Vanadate (LSVO) thin films in this section.

### 4.3.1 Structural and chemical characterization

We have deposited the solid solution set of LSVO thin films on (001) - oriented lanthanum strontium Aluminium Titanate (LSAT) substrates in order to investigate the behavior of these thin films and compare their properties. This investigation seeks to make comparisons with the solid solutions that have been previously deposited on STO (001) substrates. As compared to STO (3.905Å), the lattice parameter of LSAT (3.868 Å) is smaller, leading to a compressive strain on a large part of the solid solution. The calibration for the deposition process was performed in the same way as in the preceding studies with STO substrates to guarantee a fair comparison. We strive to reduce disparities that may result from variations in deposition parameters. This strategy will provide a more precise and thorough knowledge of the behavior of the LSVO thin films by allowing us to concentrate on their fundamental characteristics on the two different substrates. It is worth noting that the deposition rate were similar to the calibration of LSVO on STO substrate.

The Figure 4.20 (a) represent the  $\theta-2\theta$  diffractograms for LSVO thin films grown on LSAT substrate, captured using XRD. The diffractograms target the region close to the (002) Bragg peak particularly. The (002) reflection corresponding to the LSAT substrate is clearly visible at a position close to 47 °. For the LSVO thin films, the peak associated with the (002) reflection with positions ranging from 45.4 ° to 47.35 °. This range in peak positions can be attributed to the differences in the lanthanum composition within the individual films. The Laue fringes in the thin films deposited on LSAT show high intensity, especially at higher La doping levels,

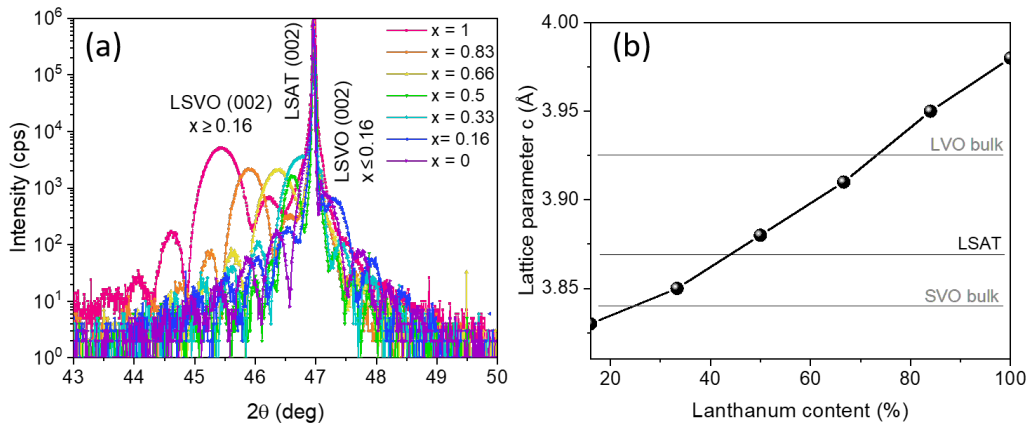


Figure 4.20: (a)  $\theta-2\theta$  scan of the (002) reflection of the LSAT and the  $\text{La}_x\text{Sr}_{1-x}\text{VO}_3$  solid solution thin films, (b) Out-of-plane lattice parameter evolution with the La content.

as compared to those deposited on STO substrates (Figure 4.2). The shift in the thin film's Bragg peak as a result of the amount of lanthanum inserted into the film is highlighted. According to this finding, solid solutions of different compositions are effectively formed in the thin films, demonstrating that the growth of different solid solution was successful and that lanthanum was effectively incorporated in the film structure. The out-of-lattice parameter evolution with the lanthanum content is following perfectly the law of Vegard, as it is linear (4.20 (b)).

Using XPS, we sought to elucidate the elemental composition and chemical environment of lanthanum strontium Vanadate (LSVO) solid solutions on the LSAT substrate. Recognizing the necessity of a comparative analysis, we again measured both water treated and untreated sample surfaces. Through a comprehensive analysis of the core level peaks corresponding to the samples before and after exposure to water, we were able to estimate the composition concerning the La/Sr ratio, as depicted in Figure 4.21. At  $x = 0.83$  for LSVO deposited on LSAT, a notable variation was observed, both concerning the nominal La/Sr ratio, as well as concerning the difference before and after the water treatment. This deviation may be related to the more strongly insulating character of the sample, with  $x$  being above the metal-insulator threshold. However, our data revealed no discernible compositional differences for the other solid solution sets grown on STO and LSAT. In addition,

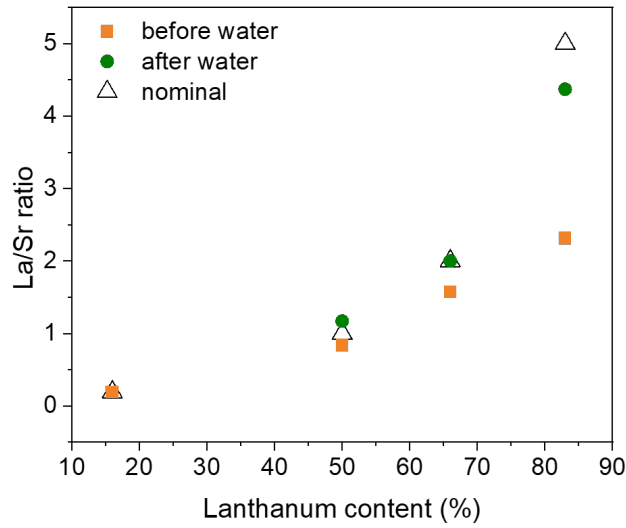


Figure 4.21: Experimental composition extracted from XPS before and after water treatment versus the nominal composition for LSVO solid solution films grown on LSAT (001).

the calibration procedure utilized in our study exhibited remarkable accuracy, with the experimental composition closely matching the predicted nominal composition.

We carried out an in-depth investigation of the Sr 3d core levels for a total of four distinct compositions of LSVO that had been deposited on LSAT substrates. Figure 4.22 is a representation of the fitting that was carried out on the Sr 3d core levels, same as previous analysis on LSVO deposited on STO, each correlates to a distinct chemical environment, which helps to shed light on the interactions and bonds that are present in the LSVO.

For all the measured samples, two Sr contributions related to two different chemical environments are observed. Based on a thorough analysis of the Sr 3d core level in  $\text{SrVO}_3$  [108], these two contributions can be ascribed to a contribution related of the Sr atoms being integrated into the perovskite lattice (Sr lattice) and to a contribution of Sr atoms being located at the surface of the samples, with a distinct chemical environment related to Sr-O-H bonds. This latter contribution is observed in the case of a chemical modification of the surface. Disregarding the  $x = 0.16$  sample for the moment, it can be observed that the Sr lattice contribution increases from  $x \geq 0.33$  (Figure 4.24). Therefore, the more La is doped into the system, the

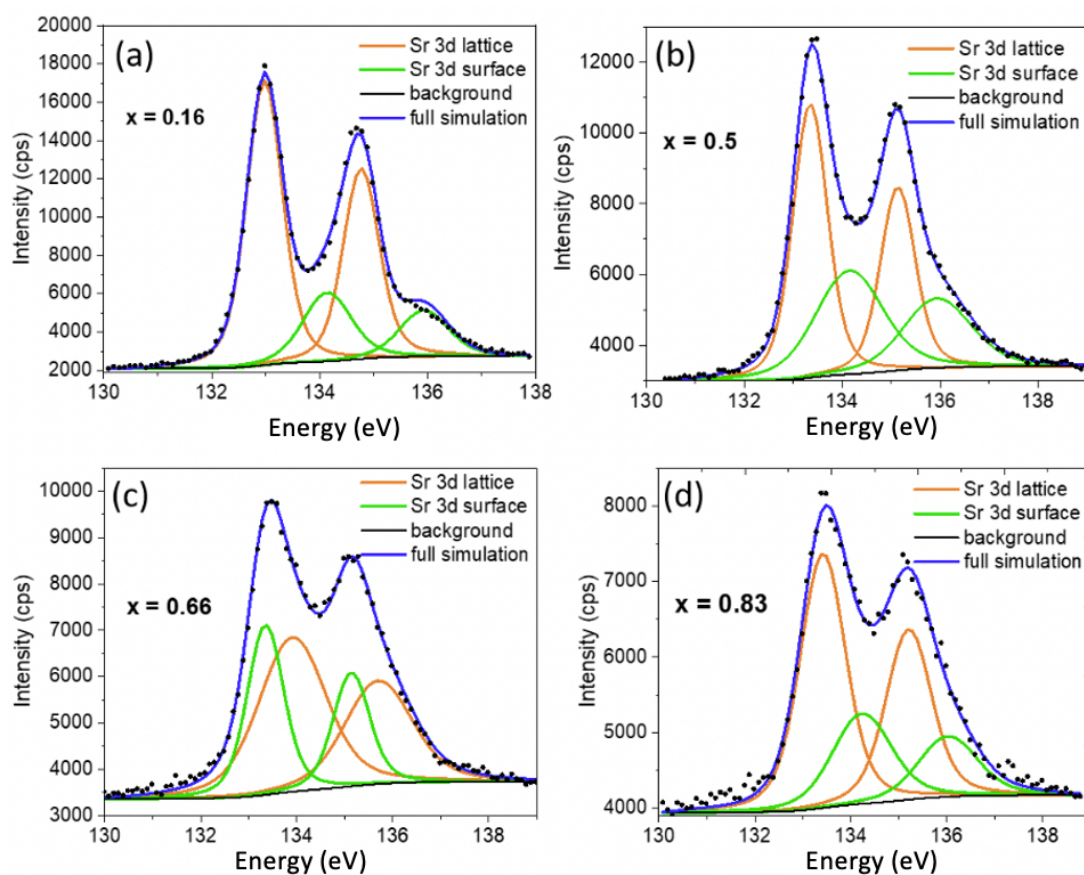


Figure 4.22: XPS Sr 3d core level spectra (black circles) of LSVO solid solution films grown on LSAT (001) with fit: Sr lattice contribution (orange line), Sr surface contribution (green line) and the full simulation (blue line).

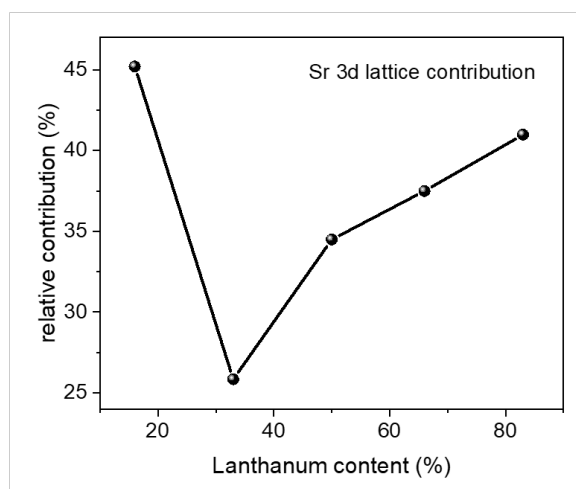


Figure 4.23: Relative contribution of the XPS Sr 3d lattice signal as a function of the La content.

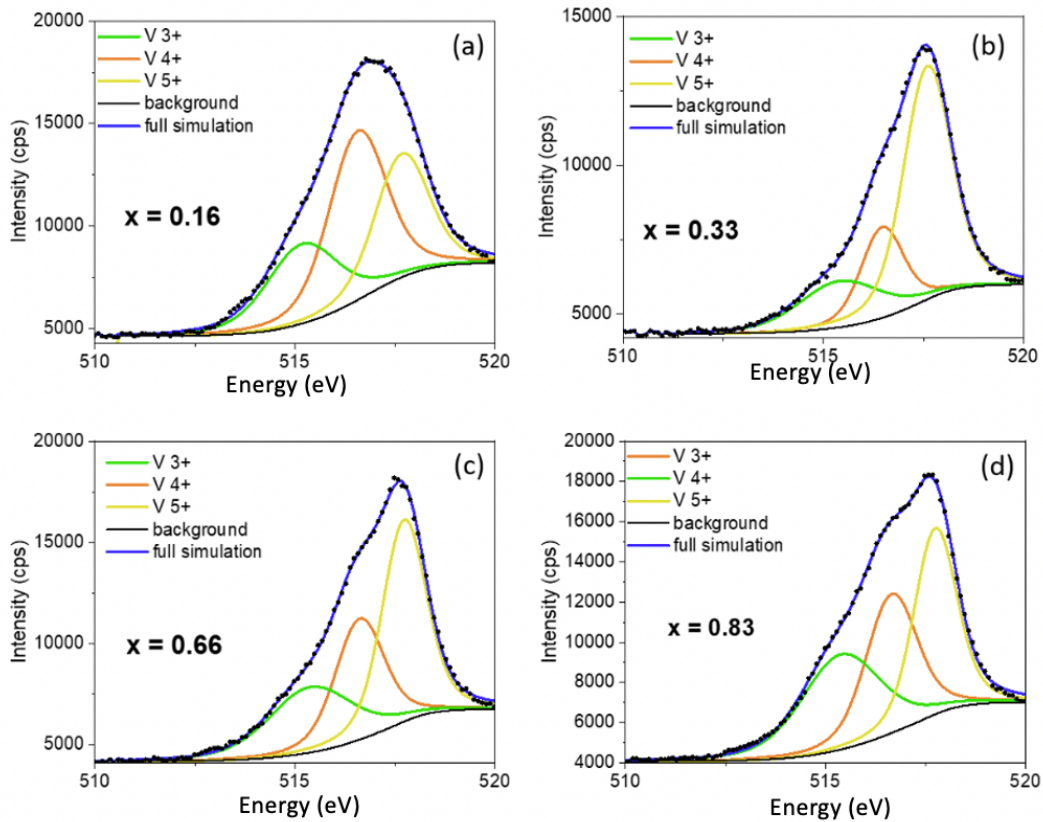


Figure 4.24: XPS V 2p3 core level spectra (black circles) with fit:  $V^{3+}$  contribution (green line),  $V^{4+}$  contribution (yellow line),  $V^{5+}$  contribution (green line), and the full simulation (blue line).

surface contamination seems to decrease. The high contribution of the Sr lattice signal in the  $x = 0.16$  sample seems to contradict this conclusion, but the fact that these measurements were done after the water treatment, an influence of the La content on the effect of the water treatment cannot be excluded.

We applied the same approach to the V 2p3 core levels so that we could gain a more in-depth knowledge of the chemical complexity that exists within the LSVO samples. vanadium, which is similar to strontium, was also found to coexist in a variety of chemical environments or oxidation states in the LSVO samples (Figure 4.24). A similar evolution than for the Sr core level is observed: the  $x = 0.16$  sample is out of the overall evolution, but when regarding from  $x \geq 0.33$ , the  $V^{5+}$  contribution reduces, which should be present only in the chemically modified surface. Therefore, La doping helps to avoid at least partly the surface overoxidization. The

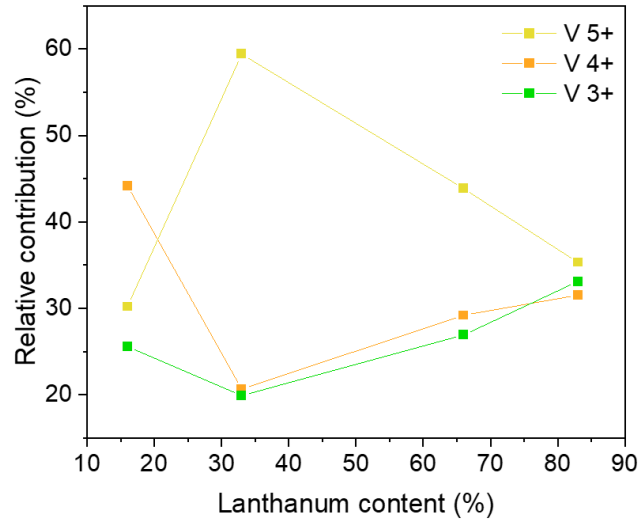


Figure 4.25: Relative contribution of the different V oxidation states to the XPS V 2p3 core level as a function of the La content of LSVO/LSAT.

V<sup>4+</sup> contribution increases, as expected in this case. The concomitant increase of the V<sup>3+</sup> indicates an effective charge doping of the V ions. Again, the  $x = 0.16$  sample is out of the overall evolution, by showing a large V<sup>4+</sup> contribution, while the V<sup>5+</sup> contribution is relatively small, which would be expected on a surface with an efficient water cleaning. However, the V<sup>3+</sup> contribution is quite important, and especially larger than for the  $x = 0.33$  sample.

We were able to identify and quantify the various oxidation states of vanadium that were present in the samples thanks to a thorough examination of the V 2p3 core levels. This provided insights into the electrical structure as well as the role that vanadium plays in the overall material. The fact that each component of the fit corresponds to a different chemical state or local bonding environment of the vanadium atoms highlights the interplay that exists between the many oxidation states and the impact that these states have on the properties of the material. Overall, we notice that the V<sup>5+</sup> decreases with the lanthanum doping, while the V<sup>4+</sup> and V<sup>3+</sup> increases, with the exception of the  $x = 0.16$  composition.

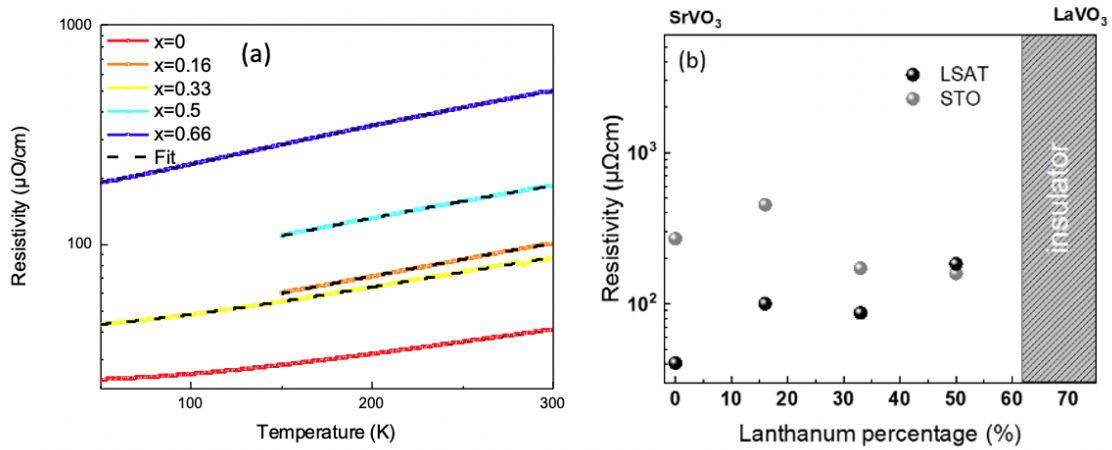


Figure 4.26: Resistivity as a function of temperature of the LSVO solid solution thin films on LSAT.

### 4.3.2 Analysis of the functional TCO properties

The Figure 4.26 presents the evolution of resistivity in conducting samples of lanthanum strontium vanadium oxide (LSVO) as a function of the temperature. The results provided two significant insights into the influence of strain on the electrical characteristics of LSVO. The samples deposited on LSAT demonstrates a significant decrease in resistivity in comparison to those deposited on STO, a clear evidence supporting the positive impact of compressive strain on the enhancement of electrical properties in the LSVO solid solution. Interestingly, the investigation also reveals a notable disparity between the two systems. In contrast to the samples deposited on STO, the solid solution deposited on LSAT does not exhibit any electrical enhancement in doping. This observation supports the explanation of the enhancement observed in the samples deposited on STO with the doping content, due to the 2 regimes of the evolution of the out of plan lattice parameter.

Same as the procedure done in the LSVO grown on STO, Figure 4.27(a) presents the variation of  $A$  and  $\alpha$  with the lanthanum content, and Figure 4.27 (b) shows the  $\rho_0$  variation as well, of the LSVO samples deposited on LSAT. The variation of  $A$  is showing an increase with the lanthanum doping, which clearly points at the fact that the correlation decreases. At the same time,  $\alpha$  is showing a quite complex variation, but a general decreasing tendency with the lanthanum doping can be

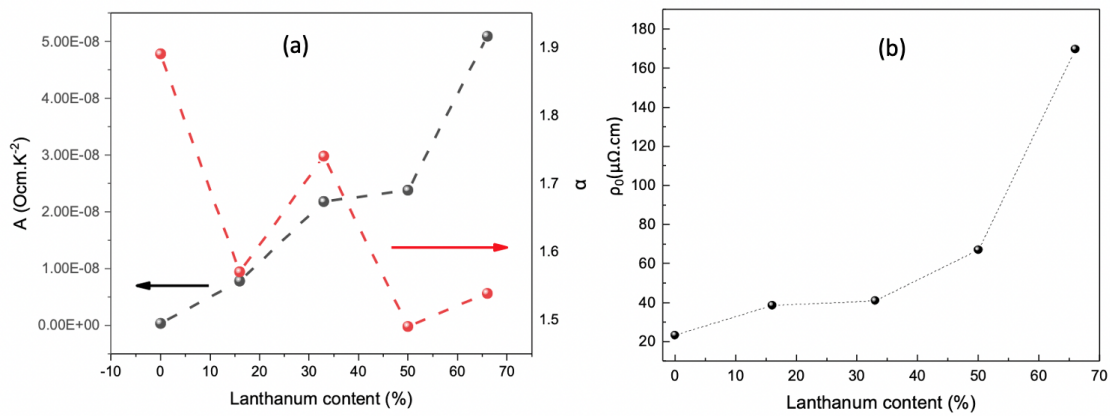


Figure 4.27: (a) The fit parameters  $\alpha$  (right axis) and  $A$  (left axis), and (b) the residual resistivity  $\rho_0$  as a function of the La content.

observed. The scattering of the  $\alpha$  values is probably related to the fact that the resistivity measurements of the samples  $x = 0.5$  and  $x = 0.16$  were not extended to the same lower range of temperature. This taken into consideration, we can deduce that the general tendency of  $\alpha$  is decreasing with the lanthanum doping. On the other hand, we notice clearly that the lanthanum doping is increasing the charge scattering within the samples as shown by the increase of the  $\rho_0$  values in Figure 4.27 (b).

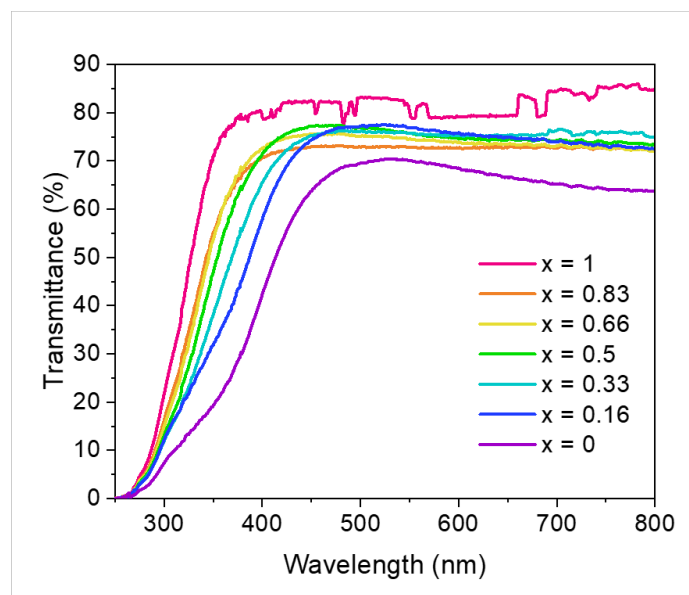


Figure 4.28: Optical transparency of the solid solution thin films as a function of wavelength.

The optical transparency measurements of LSVO solid solution samples deposited on an LSAT substrate are depicted in Figure 4.28. From an optical perspective, there is no significant difference in transparency observed among the solid solution. However, a notable distinction becomes apparent when comparing them to the LSVO samples that have been deposited on STO. This suggests that the strain has decreased the bandgap, allowing the samples to absorb in higher energy photons range, which leads to a transparency in lower wavelengths. Also strain alters the spacing between atoms, which in turn affects electronic energy levels and band alignments. This fact highlights the significant impact of compressive strain on optical measurements, resulting in the formation of a transparency region at shorter wavelengths. The results indicate that strain engineering has the ability to exert precise control over optical properties. This enables the fine-tuning and potential optimization of transparency characteristics within specific wavelength ranges.

## 4.4 Interaction of the (La,Sr)VO<sub>3</sub> surface with different atmosphere

As mentioned in section 3.1.4, the SVO surface is known to be altered in ambient atmosphere due to overoxidation, with a possibility to etch this chemically modified surface with liquid water. We have carried out in-depth studies on the pure SVO surface [19], using an operando cell available at the APE-HE beamline. In the framework of this study, we have also carried out operando measurements on the surface of the LSVO solid solution, in order to study the influence of the La doping. As the surface instability of SVO is related to its unstable V<sup>4+</sup> oxidation state, the substitution with La leading to a gradual change to V<sup>3+</sup> may stabilize the film surface. Therefore, we have carried out XAS studies on the solid solution thin films under He as a slightly reducing atmosphere especially at elevated temperatures, and under O<sub>2</sub> as an oxidizing atmosphere, accelerating the mechanisms also possible under ambient atmosphere.

Using X-ray absorption spectroscopy (XAS), we give a thorough analysis of the L2 and L3 vanadium absorption edges. The primary objective is to examine how exposure to helium and oxygen gas affects the electrical structure and local atomic

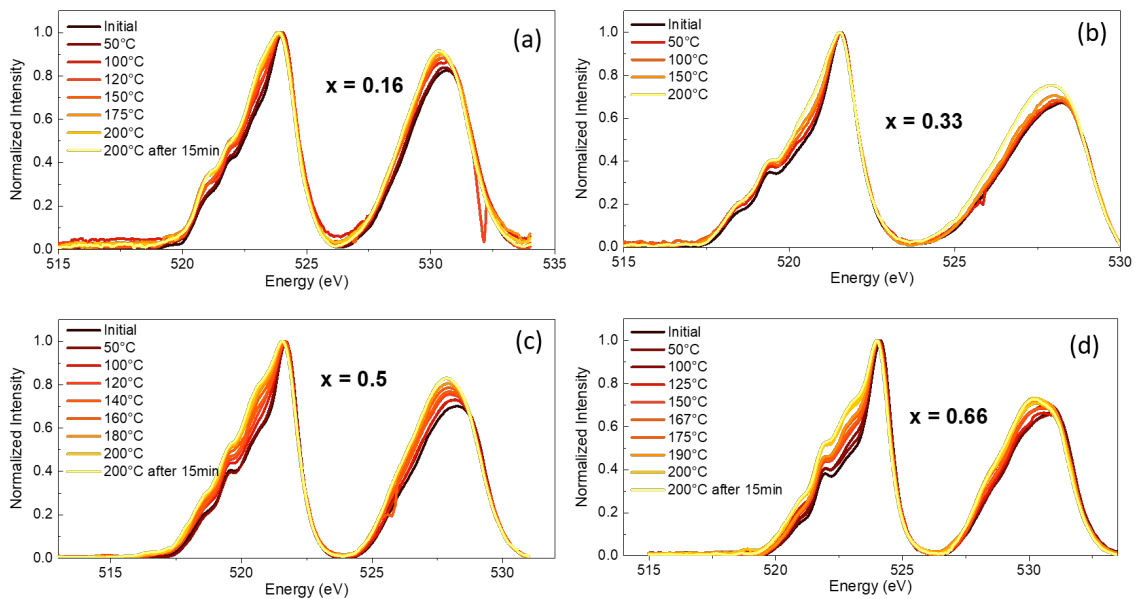


Figure 4.29: XAS vanadium L2 and L3 edges spectra with helium induced reduction for (a) 0.16 (b) 0.33 (c) 0.5 (d) 0.66.

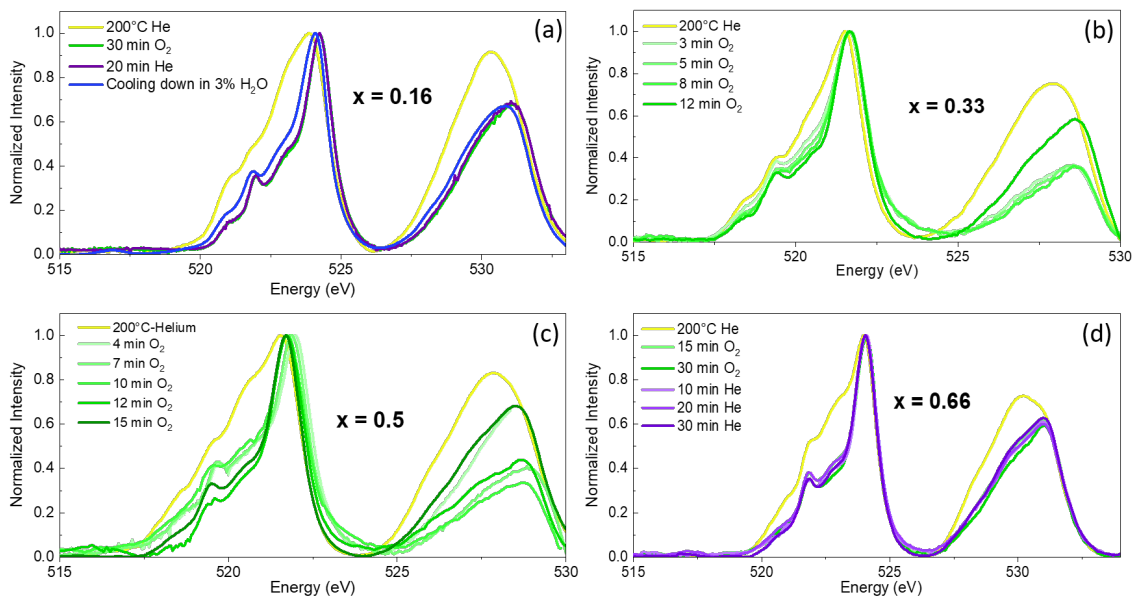


Figure 4.30: XAS vanadium L2 and L3 edges spectra under different atmospheres (oxygen green lines, He violet lines and H<sub>2</sub>O vapor blue line) for (a) 0.16 (b) 0.33 (c) 0.5 (d) 0.66.

environment of vanadium. It is possible to learn essential information about the helium-reduction and oxidation of vanadium in-situ and how it affects the material and its surface. After the exploration phase, we have developed a protocol consisting of the following steps: treatment of the sample with 1 min liquid water prior to introduction into the chamber (dissolution of the naturally aged, modified overoxidized surface), heating the sample to 200°C under a helium atmosphere (reducing atmosphere), and then oxidizing under oxygen gas at varying pressures at this temperature.

The XAS spectra of the vanadium L2 and L3 edges for compositions  $x = 0.16$ , 0.33, 0.5, and 0.66 are presented in Figure 4.29. The helium-induced reduction of V<sup>5+</sup> to V<sup>4+</sup>, caused by extended exposure to helium gas, is a notable observation from these spectra. Even without a full quantitative analysis, the change of the pre-edge region of the L3 edge is the signature of these changes. Furthermore, the degree of this reduction reaction varies among the samples, suggesting that the amount of lanthanum doping present in the thin films affects how sensitive the samples are to helium-induced reduction (Figure 4.31). It becomes clear from a closer look at the data that higher lanthanum doping concentrations result in thin films that are

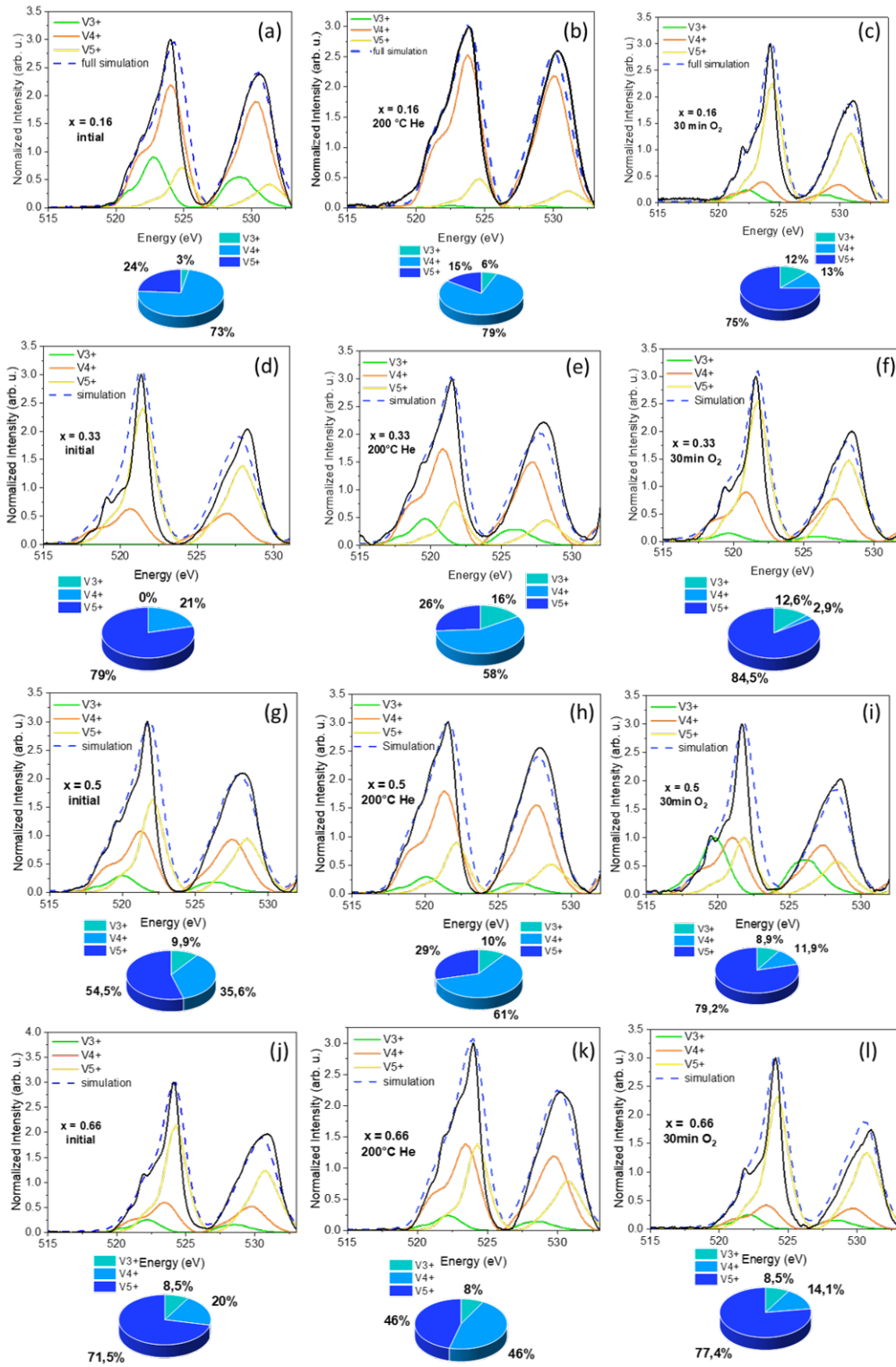


Figure 4.31: vanadium L2 and L3 edges spectra simulated for different  $x$  with V<sup>3+</sup>, V<sup>4+</sup>, and V<sup>5+</sup> references: Initial distribution (first column), after helium reduction (second column), and after oxygen exposure (third column).

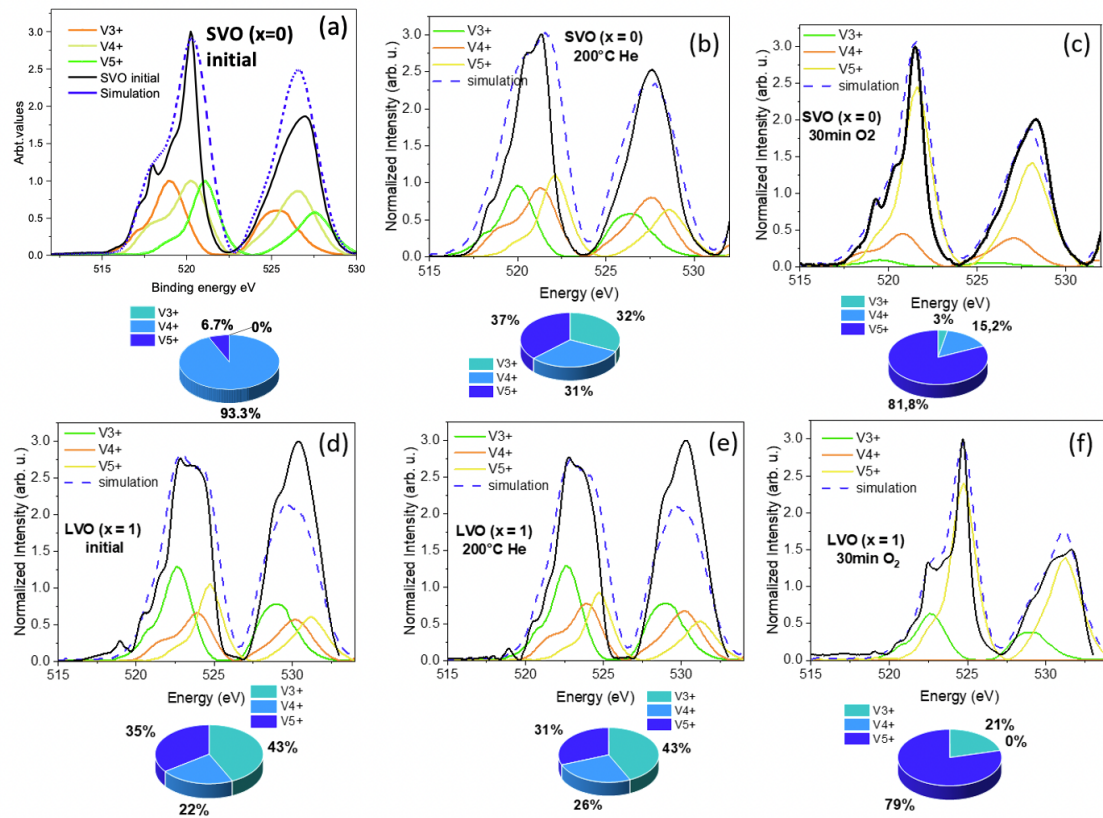


Figure 4.32: vanadium L2 and L3 edges spectra simulated of the SVO ( $x = 0$ ) and LVO ( $x = 1$ ) thin film with V<sup>3+</sup>, V<sup>4+</sup>, and V<sup>5+</sup> reference: Initial distribution (first column), after helium reduction (second column), and after oxygen exposure (third column)

more sensitive to helium-induced reduction. This finding implies that the reaction of the material to exposure to helium is directly related to the inclusion of lanthanum inside the LSVO lattice. Due to the presence of lanthanum, the local atomic and electronic environment close to vanadium has changed, which has an impact on the reaction kinetics and thermodynamics of the reduction process.

For the same set of LSVO solid solution thin films ( $x = 0.16, 0.33, 0.5,$  and  $0.66$ ) as in Figure 4.29, Figure 4.30 shows the XAS spectra after exposure to oxygen gas. The re-oxidation of V<sup>4+</sup> back to V<sup>5+</sup> during the exposure to the oxygen environment is a notable observation in this circumstance. However, in contrast to the helium-induced reduction behavior seen in Figure 4.29, the susceptibility of the thin films to this re-oxidation process appears to be more or less consistent across all doping levels of lanthanum. The re-oxidation kinetics of V<sup>4+</sup> to V<sup>5+</sup> during oxygen gas exposure

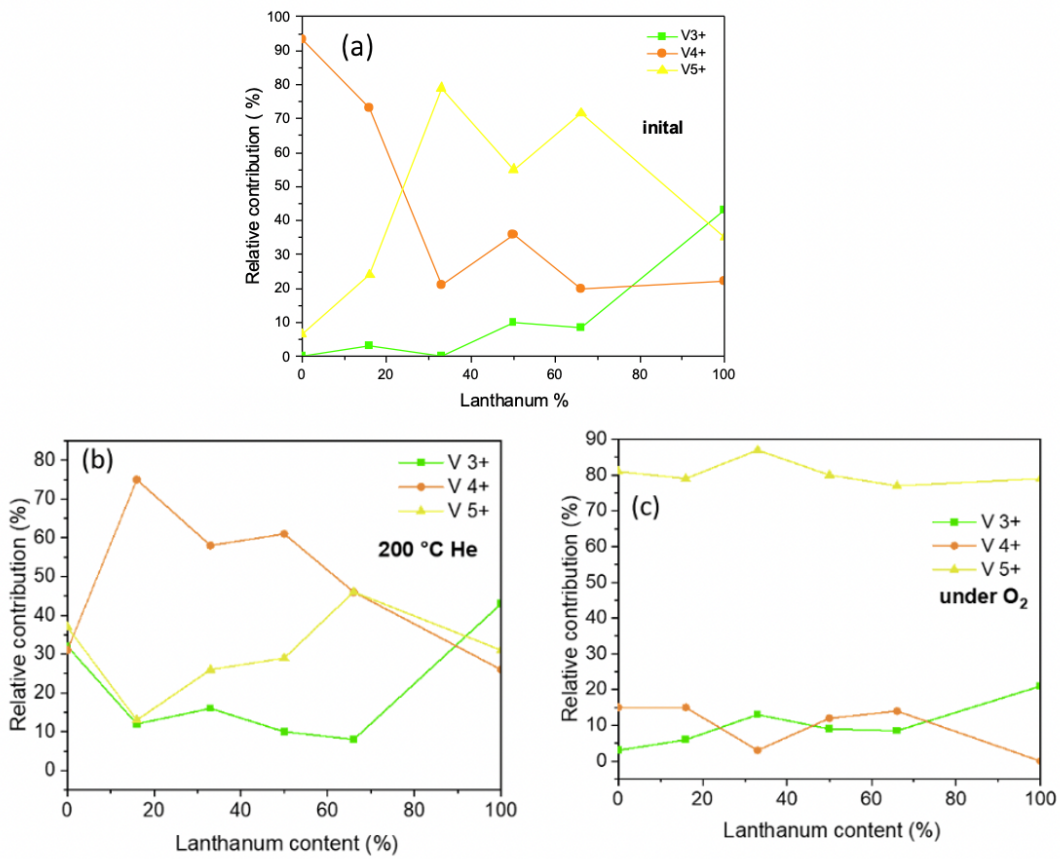


Figure 4.33: Summary of the V<sup>3+</sup>, V<sup>4+</sup> and V<sup>5+</sup> variation with lanthanum doping: (a) Initial distribution, (b) after helium reduction, and (c) after oxygen exposure.

appears to be independent of the lanthanum doping concentration, according to a thorough examination of the XAS spectra. This finding may be explained by the fact that the re-oxidation process is dominated by the intrinsic chemical affinity of vanadium for oxygen, which exceed any possible effects brought on by the presence of lanthanum in the thin films. This emphasizes the relationship between the chemical environment and the lanthanum concentration in vanadium-based materials, which ultimately affects the materials' sensitivity to various gaseous atmospheres.

We aimed to conduct a quantitative analysis of the oxidation states of vanadium in different thin films doped with lanthanum, in accordance with the observations presented in the Figures 4.29 and 4.30, indicating the sensitivity of vanadium oxidation states to various gaseous environments and lanthanum doping levels. In order to do this, we used a fitting methodology to deconvolute the vanadium L2 and L3

edges in the XAS spectra by taking into account the unique contributions of the V<sup>3+</sup>, V<sup>4+</sup> and V<sup>5+</sup> oxidation states, as presented in Figure 4.33 for the different atmospheres. The data of the initial state is the same as shown in Figures 4.13, and was discussed there.

Under He reduction (Figure 4.33 (b)), we see that the evolution of the V<sup>3+</sup> and V<sup>5+</sup> is increasing with the lanthanum doping content, while V<sup>4+</sup> is decreasing. This suggests that the lanthanum doping is favoring the 3+ and 5+ oxidation states over the 4+ on the reduction under helium. It is important to acknowledge that the fitting results should not be considered as absolute, and the observed tendencies might not be precise. Nevertheless, the objective is to correlate an overall trend in the relationship between the doping content and the behavior of the thin film samples under various atmospheric conditions in the X-ray Absorption Spectroscopy.

As observed before, the development of the vanadium oxidation states appears to be quite stable across the various lanthanum doping levels for the oxygen exposure (Figure 4.33 (c)). The re-oxidation of V<sup>4+</sup> to V<sup>5+</sup> in the presence of oxygen gas is therefore suggested to be less susceptible to the lanthanum doping. Any possible impacts brought on by the lanthanum dopants inside the thin films may be overshadowed by the intrinsic chemical affinity of vanadium for oxygen, which is thought to be playing a more substantial role in the re-oxidation process.



## CHAPTER 5

---

### (La, Sr)CrO<sub>3</sub> solid solution thin films

---

In this chapter, a full analysis of the complexities of lanthanum strontium chromium oxide (LSCO) thin films is conducted, concentrating on the impact of doping on the material's characteristics and the ensuing consequences on the functional properties. The investigation is focused on five different compositions of the solid solution with different lanthanum doping. These compositions are indicated as La<sub>1-x</sub>Sr<sub>x</sub>CrO<sub>3</sub>, with  $x$  ranging from 0 to 1 ( $x = 0, 0.16, 0.33, 0.5, 0.66, 0.83, \text{ and } 1$ ). Because the doping levels were changed in a methodical manner, it was possible to evaluate the effect of the lanthanum concentration on the properties of the material and highlight any possible correlations. As a first step in our study, a comprehensive structural evaluation of the LSCO thin films was carried out. During this process, important factors such as thickness, lattice parameters and structural phases was evaluated. These aspects should illuminate the relationship between LSCO thin film doping levels and structural integrity. Next, the surface chemistry of the thin films were characterized by using X-ray Photoelectron Spectroscopy (XPS). This gave us the opportunity to evaluate the accuracy of our calibration technique and provided insights on the oxidation states of the constituent elements. An analysis of the spectra of the core level of the constituent elements can provide crucial insights into

the chemical bonding and electronic structure of a material. These factors, in turn, have a significant impact on the functional qualities of the material. In addition, X-ray Absorption Spectroscopy (XAS) measurements was carried out on selected compositions of the solid solution set. These measurements provided us with important insights into the local atomic structure. Measurements using both XPS and XAS can be combined for a more comprehensive knowledge of the chemistry of the material and how it is affected by the different concentrations of dopants. In addition, the electrical and optical characteristics of the LSCO thin films was evaluated, looking into the effect that lanthanum doping had on the possible applications of the materials as transparent conducting oxides (TCOs). In the end, the solid solution set was developed on a variety of substrates, such as LaAlO<sub>3</sub> (001), LSAT (001) and fluorine-doped SnO<sub>2</sub> on glass, so that we could assess how the strain engineering affected the characteristics of the LSCO thin films and study the role that substrate-induced strain plays in regulating the material's performance.

## 5.1 Growth of the solid solution thin films

The development of the LSCO solid solution has been investigated, gaining inspiration from the established findings on the growth of LSVO. The use of a STO (001) substrate was implemented to reduce the impact of strain-induced interference and focus exclusively on the impact of doping concentration in the LSCO material. In the same manner as the development of LSVO, the parent compounds  $\text{SrCrO}_3$  (SCO) and  $\text{LaCrO}_3$  (LCO) were first grown on the STO substrate. Optimizing growth parameters is crucial for understanding the behavior of the parent compounds. Factors such as temperature, substrate-target distance, and pressure were carefully considered to ensure a thorough understanding.

A temperature-dependent behavior in the SCO phase was observed during XRD analysis of the parent compounds at varying growth temperatures. According to the findings shown in Figure 5.1, it can be inferred that the stability of SCO is heavily reliant on high temperatures. The absence of any Bragg peak related to the film for samples grown below 700 °C suggests that maintaining a certain temperature during the growth is essential for preserving the structural integrity of SCO. The optimal growth temperature for the LSCO solid solution was determined through a comprehensive assessment of the temperature-dependent structural properties of the parent compounds. LCO shows a larger possible growth window, with intense

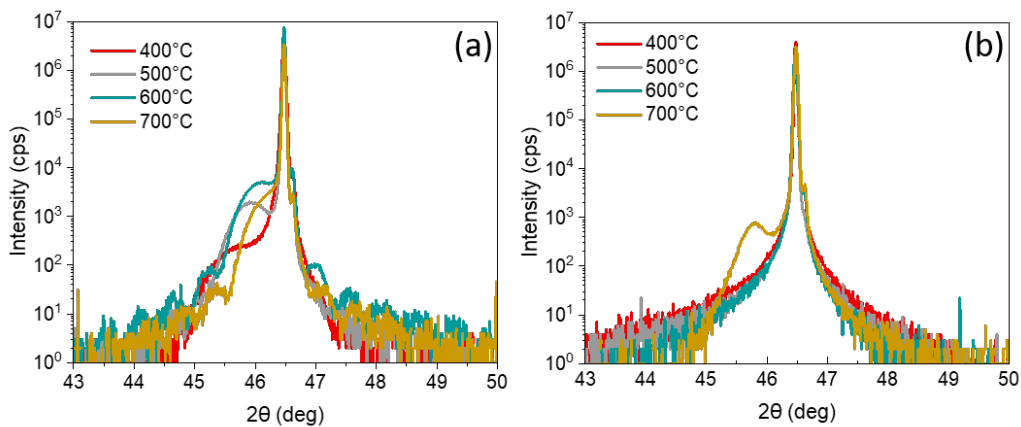


Figure 5.1:  $\theta - 2\theta$  scan of the (002) reflection of the  $\text{LaCrO}_3$  (a) and the  $\text{SrCrO}_3$  (b) thin films at various deposition temperatures.

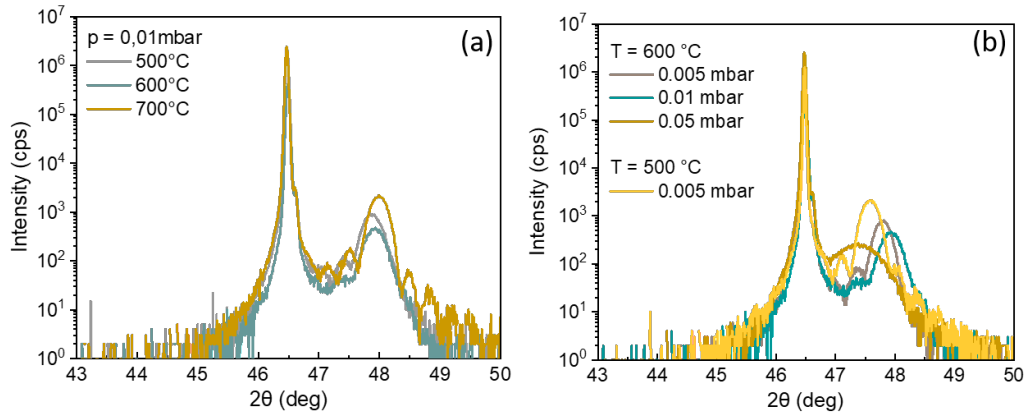


Figure 5.2:  $\theta - 2\theta$  scan of the (002) reflection of  $x = 0.33$  solid solution grown at different temperatures (a) and under different oxygen atmospheres (b).

thickness oscillations for all films. Therefore, it was found that a growth temperature of 700 °C would provide the most favorable conditions. The decision to ensure the formation of a well-defined phase within the solid solution was made with the aim of maintaining the stability of SCO, especially for the Sr-rich solid solutions.

The same calibration procedure as described in chapter 3.1.3, was performed on the laminates composed of LCO and SCO. The investigation involved the examination of different pulse combinations, particularly 1000/300, 300/1000, and 1000/1000 pulses, with the aim of identifying the deposition rate of each parent compound. According to the results, the deposition rate of SCO was 0.004718 nm per pulse, whereas the deposition rate of LCO was relatively low, measured to be 0.002762 nm per pulse.

### 5.1.1 Structural characterizations

In the present study, we have much less experience with the growth of Chromites compared with Vanadates. Also, the SrCrO<sub>3</sub> phase being instable, we have decided to conduct this study on the solid solution film. In order to study the influence of the deposition condition, the composition  $x = 0.33$  was subjected to various oxygen pressures and temperatures during deposition on STO (001) substrates. The maintenance of film stability, desired composition and crystalline structure may require the presence of oxygen during deposition. Insufficient oxygen pressure may lead to

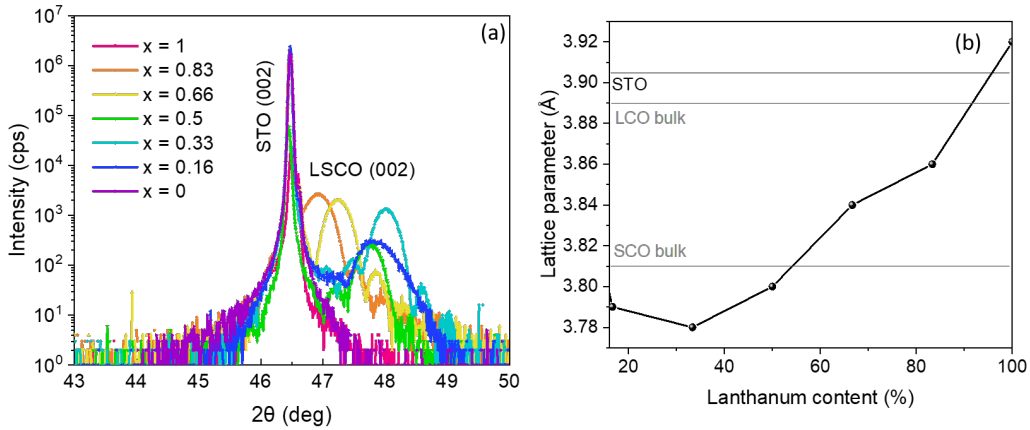


Figure 5.3: (a)  $\theta - 2\theta$  scan of the (002) reflection of the LSCO solid solution grown under optimal deposition parameters, (b) Out-of-plane lattice parameter evolution with the La content.

a non-stoichiometry in the films, that results from the inclusion of an inaccurate quantity of oxygen atoms, thereby impacting the atomic configuration and impeding the intended crystalline formation. The quality of thin films is also significantly influenced by temperature. The mobility of atoms within the film increases at higher temperatures. The increased thermal energy promotes the ability of atoms to surpass energy barriers and exhibit greater mobility, thereby fostering the development of homogeneous and properly oriented thin films.

The precise control of thin film quality was achieved through the simultaneous regulation of oxygen pressure and temperature during deposition. As these deposition conditions also influence the growth rate of the materials, in a possibly different way, a full calibration procedure was performed prior to each set of conditions using the laminate calibration method as described in the methods chapter. The X-ray diffraction (XRD)  $\theta - 2\theta$  peaks of the samples under investigation are illustrated in Figure 5.2. The optimal conditions for achieving both structural stability and high-quality electrical conductivity were determined based on the structural results and preliminary electrical characterization. The selected conditions include an oxygen pressure of 0.01 mbar during deposition and a temperature of 600 °C. The samples deposited under those specific conditions demonstrated the best electrical and structural outcomes.

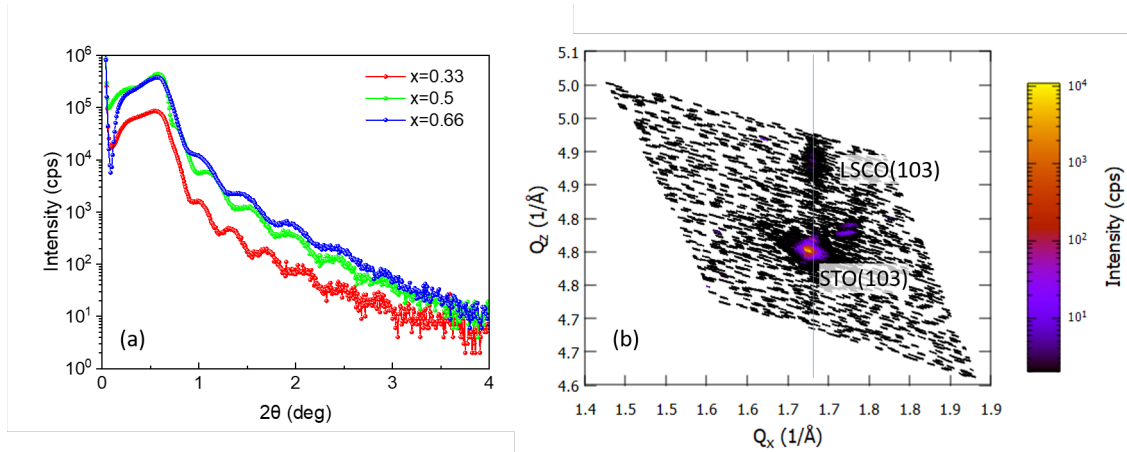


Figure 5.4: (a) X-ray reflectivity of LSCO solid solution samples for selected compositions, and (b) Reciprocal Space Map of the (103) reflection of the La<sub>0.33</sub>Sr<sub>0.67</sub>VO<sub>3</sub> solid solution thin film

Figure 5.3 illustrates XRD  $\theta-2\theta$  patterns for the solid solution set that was grown under optimal growth conditions. The observed shift in peak position, ranging from 46.9 to 48.1 °, is correlated to the variation in lanthanum concentration among the samples. Concerning the crystalline quality of the films, the Bragg peak of SCO ( $x = 0$ ) is absent, and the Bragg peak of the  $x = 0.16$  sample is markedly enlarged compared to the other compositions, with only barely visible Laue fringes. Therefore, it seems that this Sr-rich solid solutions may suffer, as SCO, from a chemical instability.

The graph depicted in Figure 5.3 (b) illustrates the variation of the lattice parameter  $c$  as a function of lanthanum doping. Unlike the LSVO system discussed in the previous chapter,  $c$  shows a linear evolution with respect to the lanthanum doping concentration. This confirms the relation with the change of strain state we have made for the LSVO system. Here, the lattice parameter of the solid solution is smaller than the substrate lattice parameter (3.905 Å) for all compositions, except the LCO (3.92 Å). Therefore, the LSCO system on STO (001) is under tensile strain for the full solid solution.

The XRR plot of the solid solution samples indicates the precise control on the film thickness. The observed oscillations in Figure 5.4 show a single period, indicative again on the high quality and the homogeneous density and composition of the films. The analysis of these patterns, in conjunction with the computational

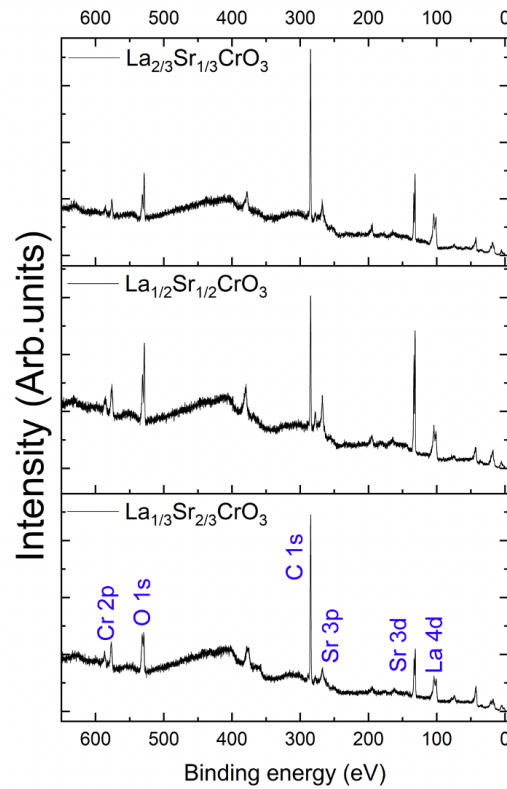


Figure 5.5: XPS survey spectra of LSCO solid solution thin films for specific  $\text{La}_x\text{Sr}_{1-x}\text{CrO}_3$  compositions ( $x = 0.33$  bottom panel, 0.5 middle panel, and 0.66 top panel) .

modeling methods delineated in the methods chapter, reveal that all the samples have a thickness of approximately 20 nm, with a low standard deviation of about 2 nm. This observation allows to estimate the uncertainty of the deposition growth rate to be about 10 %, demonstrating the reliability of the deposition machine and the calibration method.

In order to study the strain state of the LSCO solid solution films on the STO (001) substrate, reciprocal space maps were measured on the (103) reflection of the film and the substrate (an example is shown in Figure 5.4 (b)). Both peaks are visible in the RSM, and align at the same in-plane reciprocal lattice point  $Q_x$ , indicating that the LSCO films have the same in-plane lattice parameter as STO, and are therefore coherently strained.

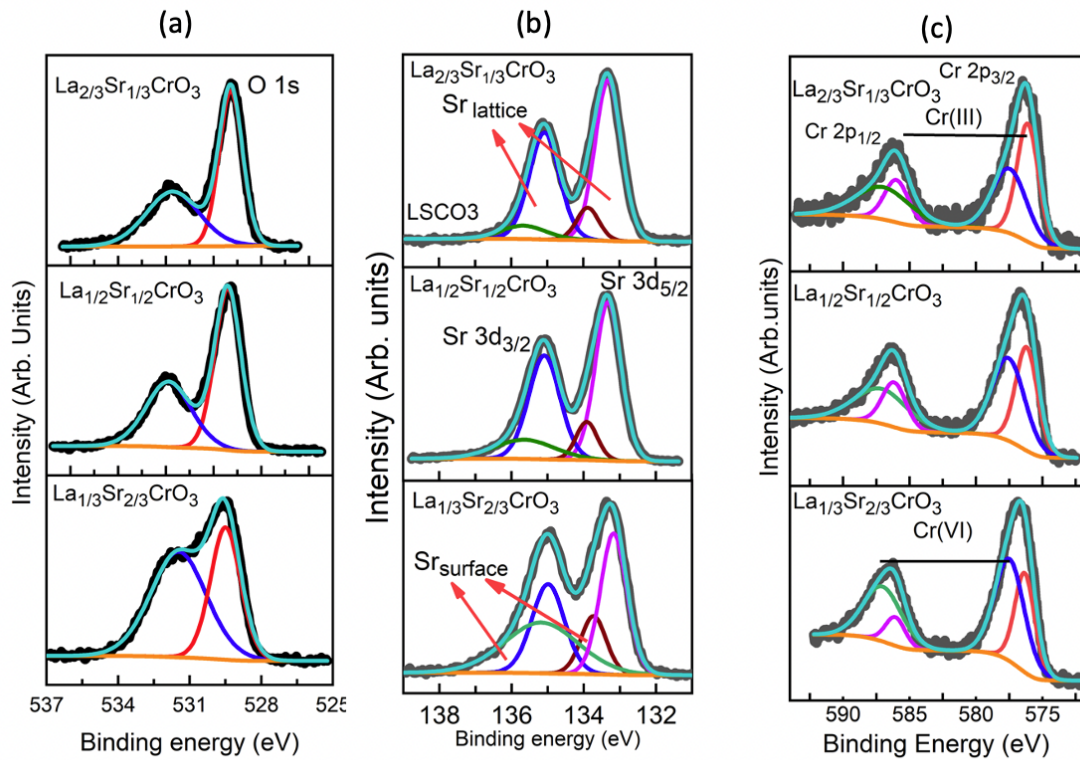


Figure 5.6: Core level variation with the lanthanum content: (a) O 1s (b) Sr 3d, and (c) Cr 2p.

### 5.1.2 Chemical characterization

XPS was used to examine the chemical composition of  $\text{La}_x\text{Sr}_{1-x}\text{CrO}_3$  thin films and the Cr oxidation states with varying compositions ( $x = 0.33, 0.5, \text{ and } 0.66$ ). The obtained La/Sr ratio complies with the nominal one, indicating that the calibration was reliable and accurate in the deposition of the LSCO thin film samples

The study involved also acquiring high-resolution XPS spectra for the O 1s, Cr 2p, and Sr 3d regions. The binding energies of these spectra were calibrated by utilizing the C 1s peak at 284.6 eV as a reference point. The O 1s spectra displayed a characteristic pattern of doublet peaks (Figure 5.6 (a)), suggesting the presence of two distinct oxygen environments. On the other hand, the Cr 2p peaks indicated the existence of  $\text{Cr}^{3+}$  and  $\text{Cr}^{6+}$  states, and the  $\text{Cr}^{3+}$  is found to increase with the addition of La (Figure 5.6 (c)). The analysis of Sr 3d peaks (Figure 5.6 (b)) demonstrated the presence of contributions originating from both the Sr inside the perovskite structure (called Sr lattice) and Sr at the chemically modified film

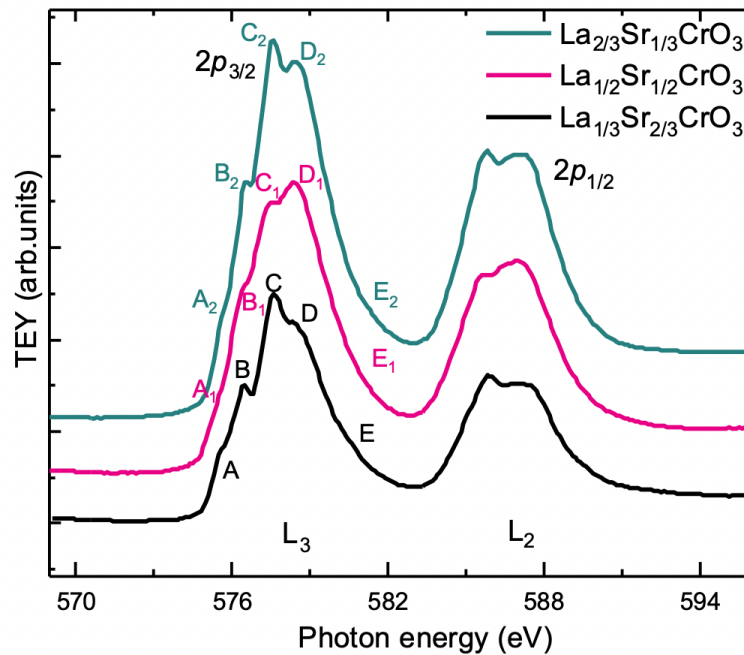


Figure 5.7: Cr L2,3-edge XAS spectra of  $\text{La}_x\text{Sr}_{1-x}\text{CrO}_3$  ( $x = 0.33, 0.50$  and  $0.66$ ) (LSCO) thin films grown on single crystal STO substrate.

surface. However, it was observed that the influence of surface Sr content decreased as the La content increased in the LSCO films.

The thin films have demonstrated enhanced signals of  $\text{Cr}^{6+}$  in the Sr-rich solid solutions. This could be an indication of surface instabilities, possibly due to overoxidation. On the other hand, the addition of La seems to withdraw the surface instability, as shown by the appearance of the  $\text{Cr}^{3+}$  signal alongside with a strong Sr lattice signal. This suggests that La could play a pivotal role in enhancing the chemical stability of the solid solution, as was also observed in the LSCO system.

Figure 5.7 presents the XAS measurements conducted on thin films composed of LSCO with the same La compositions as for the XPS measurements ( $x = 0.33, 0.50$ , and  $0.66$ ). The XAS spectra were acquired by observing the Cr L2,3-edge in a total electron yield configuration at Elettra. The spectra exhibit peak separation in the L3 and L2 regions as a consequence of the spin-orbit splitting energy associated with the Cr 2p core hole. The L3 region exhibits peaks denoted as A, B, C, D, and E, which correspond to the relative intensities of atomic and crystal field interactions within the atomic multiplet. [123]

When comparing the spectra of thin films of LSCO with varying La compositions, it is observed that the films with La compositions of  $x = 0.33$  and  $x = 0.66$  display similar line shapes, especially when comparing the relative intensities of the peaks labeled C and D. Nevertheless, the film with  $x = 0.50$  shows distinct differences compared to the other two samples. It is worth mentioning that the film with  $x = 0.50$  exhibits a decrease in the intensities of the B and B1 peaks, which are rather typical for the low-energy part of the Cr<sup>3+</sup> XAS spectrum [123]. Furthermore, the observed increase in D1 and decrease in C1, relative to their respective counterparts (C, C2, and D, D2), suggest that the majority of Cr ions are in the tetravalent state, whereas the trivalent Cr ions are present in minimal amounts. Finally, the XPS and the XAS results of the  $x = 0.33$  sample do not go together: while XPS shows a deteriorated surface, XAS shows a rather normal Cr<sup>3+</sup> surface. When enhancing La,  $x = 0.5$  to  $x = 0.66$ , the two techniques show the same enhancement of the Cr<sup>3+</sup> signal. It is not possible at this state to understand these differences observed in the  $x = 0.33$  sample, except maybe a small difference of the sampling depth of the two techniques. However, the results are concordant that La - doping helps to stabilize the Cr<sup>3+</sup> at the surface of the thin films.

## 5.2 TCO properties of LSCO solid solution thin films

This section of the study examined the impact of the La doping concentration on the electrical conductivity of the LSCO thin films. In this study, a Physical Property Measurement System (PPMS) was utilized in a four-point configuration to assess the temperature-dependent changes in the electrical resistivity of the thin films, as described in the methods chapter 3.4.1.

The temperature-dependent electrical resistivity ( $\rho(T)$ ) of LSCO thin films with compositions  $x = 0.16, 0.33,$  and  $0.66$  is depicted in Figure 5.8. It was not possible to measure the parent compounds as  $\text{LaCrO}_3$  is too resistive for the PPMS setup, and the  $\text{SrCrO}_3$  film showed a deteriorated resistivity, probably due to the instability of the film. It is noteworthy that all three solid solution samples exhibit a semiconducting behavior, which is characterized by a notable reduction in resistance with increasing temperature. The impact of lanthanum doping on the resistivity of LSCO systems can be observed both in the room temperature value of the resistivity, as also in the different temperature evolutions. The composition with  $x = 0.16$  shows the lowest resistivity and a relatively shallow resistivity dependence on temperature. An increase in resistivity occurs with higher levels of lanthanum doping. An increase in resistivity occurs with higher levels of lanthanum doping, as expected based on the

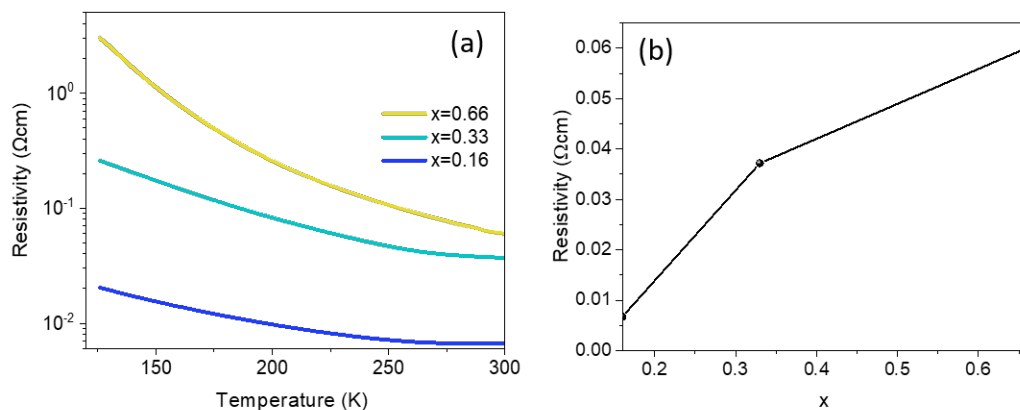


Figure 5.8: (a) Resistivity as a function of temperature of the LSCO solid solution thin films, (b) Room temperature resistivity as a function of lanthanum doping.

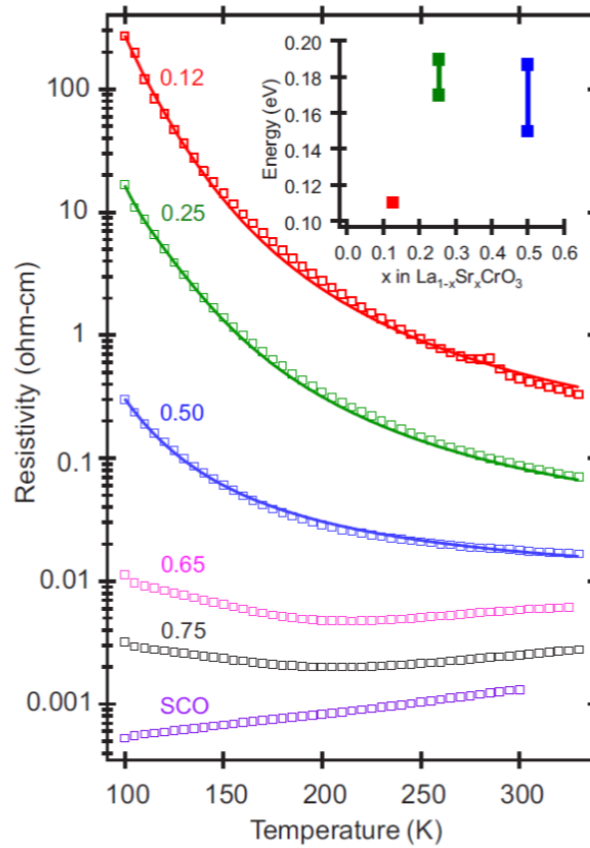


Figure 5.9: Resistivity as a function of temperature of the  $\text{La}_{1-x}\text{Sr}_x\text{CrO}_3$  solid solution thin films taken from [18]. Note the different definition of  $x$ , being here the Sr content.

reported properties in literature [15, 18]. When substituting Sr by La, the nominal oxidation state of Cr changes partially from  $\text{Cr}^{4+}$  with a  $3d^2$  electronic configuration to  $\text{Cr}^{3+}$  with  $3d^3$ . Therefore, the holes responsible for the conduction are partially filled with electrons, which leads to a lower p-type charge carrier density and a higher resistivity.

It is noteworthy that at room temperature, the resistivity goes from  $0.0597 \Omega\cdot\text{cm}$  for the composition  $x = 0.66$  to a remarkably low value of  $0.0068 \Omega\cdot\text{cm}$  for the composition  $x = 0.16$  (Figure 5.8 (b)). The findings demonstrate a strong consistency with values documented in the existing body of literature on MBE grown films (Figure 5.9). The uniformity of resistivity measurements observed in multiple investigations underscores the reproducibility of these results and establishes a sturdy basis for comprehending the fundamental mechanisms that regulate the electrical

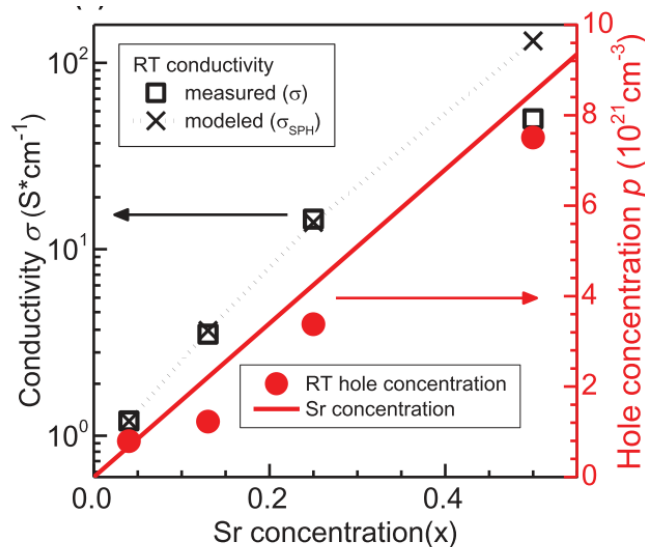


Figure 5.10: Room temperature conductivity and hole concentration versus Sr content  $x$  adapted from [15]. Note the different definition of  $x$ , being here the Sr content.

characteristics.

The same group, in another publication concerning the TCO properties of LSVCO [15], have reported the evolution of the conductivity of the low Sr concentration thin films, showing an enhancement in the electrical properties with the Sr doping, as shown in Figure 5.10. With our study, we were able to give a view more into the high Sr doping ( $x = 0.33$  La) which follows the tendency of the observed evolution. This gives an overview of the full evolution of the electrical resistivity within LSCO thin film solid solution.

The investigation of the electrical properties of thin film samples of LSCO through Hall measurements was found to be a highly challenging task. This was due to the fact that the samples exhibited a high resistance that exceeded the measurement range of the PPMS used for characterization. In order to overcome this problem, various strategies were employed such as depositing gold, silver, and chromium surface contacts at the edges of the thin films, with the aim of controlling the contact resistance. Another approach was to shorten the distance between the contacts by depositing electrical contacts in the middle of the sample. Nevertheless, we were not able to measure a reproducible Hall signal allowing for the extraction of the charge density, and their mobility.

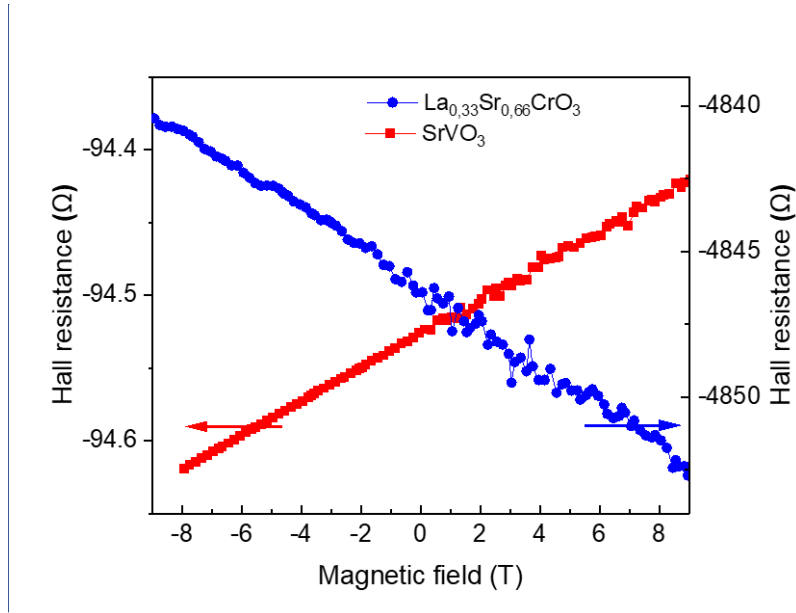


Figure 5.11: Hall resistance slope of SVO and LSCO ( $x = 0.33$ )

Despite the non-reproducibility, samples may display a Hall measurement with a constant slope that was opposite to that of SVO, a well-established n-type conductor (Figure 5.11). Although this individual specimen does not offer a conclusive proof, the p-type conduction of LSCO has been largely documented before [97, 101, 124]. Oxide p-type conductors are typically characterized by a high resistivity and semi-conducting behaviour, which is also the case in the thin films of this study. Therefore, having demonstrated the expected composition by XPS/XAS, and the similar resistive properties, we infer that our films are p-type conductors.

The optical characteristics of the LSCO solid solution system were examined, revealing a remarkable level of transparency throughout the sample set (Figure 5.12). The transparency levels exceeded 50 % across the entire visible range. The degree of transparency exhibited by these materials is of notable importance, as it underscores their prospective utility in diverse optoelectronic devices. Nevertheless, upon comparison with the parent compounds, it can be observed that the solid solution LSCO exhibits a smaller transparency than the parent compounds with a transparency exceeding 85 %. Several factors can be attributed to the discrepancy in transparency between the LSCO solid solution and its parent compounds. The change of the charge carrier effective mass with doping, but also defects could be resulting in

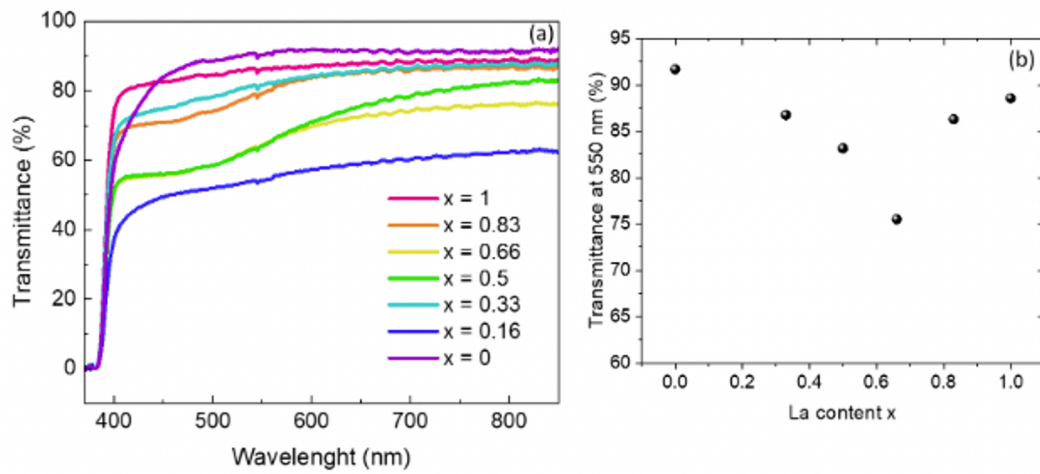


Figure 5.12: Optical transmission of the LSCO solid solution thin films as a function of wavelength (a), and the transmittance of the films with different composition at a wavelength of 550 nm (b). Here, the  $x = 0.16$  sample was left out for clarity, where the low transmittance is probably due to experimental problems with the substrate.

supplementary light scattering or absorption. The substitution of lanthanum and strontium in the Chromite lattice leads to an altered electronic structure, which could potentially affect the material's absorption characteristics by modifying the bandgap or altering the band edge states.

Taking into consideration all the results, the composition  $\text{La}_{0.33}\text{Sr}_{0.67}\text{CrO}_3$  has shown the optimal choice due to its unique combination of surface stabilization, exceptional electrical and optical properties.

## 5.3 Strain engineering of LSCO

As discussed in the state of art section, strain engineering in thin film oxides entails the application of strain to thin films of oxide materials with the aim of altering their physical properties. This methodology takes advantage on the fact that the lattice parameters of the substrate and the thin film can have a mismatch, thereby inducing strain in the film during its growth on the substrate. The use of different (001)-oriented substrates, namely LSAT ( $a = 3.87 \text{ \AA}$ ), LAO ( $a = 3.82 \text{ \AA}$ ), and STO ( $a = 3.905 \text{ \AA}$ ), enables the investigation of the impact of strain on the physical properties of thin films. The application of compressive strain on the LSCO film is induced when the lattice constant of the substrate exceeds that of the film. On the contrary, in cases where the substrate's lattice constant is smaller than that of LSCO, it results in the imposition of tensile strain on the film. Two compositions, namely  $x = 0.33$  and  $0.66$ , were deposited on all three substrates. We have decided to reduce this study to two interesting compositions and not to grow all solid solution compositions, in order to reduce the number of samples necessary for this study. Specifically, LSCO deposition on LAO should lead to a compressive strain for the two considered compositions, whereas LSCO deposition on LSAT would result in a slighter compression or tensile depending on the composition. Conversely, deposition on STO should lead to a tensile strain in any case.

### 5.3.1 Structural Analysis

Judging on the XRD patterns of the respective films, the thin films grown on LSAT and LAO exhibit good crystalline quality, as illustrated in Figure 5.13. The films on the LSAT substrate exhibit higher quality, as inferred from the number and the intensity of the Laue fringes, probably due to its low misfit with the film. Compared to LSAT, the Laue fringes on the LAO substrate exhibit a reduced prominence. Nevertheless, the quality of the film persists to be quiet good.

The strain state of the films were determined by Reciprocal Space Maps (RSM) using the (103) reflections. As an example, the RSMs of the films on LAO (001) are shown in 5.14. In this case, the coinciding in-plane lattice vector of the film and the

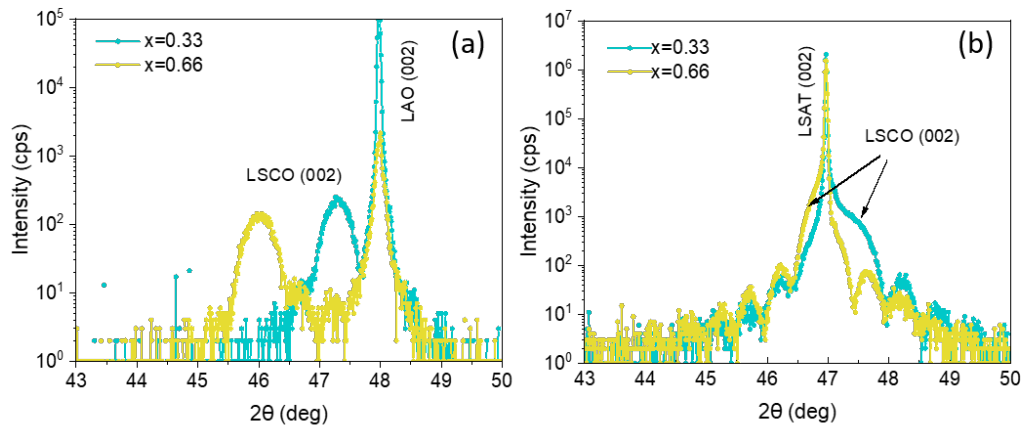


Figure 5.13:  $\theta - 2\theta$  scan of the (002) reflection of  $x = 0.33$  and  $0.66$   $\text{La}_x\text{Sr}_{1-x}\text{CrO}_3$  solid solution thin films on LAO (a) and LSAT (b).

substrate for the  $x = 0.66$  composition indicates a coherently strained state, while the  $x = 0.33$  composition shows a relaxed state, due to the high misfit of the system. The strain state was quantified for all films using the relative deformation ratio  $c/a$  of the out-of-plane lattice parameter  $c$  and the in-plane-lattice parameter  $a$  of the film. The deformation is presented in Table 5.1. The aforementioned relative deformation ratio serves as a reliable indicator of strain, while disregarding the plausible chemical alterations that may occur with respect to oxygen atoms and other related factors.

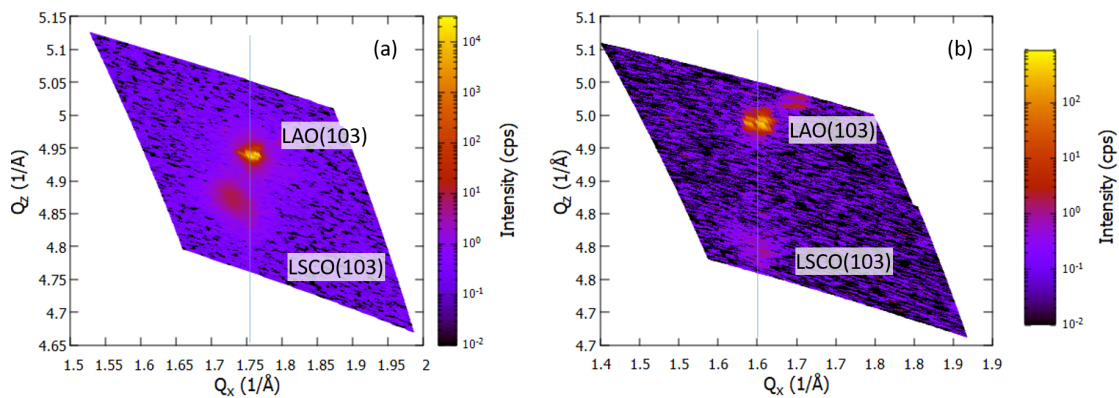


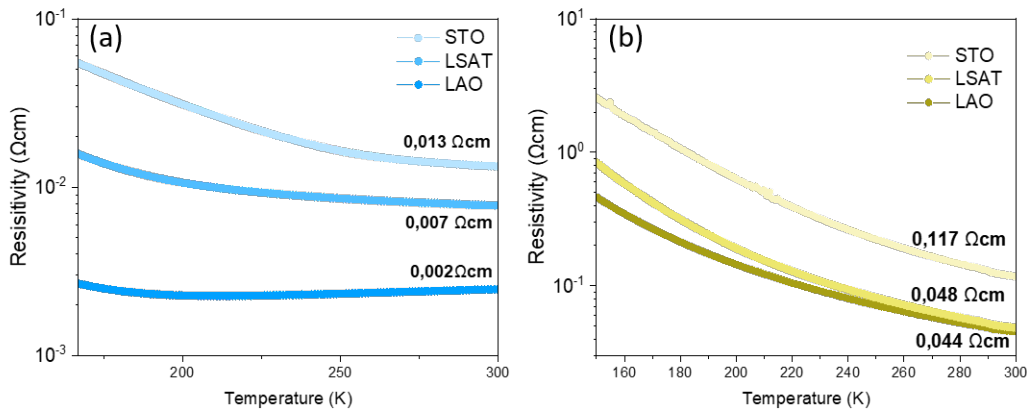
Figure 5.14: Reciprocal space maps of the (103) LSCO films and  $\text{LaAlO}_3$  substrate, for (a)  $x = 0.33$  and (b)  $x = 0.66$ .

substrate	$x = 0.33$	$x = 0.66$
LAO (001)	0.999 (relaxed)	1.03
LSAT (001)	1.006	1.005
STO (001)	0.96	0.981

Table 5.1: Table of the deformation  $c/a$  of two different La<sub>x</sub>Sr<sub>1-x</sub>CrO<sub>3</sub> compositions

### 5.3.2 Electrical properties

Figure 5.15 illustrates the resistivity as a function of temperature for the two distinct compositions on the three different substrates. The data on STO was added here for sake of comparison. In Figure 5.16, the room temperature values are summarized as a function of the lattice deformation  $c/a$ . Independently on the solid solution composition, the observations are the same. The LSCO films that have been deposited on the STO substrate demonstrate the highest resistivity, and the films grown on LAO demonstrate the lowest resistivity values, even the  $x = 0.33$  film in the relaxed state. This observation suggests that the electronic configuration or carrier mobility within the LSCO system is positively affected by an elongation of  $c$  with respect to  $a$ , either by compressive strain or by chemical modifications of the film. An elongation of  $a$  with respect to  $c$ , i.e. films in tensile strain, leads to an increase of the resistivity. The same behaviour was already shown for  $x = 0.77$  films on different substrates [101], confirmed here with different compositions. The increase of the La doping level showed a general increase in the resistivity on all

Figure 5.15: Resistivity as a function of temperature of the LSCO solid solution deposited on various substrates: (a)  $x = 0.33$ , (b)  $x = 0.66$ .

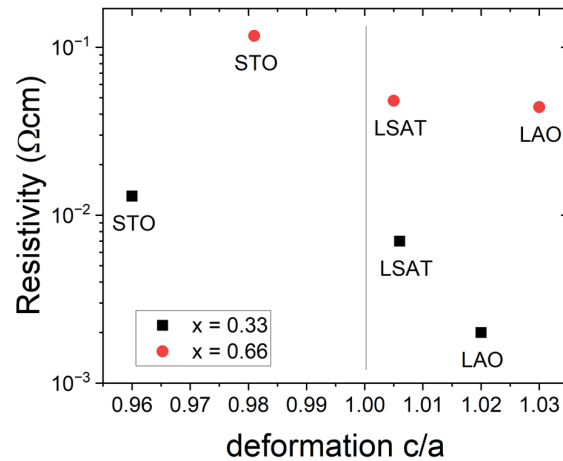


Figure 5.16: Room temperature resistivity of the composition  $x = 0.33$  and  $0.66$  thin films as a function of the lattice deformation  $c/a$

substrates. It is also worth noting that, the film crystalline quality plays a small role in this particular case as the films deposited on LAO demonstrated the lowest resistivity, although they show a lower structural quality.

The decrease in electrical resistivity in LSCO thin films with  $c/a \geq 1$  on the LAO substrate can be attributed to two main factors, namely, an increase of orbital overlap and potential chemical alterations resulting from variations in oxygen content. The compressive strain induces a modification in the lattice parameters of the LSCO film, thereby causing a smaller distance between the Cr ions, which facilitates an increased level of orbital overlap among adjacent atoms within the film. Enhanced orbital overlap facilitates electronic interaction between atoms, thereby enabling more effective charge transport. Furthermore, the LSCO film can undergo chemical alterations regarding the oxygen content, which is probably the reason of the deformation of the  $x = 0.33$  film on LAO. The chemical interaction with the substrate has the potential to modify the concentration of oxygen vacancies or impact the kinetics of oxygen diffusion within the film. Variations in the oxygen concentration can exert a substantial influence on the electronic properties.

The investigation on strain engineering of LSCO thin films did not include optical measurements as an aspect of the study. The reason for this exclusion is due to the involvement of the substrate in the optical assessments. The substrate can interfere

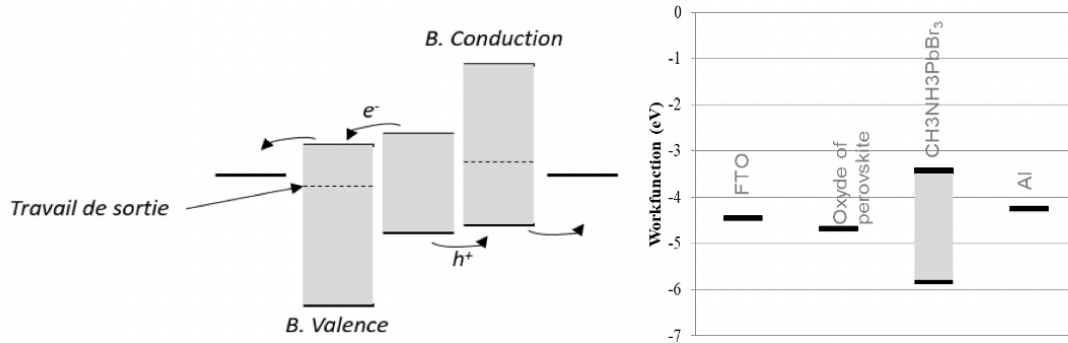


Figure 5.17: Schematics of the band alignment in a solar cell, and an overview of the work function of different materials including F-doped SnO<sub>2</sub> (FTO) and other materials.

with the measured optical response, making it difficult to isolate the intrinsic optical properties of the thin film. Given that the primary objective of this investigation was to understand the impact of strain on the physical characteristics of LSCO films, the optical assessments were deliberately skipped, especially because of the nature of the LAO substrate. The focus of the study was primarily on characterizing other properties, such as electrical resistivity or structural analysis, that could be more accurately associated with the changes in the film's properties induced by strain.

### 5.3.3 Integration with solar cell materials

In collaboration with Sylvain Vedraïne and Ceren Yildirim from the XLIM laboratory in Limoges, France, the possibility of the integration of LSCO thin films in existing solar cells was studied. The principal aim of this collaboration was to explore the use of LSCO as an interface layer in solar cell devices for the adaptation of the p-type side band structure for efficient extraction of the charges. Therefore, a particular focus was put on the analysis of the work function. Such an interface layer is considered ideal when exhibiting a number of crucial characteristics, namely high transparency, high selective conduction of charge carriers, efficient blocking of charge carriers, and a certain level of conductivity.

In order to test LSCO for the use as an interface layer, a range of LSCO composi-

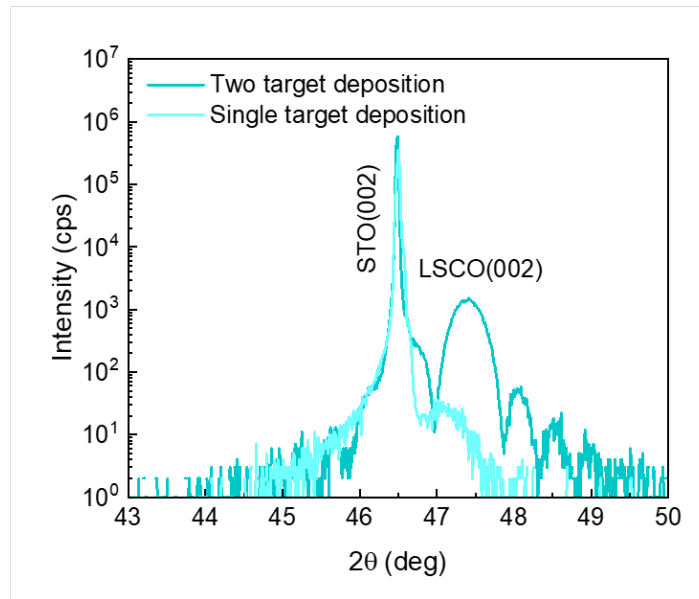


Figure 5.18:  $\theta - 2\theta$  scan of the (002) reflection using double target (parent compound), and mono target with specific LSCO  $x = 0.33$  composition.

tions were deposited on glass substrates covered by fluorine-doped tin oxide (FTO), that were analyzed in a systematic manner to investigate the effects of composition and thickness on the properties of the interface layer under consideration. The samples were divided into two separate groups: the initial group was intended to assess the impact of altering the lanthanum content within the solid solution. In the compositional set, LSCO thin films with a thickness of around 20 nm were synthesized, while the lanthanum content was methodically altered to assess its impact on the interface layer's efficacy. The second group was centered on investigating the impact of film thickness on the material's characteristics. In order to achieve high thickness values, we have used a single target with  $x = 0.33$  composition. Using two targets increases strongly the deposition time, due to the time needed to rotate the targets, which may lead to laser instabilities if the deposition time exceeds 45 min. Using a single target with one desired La/Sr composition allows to reach thickness values of about 50 nm. The aim is to evaluate the influence of the film thickness on the material characteristics.

It is worth nothing the importance of the use of a two-target approach in the synthesis of LSCO thin films. Figure 5.18 shows XRD patterns obtained on two films deposited under similar deposition conditions, but one with a double-target

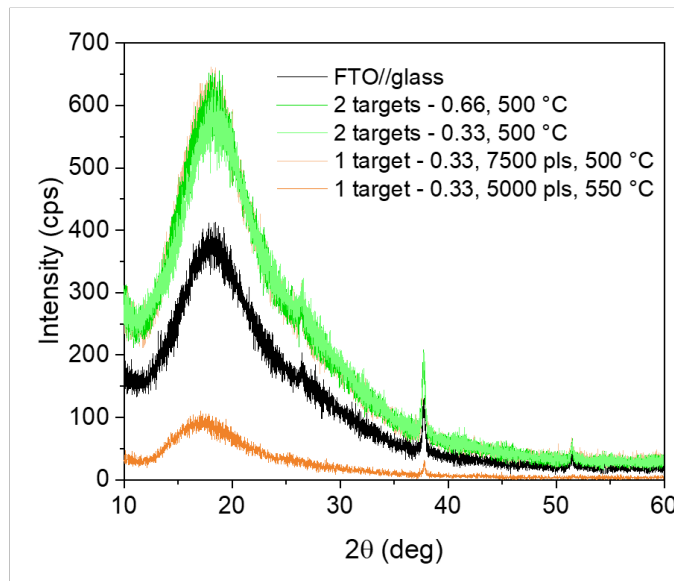


Figure 5.19:  $\theta - 2\theta$  scan of LSCO deposited on FTO under different conditions.

deposition, and the other with a single-target deposition. It is clearly observed that the crystalline quality of the two target films is markedly enhanced in comparison to those generated via the single-target method. The improved crystalline quality of the thin films produced through the utilization of the two-target approach is attributed to the longer deposition time, that enables the atoms to order and therefore results in better quality. This enables the creation of a highly organized lattice structure and reduces the possibility of defects or interstitial impurities. On the one hand, the single-target methodology presents certain benefits in relation to deposition time and ease of use. On the other hand, it may result in a less optimal crystalline quality of the films.

When growing LSCO thin films on the FTO-covered glass substrates, one of the primary challenges encountered in this case is achieving the delicate equilibrium between optimizing the thin film growth conditions and maintaining the substrate's integrity. The LSCO solid solution thin films exhibit optimal growth at a temperature of 600 °C. However, the use of such high temperature may lead to potential damage or degradation of the FTO film or the melting of the glass substrate, thereby compromising the overall performance of the device. In order to tackle this crucial matter, a methodical exploration of the growth temperature was undertaken, with

the objective of identify an appropriate temperature interval that would enable the growth of LSCO films of the necessary quality, while avoiding any damage to the FTO substrate.

In order to determine the crystalline structure of the LSCO solid solution thin films on FTO-covered glass, we have carried out different methods of XRD characterization, but we were not able to observe peaks related to the LSCO thin film. It has to be pointed out here that the FTO layers are polycrystalline, and do not propose a monocrystalline growth template to the LSCO layer. Therefore, the LSCO film is supposed to be also polycrystalline, reducing strongly the intensity of the possible peaks. It should be noted that the investigated samples possess an FTO layer with an estimated thickness of 150 nm. Typical  $\theta - 2\theta$  scans are presented in Figure 5.19 showing a large amorphous peak just below  $20^\circ$  with some superposed peaks related to the FTO layer. The selected data on sample with a LSCO film there are no additional features visible, compared to the reference (black curve). Therefore, it is impossible to determine the crystalline structure or the quality of the deposited LSCO films from these measurements.

However, it is possible from electrical measurements to determine the successful growth of the LSCO layer. Using a multimeter, the resistance values of a bare FTO - covered glass substrate were collected before the deposition of a LSCO thin film. For high deposition temperature  $\geq 600^\circ\text{C}$ , the surface of the films were domed, indicating a partial melting of the glass, and the resistance was observed to be too high to be measured. For smaller deposition temperatures, the resistance of the deposited LSCO film was compared to the FTO film underneath. This was possible using a mask covering a part of the substrate surface during LSCO deposition. When the LSCO resistance was still possible to be measured, but higher than the underlying FTO layer, the LSCO film was supposed to be constituted. The FTO films showed a similar resistance before and after the LSCO deposition at these temperatures, indicating a preserved FTO quality. Thus, with a lack of techniques allowing to detect the LSCO layers, we suppose that LSCO thin films can be grown at sub- $550^\circ\text{C}$  temperatures without compromising their intended characteristics, while mitigating the potential harm to the FTO substrate. With the earlier demonstrated

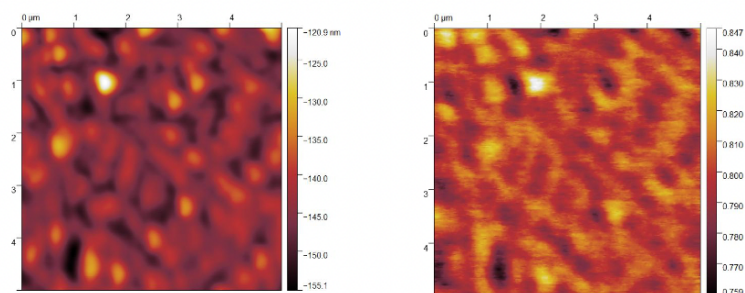


Figure 5.20: Kelvin Probe Force Microscopy (KPFM) measurements for a  $x = 0.33$  thin films deposited from two targets at 500 °C (a) surface topography, (b) work function distribution.

reliability of the calibration procedure, the La/Sr composition of the films and the thickness should correspond to the intended values.

Topographical analysis is a critical factor in evaluating the uniformity and quality of the LSCO films. Kelvin Probe Force Microscopy (KPFM) measurements were carried out at the XLIM, in order to examine the surface potential fluctuations present in the LSCO thin films (Figure 5.20) as well as an estimation of the work function of the material. The topography (Figure 5.20 (a)) shows an homogeneous grain structure, with a height variation of about 30 nm. As the FTO layer also has an inherent roughness related to its thickness of 150 nm, it cannot be concluded on the homogeneity of the LSCO film based on this measurements. However, the KPFM measurements demonstrate an average value of the work function of 4.63 eV and a negligible variation of the surface potential below  $\pm 0.05$  eV throughout the examined samples. The present observation strongly indicates a considerable degree of homogeneity of the thickness and of the composition of the LSCO thin film layer, given the inherent measurement error of KPFM being approximately 0.1 eV. The homogeneity observed in the properties of the film is a favorable characteristic that can facilitate the maintenance of uniform and predictable functional features throughout the material. Consequently, this can lead to an improvement in the overall efficiency and dependability of the devices integrating LSCO thin films. The obtained work function value is perfectly matching its intended use as a interface layer (see Figure 5.17), as it is situated next to the work function of FTO and in

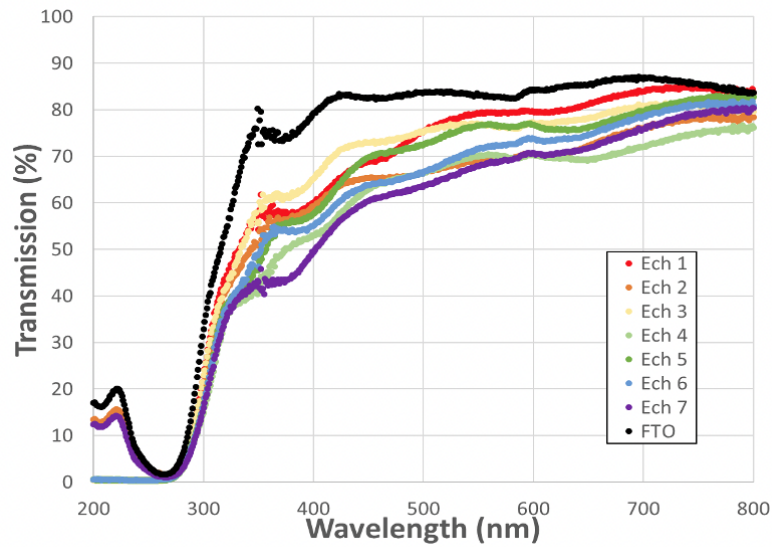


Figure 5.21: Optical transmission of LSCO thin films deposited on FTO under different growth parameters.

the area of what is possible with Organometal Halide Perovskites, being one of the standards for high efficiency solar cells [125].

All samples demonstrated high optical transparency. The results of the optical transmission measurements carried out on the LSCO films deposited on the FTO-covered glass substrates (Figure 5.21) indicate a significant signal of the substrate, as can be appreciated by the signal of the reference FTO sample (black line). In such circumstances, it is preferable to correct the measured transmission by the transmission of the glass/FTO reference, in order to determine the transmission of the LSCO films. In cases where the thickness of the film is equal to or less than the wavelength of light, this treatment may become complicated due to the emergence of optical interference effects. It is important to note that the interference phenomena exhibited by the glass/FTO sample cannot be compared with those of any glass/FTO/oxide sample. Therefore, they cannot be corrected without careful consideration. Despite the aforementioned difficulties, our study has evidenced that the selected thicknesses of oxide layers can attain elevated degrees of transmission within the visible spectrum, rendering them highly suitable for deployment as an interface layer in solar cells or LEDs. The high transmission within the visible spectrum is a crucial characteristic for stated applications, as it guarantees effective

absorption or emission of light, ultimately bolstering the efficacy and efficiency of photovoltaic devices.

The determination of particular properties, such as the bandgap value, which should be situated within the 2.5 eV to 4.2 eV range corresponding to wavelengths from 300 nm to 500 nm, may require an increased film thickness. Therefore, only the transmission in itself will be discussed while the analysis of these particular properties is scheduled in a later time.

Fluorescence measurements were conducted as well. The objective was to analyze the photoluminescence characteristics of the LSCO thin films and obtain a better understanding of their electronic structure and the energy levels that participate in the recombination processes. The aforementioned data can be of great significance in understanding the role of the material in diverse optoelectronic implementations, such as photovoltaic cells and light-emitting diodes. Regrettably, the fluorescence measurements did not produce statistically significant outcomes in this instance. The substrate's strong reaction has resulted in signal saturation, posing a significant challenge in extracting any substantial insights concerning the LSCO thin film layer. The aforementioned result underscores the necessity for additional refinement of the experimental parameters in order to attain dependable and comprehensible fluorescence data. A plausible strategy for improving the fluorescence measurements is to deposit the LSCO thin film onto a quartz substrate, which manifests a lower signal intensity in comparison to the present substrate, consequently mitigating the probability of substrate-induced interference. Furthermore, enhancing the thickness of the LSCO layer could potentially enhance its fluorescence signal, thereby increasing the likelihood of acquiring significant outcomes. Therefore, more work is necessary to characterize the LSCO/FTO system in more details, as the preliminary results show promising properties of the p-type LSCO in photovoltaic applications.

## CHAPTER 6

---

### General conclusion and perspectives

---

In summary, this thesis was dedicated to the development of La/Sr solid solution thin films of perovskite oxide transparent conductors. We have successfully accomplished the growth of thin films of lanthanum strontium vanadium oxide (LSVO) with range of diverse compositions. The LSVO thin film samples have been subjected to a thorough structural characterization, which has provided insights into their high crystalline quality. By conducting exhaustive chemical characterizations, such as X-ray Photoelectron Spectroscopy (XPS) and X-ray Absorption Spectroscopy (XAS), the oxidation states of the vanadium have been determined, therefore offering valuable insights into their evolution under various atmospheric conditions. Significantly, it has been established that lanthanum plays an essential role in the stabilization of the thin films from surface oxidation, which is frequently observed in thin films of strontium Vanadate (SVO). The examination of strain engineering has shed light on its influence on the physical characteristics of LSVO thin films. It is worth noting that the application of compressive strain has been observed to increase the level of electronic correlations within the material, consequently leading to an increase in effective mass. Nevertheless, the introduction of oxygen vacancies has a negative impact on the electrical properties when the material is grown on a strontium

Titanate (STO) substrate. This emphasizes the superior appropriateness of using a lanthanum strontium Aluminium Titanate (LSAT) substrate in order to achieve improved electrical characteristics. Moreover, the growth of LSVO solid solutions on LSAT substrates has revealed intriguing optical characteristics, specifically a transparent region at shorter wavelengths in comparison to samples deposited on STO substrates. After considering the impact of lanthanum doping and strain engineering on the properties of LSVO thin films, it has been determined that the composition of  $\text{La}_{0.33}\text{Sr}_{0.67}\text{VO}_3$ , when deposited on LSAT, exhibits the most favorable characteristics as a Transparent Conductive Oxide (TCO). The introduction of lanthanum serves as a stabilizing factor against surface oxidation, while simultaneously improving good optical and electrical characteristics.

The achievement of synthesizing thin films of lanthanum strontium chromium oxide (LSCO) solid solution with diverse compositions has yielded significant findings. By means of growth optimization, we were able to attain crystalline structures of superior quality and enhanced conductivity. The presence of strontium appeared to induce a  $\text{Cr}^{6+}$  oxidation state, indicating a potential surface instability to overoxidation, especially at higher Sr levels. Lanthanum doping effectively mitigated this instability, observed by the introduction of  $\text{Cr}^{3+}$ . The resistivity at room temperature exhibited a notable decrease from La-rich composition ( $\text{La}_{0.66}\text{Sr}_{0.34}\text{CrO}_3$ ) to Sr-rich compositions ( $\text{La}_{0.16}\text{Sr}_{0.84}\text{CrO}_3$ ), which aligns with the results reported in previous works. The transparent character of the material was clearly observable, exhibiting a transparency level exceeding 50% throughout the visible spectrum. It is worth mentioning that the composition  $\text{La}_{0.33}\text{Sr}_{0.67}\text{CrO}_3$  has emerged as the optimal choice due to its unique combination of surface stabilization, exceptional electrical and optical properties. Consequently, this composition holds great promise as a p-type material for transparent conducting oxides. Furthermore,  $\text{La}_{0.33}\text{Sr}_{0.67}\text{CrO}_3$  thin films were deposited on F-doped  $\text{SnO}_2$  covered glass substrates, and demonstrated a work function particularly well adapted as an interface material for p-type halide perovskites. This discovery bears considerable significance, especially within the field of solar cells.

In summary, our extensive investigation, including various aspects as high quality

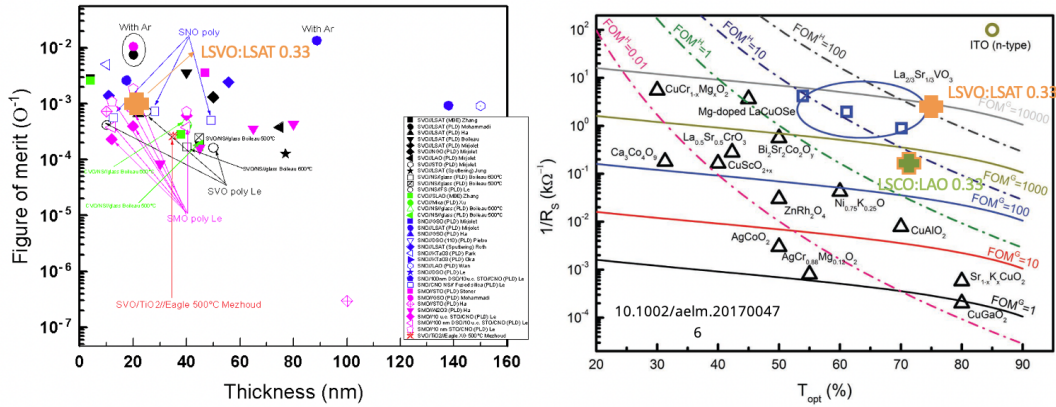


Figure 6.1: Graphical representation of figure of merit (electrical resistance and optical transmission) for the LSVO and LSCO thin films in comparison with other typical TCO's.

thin film growth, structural, chemical, electrical and optical characterisation, as well as strain engineering, has provided insights into the suitability of lanthanum strontium vanadium oxide (LSVO) and lanthanum strontium chromium oxide (LSCO) for application as a transparent conducting oxide (TCO) for optoelectronic devices. The successful development of LSVO and LSCO thin films, under the guidance of optimal conditions, highlights their potential for industrial applications.

To evaluate the performance of our samples in comparison with others, we employ a methodology involving a standard criterion known as Figure of Merit (FoM). Researchers have long sought a reliable FoM for assessing material performance. In 1976, Haacke [126] introduced a straightforward and practical FoM that correlates the transmittance ( $T$ ) and the sheet resistance ( $R_s$ ), where  $R_s$  is the reciprocal of the film thickness ( $R_s = 1/\sigma d$ , with  $d$  denoting the film thickness). This FoM, denoted as  $F$ , is expressed as:

$$F = T^q/R_s = T^q \sigma d$$

This FoM includes a parameter  $q$ , which dictates the transmittance level required for a specific application. Typically,  $q = 10$  is chosen, as a transmittance of 90% is deemed sufficient for most purposes.

Figure 6.1 illustrates a comprehensive comparison of the Figure of Merit (FoM) for the optimal compositions of LSVO (lanthanum strontium vanadium Oxide) and LSCO (lanthanum strontium Cobaltite) in relation to various other materials. This

visual representation effectively highlights the remarkable combination of excellent optical and electrical performances exhibited by LSVO and LSCO. The FoM serves as a valuable metric to assess the overall quality of these materials, taking into account their transmittance and sheet resistance. In this context, both LSVO and LSCO stand out as they not only demonstrate superior optical transparency but also exhibit remarkable electrical conductivity. This unique synergy between optical and electrical properties positions these materials as promising candidates for a wide range of applications, where both aspects are of paramount importance.

However, it is important to note that this quantification tends to emphasize optical transparency at times. A material could achieve a high FoM with a transmittance  $>90\%$ , even if the sheet resistance is exceptionally high, mainly due to the influence of the  $q$  exponent. In theory, one could artificially inflate the FoM of a material by making it exceedingly thin.

The ongoing investigation into (LSVO) and (LSCO) presents a potential for furthering our comprehension of their complex characteristics, customizing them to suit particular uses, and progressing the development of optoelectronic devices. This work also addresses obstacles to the integration of those materials, sustainability, and manufacturing methods, thereby positioning these materials to adequately meet technological demands.

The use of (LSVO) as an n-type transparent conducting oxide (TCO) and (LSCO) as a p-type counterpart can open prospects in advanced materials science. LSVO, with its exceptional electron mobility and transparency, holds promise as a high-performance TCO. The remarkable work function of LSCO is especially intriguing, offering an interesting resource for developing efficient photovoltaic systems and enhancing the energy conversion efficiency of solar cells. Furthermore, the exploration of these materials on other substrates, such as glass, extends the horizons of their application. Glass substrates is dominant in various industries, and understanding how LSVO and LSCO behave and grow on this substrate is important. Scaling up to large-area PLD can make the growth of films on sizes relevant to the industry, allowing for a more comprehensive investigation of their properties. Expanding on this research, the development of similar materials using similar methodologies could

be a very promising perspective. Moreover, creating P-N junctions by combining LSCO and LSCO opens up an exciting path in the study of transparent junctions. Investigating the properties and performance of these transparent junctions could be valuable in the innovations in the field of transparent electronics and energy conversion.



---

## List of publications and conferences

---

### 1. Publication

Vincent Polewczyk, Moussa Mezhoud, Martando Rath, Oualyd El-Khaloufi, Ferdinando Bassato, Arnaud Fouchet, Wilfrid Prellier, Mathieu Frégnaux, Damien Aureau, Luca Braglia, Giovanni Vinai, Piero Torelli, and Ulrike Lüders  
Formation and Etching of the Insulating Sr-Rich  $V^{5+}$  Phase at the Metallic  $SrVO_3$  Surface Revealed by Operando XAS Spectroscopy Characterizations  
Advanced Functional Materials 2301056, 2023

### 2. Publication

M. Rath, M. Mezhoud, O. El Khaloufi, O. Lebedev, J. Cardin, Ch. Labbé, F. Gourbilleau, V. Polewczyk, G. Vinai, P. Torelli, A. Fouchet, A. David, W. Prellier, and U. Lüders  
Artificial ageing of thin films of the indium-free transparent conducting oxide  $SrVO_3$   
ACS Appl. Mater. Interfaces 15 (16), 20240–20251, 2023

### 3. Publication

O. El Khaloufi, A. Cheikh, M. Mezhoud, M. Rath, Y. Abishek, D. Aureau, M. Frégnaux, C. Labbé, J. Cardin, S. Duprey, V. Polewczyk, A. David, W. Prellier, and U. Lüders  
Exploration of the  $(La,Sr)VO_3$  thin film solid solution on low strain  $SrTiO_3$  (001) substrates

Advanced Functional Materials, under review.

4. Publication

Y. Abhishek, S. Pradhan, M. Khokhlova, O. El Khaloufi, Nicole Zi Jia Khong, SoakKuan Lai, A. Fouchet, A. David, U. Lüders, Hoi-Yeung Li, M.S. Ramachandra Rao and W. Prellier  
under publication.

5. Oral presentation

E-MRS 2023 SPRING MEETING, May 29 to June 2, 2023 at the Convention & Exhibition Centre in Strasbourg (France).

6. Oral presentation

Journées du GDR OXYFUN 2020, GDR CNRS 3660 : 30 mars - 3 avril 2020, Guéthary

7. Conference

The 8th Quantum Oxide Research Online Meeting (QUOROM-8), Thursday, 16th February

8. Oral presentation

JMC17 : 17ème Journées de la Matière Condensée, 23-27 août 2021 Rennes (France)

---

## Bibliography

---

- [1] L. Zhang, Y. Zhou, L. Guo, W. Zhao, A. Barnes, H.-T. Zhang, C. Eaton, Y. Zheng, M. Brahlek, H. F. Haneef, N. J. Podraza, M. W. Chan, V. Gopalan, K. M. Rabe, R. Engel-Herbert, Correlated metals as transparent conductors, *Nature Materials* 15 (2) (2016) 204–210.
- [2] I. Shein, V. Kozhevnikov, A. Ivanovskii, First-principles calculations of the elastic and electronic properties of the cubic perovskites  $\text{SrMO}_3$  (M= Ti, V, Zr and Nb) in comparison with  $\text{SrSnO}_3$ , *Solid State Sciences* 10 (2) (2008) 217–225.
- [3] U. Lüders, Q.-R. Li, R. Feyerherm, E. Dudzik, The evolution of octahedral rotations of orthorhombic  $\text{LaVO}_3$  in superlattices with cubic  $\text{SrVO}_3$ , *Journal of Physics and Chemistry of Solids* 75 (12) (2014) 1354–1360.
- [4] A. Biswas, Y. Jeong, *Epitaxy*, Intech Open, 2017.
- [5] D. G. Schlom, L.-Q. Chen, C. J. Fennie, V. Gopalan, D. A. Muller, X. Pan, R. Ramesh, R. Uecker, Elastic strain engineering of ferroic oxides, *Mrs Bulletin* 39 (2) (2014) 118–130.

- [6] M. Brahlek, L. Zhang, J. Lapano, H.-T. Zhang, R. Engel-Herbert, N. Shukla, S. Datta, H. Paik, D. G. Schlom, Opportunities in vanadium-based strongly correlated electron systems, *MRS Communications* 7 (2017) 27.
- [7] M. Mirjolet, F. Sánchez, J. Fontcuberta, High carrier mobility, electrical conductivity, and optical transmittance in epitaxial SrVO<sub>3</sub> thin films, *Advanced Functional Materials* 29 (14) (2019) 1808432.
- [8] T.-h. Arima, Y. Tokura, Optical study of electronic structure in perovskite-type RMO<sub>3</sub> (R= La, Y; M= Sc, Ti, V, Cr, Mn, Fe, Co, Ni, Cu), *Journal of the Physical Society of Japan* 64 (7) (1995) 2488–2501.
- [9] L. F. Kourkoutis, Y. Hotta, T. Susaki, H. Hwang, D. Muller, Nanometer scale electronic reconstruction at the interface between LaVO<sub>3</sub> and LaVO<sub>4</sub>, *Physical review letters* 97 (25) (2006) 256803.
- [10] H.-T. Zhang, M. Brahlek, X. Ji, S. Lei, J. Lapano, J. W. Freeland, V. Gopalan, R. Engel-Herbert, High-quality LaVO<sub>3</sub> films as solar energy conversion material, *ACS applied materials & interfaces* 9 (14) (2017) 12556–12562.
- [11] S. Miyasaka, T. Okuda, Y. Tokura, Critical behavior of metal-insulator transition in La<sub>1-x</sub>Sr<sub>x</sub>VO<sub>3</sub>, *Physical Review Letters* 85 (25) (2000) 5388.
- [12] L. Hu, R. Wei, J. Yan, D. Wang, X. Tang, X. Luo, W. Song, J. Dai, X. Zhu, C. Zhang, et al., La<sub>2/3</sub>Sr<sub>1/3</sub>VO<sub>3</sub> thin films: a new p-type transparent conducting oxide with very high figure of merit, *Advanced Electronic Materials* 4 (3) (2018) 1700476.
- [13] A. Boileau, A. Cheikh, A. Fouchet, A. David, C. Labbé, P. Marie, F. Gourbilleau, U. Lüders, Tuning of the optical properties of the transparent conducting oxide SrVO<sub>3</sub> by electronic correlations, *Advanced Optical Materials* 7 (7) (2019) 1801516.
- [14] A. Boileau, A. Cheikh, A. Fouchet, A. David, R. Escobar-Galindo, C. Labbé, P. Marie, F. Gourbilleau, U. Lüders, Optical and electrical properties of the

- transparent conductor SrVO<sub>3</sub> without long-range crystalline order, *Applied Physics Letters* 112 (2) (2018).
- [15] K. H. Zhang, Y. Du, A. Papadogianni, O. Bierwagen, S. Sallis, L. F. Piper, M. E. Bowden, V. Shutthanandan, P. V. Sushko, S. A. Chambers, Perovskite Sr-doped LaCrO<sub>3</sub> as a new p-type transparent conducting oxide, *Advanced Materials* 27 (35) (2015) 5191–5195.
- [16] G. Brunin, Perovskite Sr-doped LaCrO<sub>3</sub>: An ab-initio study, Ph.D. thesis, Université catholique de Louvain (2016).
- [17] D. Han, R. Moalla, I. Fina, V. M. Giordano, M. d’Esperonnat, C. Botella, G. Grenet, R. Debord, S. Pailhès, G. Saint-Girons, et al., Giant tuning of electronic and thermoelectric properties by epitaxial strain in p-type sr-doped LaCrO<sub>3</sub> transparent thin films, *ACS Applied Electronic Materials* 3 (8) (2021) 3461–3471.
- [18] K. H. Zhang, Y. Du, P. Sushko, M. E. Bowden, V. Shutthanandan, S. Sallis, L. F. Piper, S. A. Chambers, Hole-induced insulator-to-metal transition in La<sub>1-x</sub>Sr<sub>x</sub>CrO<sub>3</sub> epitaxial films, *Physical Review B* 91 (15) (2015) 155129.
- [19] V. Polewczyk, M. Mezhoud, M. Rath, O. El-Khaloufi, F. Bassato, A. Fouchet, W. Prellier, M. Frégnaux, D. Aureau, L. Braglia, et al., Formation and etching of the insulating Sr-rich V<sup>5+</sup> phase at the metallic SrVO<sub>3</sub> surface revealed by operando xas spectroscopy characterizations, *Advanced Functional Materials* (2023) 2301056.
- [20] Hydrargyrum, [Bragg diffraction](#), image from Wikimedia Commons (Accessed: September 4, 2023).  
URL [https://commons.wikimedia.org/wiki/File:Bragg\\_diffraction\\_2.svg](https://commons.wikimedia.org/wiki/File:Bragg_diffraction_2.svg)
- [21] C. D. N. Chan, [Diffractométrie X : montage deux cercles  \$\theta - \theta\$](#) , image from Wikimedia Commons (Accessed: September 4, 2023).  
URL [https://commons.wikimedia.org/wiki/File:Drx\\_theta\\_theta.png](https://commons.wikimedia.org/wiki/File:Drx_theta_theta.png)

- [22] S.-Y. Lin, M.-J. Li, W.-T. Cheng, FT-IR and Raman vibrational microspectroscopies used for spectral biodiagnosis of human tissues, *Spectroscopy* 21 (1) (2007) 1–30.
- [23] [Charging in X-ray Photoelectron Spectroscopy](#), XPS Library (Accessed: September 4, 2023).  
URL <https://xpslibrary.com/charging/>
- [24] R. Zimmermann, R. Claessen, F. Reinert, P. Steiner, S. Hüfner, Strong hybridization in vanadium oxides: evidence from photoemission and absorption spectroscopy, *Journal of Physics: Condensed Matter* 10 (25) (1998) 5697.
- [25] H. Tan, J. Verbeeck, A. Abakumov, G. Van Tendeloo, Oxidation state and chemical shift investigation in transition metal oxides by eels, *Ultramicroscopy* 116 (2012) 24–33.
- [26] A. Cheikh, [Etudes des hétérostructures à bases d'oxydes complexes pour de potentielles utilisations en cellules solaires](#), Ph.D. thesis, Normandie Université (Sep. 2020).  
URL <https://theses.hal.science/tel-03018736>
- [27] J. Webb, M. Sayer, High-temperature transport in lanthanum strontium vanadate, *Journal of Physics C: Solid State Physics* 9 (22) (1976) 4151.
- [28] R. G. Egdell, M. R. Harrison, M. D. Hill, L. Porte, G. Wall, A study of the metal-nonmetal transition in lanthanum strontium vanadate by high-resolution electron spectroscopy, *Journal of Physics C: Solid State Physics* 17 (16) (1984) 2889–2900.
- [29] M. Mirjolet, H. B. Vasili, L. López-Conesa, S. Estradé, F. Peiró, J. Santiso, F. Sánchez, P. Machado, P. Gargiani, M. Valvidares, et al., Independent tuning of optical transparency window and electrical properties of epitaxial SrVO<sub>3</sub> thin films by substrate mismatch, *Advanced Functional Materials* 29 (37) (2019) 1904238.

- 
- [30] E. Fortunato, D. Ginley, H. Hosono, D. C. Paine, Transparent Conducting Oxides for Photovoltaics, *MRS Bulletin* 32 (3) (2007) 242–247.
- [31] U. Betz, M. Kharrazi Olsson, J. Marthy, M. Escolá, F. Atamny, Thin films engineering of indium tin oxide: Large area flat panel displays application, *Surface and Coatings Technology* 200 (20) (2006) 5751–5759.
- [32] H. Hosono, Recent progress in transparent oxide semiconductors: Materials and device application, *Thin Solid Films* 515 (15) (2007) 6000–6014.
- [33] C. G. Granqvist, Transparent conductors as solar energy materials: A panoramic review, *Solar Energy Materials and Solar Cells* 91 (17) (2007) 1529–1598.
- [34] Z. Wang, C. Chen, K. Wu, H. Chong, H. Ye, Transparent conductive oxides and their applications in near infrared plasmonics, *physica status solidi (a)* 216 (5) (2019) 1700794.
- [35] K. Bädeker, Über die elektrische Leitfähigkeit und die thermoelektrische Kraft einiger Schwermetallverbindungen, *Annalen der Physik* 327 (4) (1907) 749–766.
- [36] T. M. Carter, H. S. Koontz, Electrical lead arrangement for a heatable transparency, US patent US4918288A (1988).
- [37] T. Minami, Transparent conducting oxide semiconductors for transparent electrodes, *Semiconductor science and technology* 20 (4) (2005) S35.
- [38] J. K. Borchardt, Developments in organic displays, *Materials Today* 7 (9) (2004) 42–46.
- [39] H. Kawazoe, M. Yasukawa, H. Hyodo, M. Kurita, H. Yanagi, H. Hosono, Preparation of  $\text{CuYO}_2$  thin films by sol-gel method using copper acetate and yttrium acetate as metal sources, *Nature* 389 (1997) 939–942.

- [40] H. Yanagi, T. Hase, S. Ibuki, K. Ueda, H. Hosono, Bipolarity in electrical conduction of transparent oxide semiconductor  $\text{CuInO}_2$  with delafossite structure, *Applied Physics Letters* 78 (11) (2001) 1583–1585.
- [41] R. Nagarajan, A. Draeseke, A. Sleight, J. Tate, p-type conductivity in  $\text{CuCr}_{1-x}\text{Mg}_x\text{O}_2$  films and powders, *Journal of Applied Physics* 89 (12) (2001) 8022–8025.
- [42] M. Feng, H. Zhou, W. Guo, D. Zhang, L. Ye, W. Li, J. Ma, G. Wang, S. Chen, Fabrication of p-type transparent conducting  $\text{Cu}_x\text{Zn}_{1-x}\text{S}$  films on glass substrates with high conductivity and optical transparency, *Journal of Alloys and Compounds* 750 (2018) 750–756.
- [43] T. F. Wu, H. Li, P.-C. Huang, A. Rahimi, G. Hills, B. Hodson, W. Hwang, J. M. Rabaey, H.-S. P. Wong, M. M. Shulaker, et al., Hyperdimensional computing exploiting carbon nanotube fets, resistive ram, and their monolithic 3d integration, *IEEE Journal of Solid-State Circuits* 53 (11) (2018) 3183–3196.
- [44] L. Shoham, M. Baskin, M.-G. Han, Y. Zhu, L. Kornblum, Scalable synthesis of the transparent conductive oxide  $\text{SrVO}_3$ , *Advanced Electronic Materials* 6 (1) (2020) 1900584.
- [45] R. Xu, L. Min, Z. Qi, X. Zhang, J. Jian, Y. Ji, F. Qian, J. Fan, C. Kan, H. Wang, et al., Perovskite transparent conducting oxide for the design of a transparent, flexible, and self-powered perovskite photodetector, *ACS applied materials & interfaces* 12 (14) (2020) 16462–16468.
- [46] Z. Liu, N. Podraza, S. Khare, P. Sarin, Transparency enhancement for  $\text{SrVO}_3$  by  $\text{SrTiO}_3$  mixing: A first-principles study, *Computational Materials Science* 144 (2018) 139–146.
- [47] D. H. Jung, H. S. So, H. Lee, Structural and electrical properties of transparent conductor  $\text{SrVO}_3$  thin films grown using radio frequency sputtering deposition, *Journal of Vacuum Science & Technology A* 37 (2) (2019).

- [48] S. D. Marks, L. Lin, P. Zuo, P. J. Strohbeen, R. Jacobs, D. Du, J. R. Waldvogel, R. Liu, D. E. Savage, J. H. Booske, et al., Solid-phase epitaxial growth of the correlated-electron transparent conducting oxide SrVO<sub>3</sub>, *Physical Review Materials* 5 (8) (2021) 083402.
- [49] M. Mirjolet, M. Kataja, T. K. Hakala, P. Komissinskiy, L. Alff, G. Herranz, J. Fontcuberta, Optical plasmon excitation in transparent conducting SrNbO<sub>3</sub> and SrVO<sub>3</sub> thin films, *Advanced Optical Materials* 9 (17) (2021) 2100520.
- [50] R. Xu, X. Zhang, D. Zhang, J. Liu, J. Lu, R. Zhao, Y. Ji, F. Qian, H. Wang, J. Fan, et al., High stability of flexible perovskite transparent conductive oxide film via van der Waals heteroepitaxy, *Journal of Alloys and Compounds* 890 (2022) 161897.
- [51] A. Boileau, S. Hurand, F. Baudouin, U. Lüders, M. Dallochio, B. Bérimi, A. Cheikh, A. David, F. Paumier, T. Girardeau, P. Marie, C. Labbé, J. Cardin, D. Aureau, M. Frégnaux, M. Guilloux-Viry, W. Prellier, Y. Dumont, V. Demange, A. Fouchet, Highly transparent and conductive indium-free vanadates crystallized at reduced temperature on glass using a 2d transparent nanosheet seed layer, *Advanced Functional Materials* 32 (5) (2022) 2108047.
- [52] P. Anagha, M. Kinha, A. Khare, D. Rana, Precise measurement of correlation parameters driving optical transparency in CaVO<sub>3</sub> thin film by steady state and time resolved terahertz spectroscopy, *Journal of Applied Physics* 132 (3) (2022).
- [53] Y. Park, J. Roth, D. Oka, Y. Hirose, T. Hasegawa, A. Paul, A. Pogrebnyakov, V. Gopalan, T. Birol, R. Engel-Herbert, SrNbO<sub>3</sub> as a transparent conductor in the visible and ultraviolet spectra, *Communications Physics* 3 (1) (2020) 102.
- [54] J. Roth, A. Paul, N. Goldner, A. Pogrebnyakov, K. Agueda, T. Birol, N. Alem, R. Engel-Herbert, Sputtered Sr<sub>x</sub>NbO<sub>3</sub> as a UV-transparent conducting film, *ACS applied materials & interfaces* 12 (27) (2020) 30520–30529.

- [55] J. Kim, H. Yun, J. Seo, J. H. Kim, J. H. Kim, K. A. Mkhoyan, B. Kim, K. Char, Deep-UV transparent conducting oxide La-doped SrSnO<sub>3</sub> with a high figure of merit, *ACS Applied Electronic Materials* 4 (7) (2022) 3623–3631.
- [56] E. A. Katz, Perovskite: Name puzzle and german-russian odyssey of discovery, *Helvetica Chimica Acta* 103 (6) (2020) e2000061.
- [57] J. B. Goodenough, Electronic and ionic transport properties and other physical aspects of perovskites, *Reports on Progress in Physics* 67 (11) (2004) 1915–1993.
- [58] R. H. Mitchell, *Perovskites: modern and ancient*, Almaz Press, 2002.
- [59] V. M. Goldschmidt, Die Gesetze der Krystallochemie, *Naturwissenschaften* 14 (21) (1926) 477–485.
- [60] A. Fujimori, Electronic structure of metallic oxides: Band-gap closure and valence control, *Journal of Physics and Chemistry of Solids* 53 (12) (1992) 1595–1602.
- [61] M. Kinyanjui, Y. Lu, N. Gauquelin, M. Wu, A. Frano, P. Wochner, M. Reehuis, G. Christiani, G. Logvenov, H.-U. Habermeier, et al., Lattice distortions and octahedral rotations in epitaxially strained LaNiO<sub>3</sub>/LaAlO<sub>3</sub> superlattices, *Applied Physics Letters* 104 (22) (2014).
- [62] J. Hwang, Z. Feng, N. Charles, X. R. Wang, D. Lee, K. A. Stoerzinger, S. Muy, R. R. Rao, D. Lee, R. Jacobs, et al., Tuning perovskite oxides by strain: Electronic structure, properties, and functions in (electro) catalysis and ferroelectricity, *Materials Today* 31 (2019) 100–118.
- [63] J. Ngai, F. Walker, C. Ahn, Correlated oxide physics and electronics, *Annual Review of Materials Research* 44 (2014) 1–17.
- [64] J. M. Rondinelli, N. A. Spaldin, Structure and properties of functional oxide thin films: insights from electronic-structure calculations, *Advanced materials* 23 (30) (2011) 3363–3381.

- [65] D. Pesquera, G. Herranz, A. Barla, E. Pellegrin, F. Bondino, E. Magnano, F. Sánchez, J. Fontcuberta, Surface symmetry-breaking and strain effects on orbital occupancy in transition metal perovskite epitaxial films, *Nature communications* 3 (1) (2012) 1189.
- [66] S. Catalano, M. Gibert, J. Fowlie, J. Íñiguez, J. Triscone, J. Kreisel, Rare-earth nickelates  $\text{RNiO}_3$ : thin films and heterostructures, *Reports on Progress in Physics* 81 (4) (2018) 046501.
- [67] E.-J. Guo, R. D. Desautels, D. Keavney, A. Herklotz, T. Z. Ward, M. R. Fitzsimmons, H. N. Lee, Switchable orbital polarization and magnetization in strained  $\text{LaCoO}_3$  films, *Physical Review Materials* 3 (1) (2019) 014407.
- [68] F. S. Razavi, G. Gross, H.-U. Habermeier, O. Lebedev, S. Amelinckx, G. Van Tendeloo, A. Vigliante, Epitaxial strain induced metal insulator transition in  $\text{La}_{0.9}\text{Sr}_{0.1}\text{MnO}_3$  and  $\text{La}_{0.88}\text{Sr}_{0.1}\text{MnO}_3$  thin films, *Applied Physics Letters* 76 (2) (2000) 155–157.
- [69] C. Adamo, X. Ke, H. Wang, H. Xin, T. Heeg, M. Hawley, W. Zander, J. Schubert, P. Schiffer, D. Muller, et al., Effect of biaxial strain on the electrical and magnetic properties of (001)  $\text{La}_{0.7}\text{Sr}_{0.3}\text{MnO}_3$  thin films, *Applied Physics Letters* 95 (11) (2009).
- [70] B. Lee, O.-U. Kwon, R. H. Shin, W. Jo, C. U. Jung, Ferromagnetism and Ru-Ru distance in  $\text{SrRuO}_3$  thin film grown on  $\text{SrTiO}_3$  (111) substrate, *Nanoscale Research Letters* 9 (2014) 1–9.
- [71] A. Vailionis, W. Siemons, G. Koster, Room temperature epitaxial stabilization of a tetragonal phase in  $\text{ARuO}_3$  ( $A = \text{Ca}$  and  $\text{Sr}$ ) thin films, *Applied Physics Letters* 93 (5) (2008).
- [72] D. Kan, Y. Shimakawa, Strain effect on thermoelectric properties of  $\text{SrRuO}_3$  epitaxial thin films, *Applied Physics Letters* 115 (2) (2019).

- [73] Y. Shuyao, X. Ying, Y. Haitao, L. Tao, et al., Electronic structures and ferroelectric instabilities of cubic  $AVO_3$  (A= Sr, Ba, and Pb) perovskites by first-principles calculations, *Journal of Physics. Condensed Matter* 22 (2010).
- [74] M. Imada, A. Fujimori, Y. Tokura, Metal-insulator transitions, *Rev. Mod. Phys.* 70 (1998) 1039–1263.
- [75] B. Chamberland, P. Danielson, Alkaline-earth vanadium (IV) oxides having the  $AVO_3$  composition, *Journal of Solid State Chemistry* 3 (2) (1971) 243–247.
- [76] P. Dougier, J. C. Fan, J. B. Goodenough, Etude des proprietes magnetiques, electriques et optiques des phases de structure perovskite  $SrVO_{2.90}$  et  $SrVO_3$ , *Journal of Solid State Chemistry* 14 (3) (1975) 247–259.
- [77] H. He, Z. Yang, Y. Xu, A. T. Smith, G. Yang, L. Sun, Perovskite oxides as transparent semiconductors: a review, *Nano Convergence* 7 (1) (2020) 32.
- [78] G. Sclauzero, K. Dymkowski, C. Ederer, Tuning the metal-insulator transition in  $d^1$  and  $d^2$  perovskites by epitaxial strain: A first-principles-based study, *Physical Review B* 94 (24) (2016) 245109.
- [79] A. Paul, T. Birol, Strain tuning of plasma frequency in vanadate, niobate, and molybdate perovskite oxides, *Physical Review Materials* 3 (8) (2019).
- [80] T. Maekawa, K. Kurosaki, S. Yamanaka, Physical properties of polycrystalline  $SrVO_{3-\delta}$ , *Journal of alloys and compounds* 426 (1-2) (2006) 46–50.
- [81] S. Geller, M. Gilleo, Crystallographic studies of perovskite-like compounds. IV. rare earth scandates, vanadites, galliates, orthochromites, *Acta Cryst* 10 (1957) 239.
- [82] H. Sawada, N. Hamada, K. Terakura, T. Asada, Orbital and spin orderings in  $YVO_3$  and  $LaVO_3$  in the generalized gradient approximation, *Physical Review B* 53 (19) (1996) 12742.

- [83] A. Ferretti, D. Ridgley, R. Arnott, J. Goodenough, et al., Single-crystal growth and properties of the perovskites  $\text{LaVO}_3$  and  $\text{YVO}_3$ , *Journal of Applied Physics (US)* 37 (1966).
- [84] N. Hur, S. Kim, K. Yu, Y. Park, J. Park, S. Kim, Structural and magnetic properties of the anion-deficient  $\text{LaVO}_{3-\delta}$ , *Solid state communications* 92 (6) (1994) 541–546.
- [85] W. Choi, T. Sands, K.-Y. Kim, Epitaxial growth of semiconducting  $\text{LaVO}_3$  thin films, *Journal of Materials Research* 15 (2000) 1–3.
- [86] Y. Hotta, Y. Mukunoki, T. Susaki, H. Hwang, L. Fitting, D. Muller, Growth and epitaxial structure of  $\text{LaVO}_x$  films, *Applied physics letters* 89 (3) (2006).
- [87] H. Rotella, O. Copie, A. Pautrat, P. Boullay, A. David, D. Pelloquin, C. Labbé, C. Frilay, W. Prellier, Two components for one resistivity in  $\text{LaVO}_3/\text{SrTiO}_3$  heterostructure, *Journal of Physics: Condensed Matter* 27 (9) (2015) 095603.
- [88] P. Dougier, A. Casalot, Sur quelques nouvelles séries de composés oxygénés du vanadium et des lanthanides de structure perovskite, *Journal of Solid State Chemistry* 2 (3) (1970) 396–403.
- [89] H. Rotella, O. Copie, G. Steciuk, H. Ouerdane, P. Boullay, P. Roussel, M. Morales, A. David, A. Pautrat, B. Mercey, et al., Structural analysis of strained  $\text{LaVO}_3$  thin films, *Journal of Physics: Condensed Matter* 27 (17) (2015) 175001.
- [90] J. Yang, Structural analysis of perovskite  $\text{LaCr}_{1-x}\text{Ni}_x\text{O}_3$  by Rietveld refinement of X-ray powder diffraction data, *Acta Crystallographica Section B: Structural Science* 64 (3) (2008) 281–286.
- [91] T. Arima, Y. Tokura, J. Torrance, Variation of optical gaps in perovskite-type 3d transition-metal oxides, *Physical Review B* 48 (23) (1993) 17006.
- [92] B. Chamberland, Preparation and properties of  $\text{SrCrO}_3$ , *Solid State Communications* 5 (8) (1967) 663–666.

- [93] L. Ortega-San-Martin, A. J. Williams, J. Rodgers, J. P. Attfield, G. Heymann, H. Huppertz, Microstrain sensitivity of orbital and electronic phase separation in  $\text{SrCrO}_3$ , *Phys. Rev. Lett.* 99 (2007) 255701.
- [94] J.-S. Zhou, C.-Q. Jin, Y.-W. Long, L.-X. Yang, J. B. Goodenough, Anomalous electronic state in  $\text{CaCrO}_3$  and  $\text{SrCrO}_3$ , *Phys. Rev. Lett.* 96 (2006) 046408.
- [95] K. H. L. Zhang, P. V. Sushko, R. Colby, Y. Du, M. E. Bowden, S. A. Chambers, Reversible nano-structuring of  $\text{SrCrO}_{3-\delta}$  through oxidation and reduction at low temperature, *Nature Communications* 5 (1) (2014) 4669.
- [96] Y.-T. Huang, S. R. Kavanagh, D. O. Scanlon, A. Walsh, R. L. Hoyer, Perovskite-inspired materials for photovoltaics and beyond—from design to devices, *Nanotechnology* 32 (13) (2021) 132004.
- [97] Y. Du, C. Li, K. H. Zhang, M. E. McBriarty, S. R. Spurgeon, H. S. Mehta, D. Wu, S. A. Chambers, An all-perovskite p-n junction based on transparent conducting  $\text{p-La}_{1-x}\text{Sr}_x\text{CrO}_3$  epitaxial layers, *Applied Physics Letters* 111 (6) (2017).
- [98] X. Marti, I. Fina, C. Frontera, J. Liu, P. Wadley, Q. He, R. J. Paull, J. D. Clarkson, J. Kudrnovský, I. Turek, J. Kuneš, D. Yi, J.-H. Chu, C. T. Nelson, L. You, E. Arenholz, S. Salahuddin, J. Fontcuberta, T. Jungwirth, R. Ramesh, Room-temperature antiferromagnetic memory resistor, *Nat. Mater* 13 (2014) 367.
- [99] D. Karim, A. Aldred, Localized level hopping transport in  $(\text{La,Sr})\text{CrO}_3$ , *Physical Review B* 20 (6) (1979) 2255.
- [100] L. Farrell, K. Fleischer, D. Caffrey, D. Mullarkey, E. Norton, I. Shvets, Conducting mechanism in the epitaxial p-type transparent conducting oxide  $\text{Cr}_2\text{O}_3$ : Mg, *Physical Review B* 91 (12) (2015) 125202.
- [101] D. Han, R. Moalla, I. Fina, V. M. Giordano, M. d'Esperonnat, C. Botella, G. Grenet, R. Debord, S. Pailhès, G. Saint-Girons, R. Bachelet, Giant Tuning

- of Electronic and Thermoelectric Properties by Epitaxial Strain in p-Type Sr-Doped  $\text{LaCrO}_3$  Transparent Thin Films, *ACS Applied Electronic Materials* 3 (8) (2021) 3461–3471.
- [102] F. Lo Presti, A. L. Pellegrino, G. Malandrino, Metal-organic chemical vapor deposition of oxide perovskite films: A facile route to complex functional systems, *Advanced Materials Interfaces* 9 (14) (2022) 2102501.
- [103] D. Pla, C. Jimenez, M. Burriel, Engineering of functional manganites grown by MOCVD for miniaturized devices, *Advanced Materials Interfaces* 4 (8) (2017) 1600974.
- [104] P. H. T. Ngamou, N. Bahlawane, Chemical vapor deposition and electric characterization of perovskite oxides  $\text{LaMO}_3$  ( $M = \text{Co}, \text{Fe}, \text{Cr}$  and  $\text{Mn}$ ) thin films, *Journal of Solid State Chemistry* 182 (4) (2009) 849–854.
- [105] M. D. McDaniel, T. Q. Ngo, S. Hu, A. Posadas, A. A. Demkov, J. G. Ekerdt, Atomic layer deposition of perovskite oxides and their epitaxial integration with Si, Ge, and other semiconductors, *Applied Physics Reviews* 2 (4) (2015) 041301.
- [106] A. Jolivet, Développement d'oxydes transparents conducteurs de nouvelle génération par ALD, Ph.D. thesis, Université de Caen Normandie (2023).
- [107] K. H. L. Zhang, Y. Du, P. V. Sushko, M. E. Bowden, V. Shutthanandan, L. Qiao, G. X. Cao, Z. Gai, S. Sallis, L. F. J. Piper, S. A. Chambers, Electronic and magnetic properties of epitaxial perovskite  $\text{SrCrO}_3(001)$ , *Journal of Physics: Condensed Matter* 27 (24) (2015) 245605.
- [108] Y. Bourlier, M. Frégnaux, B. Bérini, A. Fouchet, Y. Dumont, D. Aureau, XPS monitoring of  $\text{SrVO}_3$  thin films from demixing to air ageing: The asset of treatment in water, *Applied Surface Science* 553 (2021) 149536.
- [109] B. Bérini, V. Demange, M. Bouttemy, E. Popova, N. Keller, Y. Dumont, A. Fouchet, Control of High Quality  $\text{SrVO}_3$  Electrode in Oxidizing Atmosphere, *Advanced Materials Interfaces* 3 (18) (2016) 1600274.

- [110] R. C. Germanicus, Y. Bourlier, V. Notot, B. Bérini, V. Demange, M. Berthe, A. Boileau, M. Euchin, Y. Dumont, D. Aureau, M. Fregnaux, B. Grandidier, U. Lüders, A. David, W. Prellier, L. Biadala, A. Fouchet, Three dimensional resistance mapping of self-organized  $\text{Sr}_3\text{V}_2\text{O}_8$  nanorods on metallic perovskite  $\text{SrVO}_3$  matrix, *Applied Surface Science* 510 (2020) 145522.
- [111] M. Rath, M. Mezhoud, O. El Khaloufi, O. Lebedev, J. Cardin, C. Labbé, F. Gourbilleau, V. Polewczyk, G. Vinai, P. Torelli, A. Fouchet, A. David, W. Prellier, U. Lüders, Artificial Aging of Thin Films of the Indium-Free Transparent Conducting Oxide  $\text{SrVO}_3$ , *ACS Applied Materials & Interfaces* 15 (16) (2023) 20240–20251.
- [112] A. Glavic, M. Björck, *GenX 3*: the latest generation of an established tool, *Journal of Applied Crystallography* 55 (4) (2022) 1063–1071.
- [113] H. Rotella, Etude de films minces de vanadates : contribution à la résolution de la structure et aux propriétés de transport, Ph.D. thesis, Université de Caen Normandie (2013).
- [114] H. Rotella, U. Lüders, P.-E. Janolin, V. H. Dao, D. Chateigner, R. Feyerherm, E. Dudzik, W. Prellier, Octahedral tilting in strained  $\text{LaVO}_3$  thin films, *Physical Review B* 85 (18) (2012) 184101.
- [115] D. C. Vaz, E. Lesne, A. Sander, H. Naganuma, E. Jacquet, J. Santamaria, A. Barthélémy, M. Bibes, Tuning Up or Down the Critical Thickness in  $\text{LaAlO}_3/\text{SrTiO}_3$  through In Situ Deposition of Metal Overlayers, *Advanced Materials* 29 (28) (2017) 1700486.
- [116] X.-J. Gu, Z.-L. Luo, Y.-Q. Dong, J.-T. Zhou, H. Xu, B. Hong, C. Gao, Redox controllable switch of crystalline phase and physical property in  $\text{SrVO}_x$  epitaxial films, *Chinese Journal of Chemical Physics* 32 (6) (2019) 727–730.
- [117] Y. Bourlier, M. Frégnaux, B. Bérini, A. Fouchet, Y. Dumont, D. Aureau, Surface Characterizations and Selective Etching of Sr-Rich Segregation on

- Top of SrVO<sub>3</sub> Thin-Films Grown by Pulsed Laser Deposition, *ChemNanoMat* 5 (5) (2019) 674–681.
- [118] K. Ellmer, Past achievements and future challenges in the development of optically transparent electrodes, *Nature Photonics* 6 (12) (2012) 809–817.
- [119] M. Onoda, H. Ohta, H. Nagasawa, Metallic properties of perovskite oxide SrVO<sub>3</sub>, *Solid State Communications* 79 (4) (1991) 5.
- [120] M. Nasir, I. Kim, K. Lee, S.-i. Kim, K. H. Lee, H. J. Park, Study on the decisive factor for metal–insulator transitions in a LaVO<sub>3</sub> Mott–Hubbard insulator, *Physical Chemistry Chemical Physics* 25 (2023) 3942–3949.
- [121] M. Uchida, K. Oishi, M. Matsuo, W. Koshibae, Y. Onose, M. Mori, J. Fujioka, S. Miyasaka, S. Maekawa, Y. Tokura, Thermoelectric response in the incoherent transport region near Mott transition: The case study of La<sub>1-x</sub>Sr<sub>x</sub>VO<sub>3</sub>, *Physical Review B* 83 (2011) 165127.
- [122] H. Makino, I. H. Inoue, M. J. Rozenberg, I. Hase, Y. Aiura, S. Onari, Bandwidth control in a perovskite-type 3d<sup>1</sup>-correlated metal Ca<sub>1-x</sub>Sr<sub>x</sub>VO<sub>3</sub> II. Optical spectroscopy, *Physical Review B* 58 (8) (1998) 4384–4393.
- [123] E. N. Yitamben, T. C. Lovejoy, A. B. Pakhomov, S. M. Heald, E. Negusse, D. Arena, F. S. Ohuchi, M. A. Olmstead, Correlation between morphology, chemical environment, and ferromagnetism in the intrinsic-vacancy dilute magnetic semiconductor Cr-doped Ga<sub>2</sub>Se<sub>3</sub>/Si(001), *Phys. Rev. B* 83 (2011) 045203.
- [124] P. Machado, R. Guzmán, R. J. Morera, J. Alcalà, A. Palau, W. Zhou, M. Coll, Chemical synthesis of La<sub>0.75</sub>Sr<sub>0.25</sub>CrO<sub>3</sub> thin films for p-type transparent conducting electrodes, *Chemistry of Materials* 35 (9) (2023) 3513–3521.
- [125] A. Kojima, K. Teshima, Y. Shirai, T. Miyasaka, Organometal halide perovskites as visible-light sensitizers for photovoltaic cells, *Journal of the American Chemical Society* 131 (17) (2009) 6050–6051.

- [126] G. Haacke, New figure of merit for transparent conductors, *Journal of Applied physics* 47 (9) (1976) 4086–4089.